CANADIAN THESES ON MICROFICHE

THÈSES CANADIENNES SUR MICROFICHE

NOTICE

The quality of this microfiche is heavily dependent upon the quality of the original thesis submitted for microfilming. Every effort has been made to ensure the highest quality of reproduction possible.

If pages are missing, contact the university which granted the degree.

Some pages may have indistinct print especially if the original pages were typed with a poor typewriter ribbon or if the university sent us an inferior photocopy.

Previously copyrighted materials (journal articles, published tests, etc.) are not filmed.

Reproduction in full or in part of this film is governed by the Canadian Copyright Act, R.S.C. 1970, c. C-30. Please read the authorization forms which accompany this thesis.

AVIS

La qualité de cette microfiche dépend grandement de la qualité de la thèse soumise au microfilmage. Nous avons tout fait pour assurer une qualité supérieure de reproduction.

S'il manque des pages, veuillez communiquer avec l'université qui a conféré le grade.

La qualité d'impression de certaines pages peut laisser à désirer, surtout si les pages originales ont été dactylographiées à l'aide d'un ruban usé ou si l'université nous a fait parvenir une photocopie de qualité inférieure.

Les documents qui font déjà l'objet d'un droit d'auteur (articles de revue, examens publiés, etc.) ne sont pas microfilmés.

La reproduction, même partielle, de ce microfilm est soumise à la Loi canadienne sur le droit d'auteur, SRC 1970, c. C-30. Veuillez prendre connaissance des formules d'autorisation qui accompagnent cette thèse.

THIS DISSERTATION HAS BEEN MICROFILMED EXACTLY AS RECEIVED

LA THÈSE A ÉTÉ MICROFILMÉE TELLE QUE NOUS L'AVONS REÇUE

Canada

0-315-19489-8

 National Library
of Canada

Bibliothèque nationale
du Canada

Canadian Theses Division   Division des thèses canadiennes

Ottawa, Canada
K1A 0N4

67397

PERMISSION TO MICROFILM — AUTORISATION DE MICROFILMER

• Please print or type — Écrire en lettres moulées ou dactylographier

Full Name of Author — Nom complet de l'auteur

Ellen Elisabeth Grein El-Khatib

Date of Birth — Date de naissance

5 Feb 1950

Country of Birth — Lieu de naissance

West-Germany

Permanent Address — Résidence fixe

1422 Center Rd.
Mascouche-Heights, Quebec
JoN 1T0

Title of Thesis — Titre de la thèse

Detection and Prevention of Lung Damage in Large
Field Irradiation with X-rays

University — Université

University of Alberta

Degree for which thesis was presented — Grade pour lequel cette thèse fut présentée.

Ph.D.

Year this degree conferred — Année d'obtention de ce grade

1984

Name of Supervisor — Nom du directeur de thèse

Dr. J.J. Battista

Permission is hereby granted to the NATIONAL LIBRARY OF CANADA to microfilm this thesis and to lend or sell copies of the film.

The author reserves other publication rights, and neither the thesis nor extensive extracts from it may be printed or otherwise reproduced without the author's written permission.

L'autorisation est, par là présente, accordée à la BIBLIOTHÈQUE NATIONALE DU CANADA de microfilmer cette thèse et de prêter ou de vendre des exemplaires du film.

L'auteur se réserve les autres droits de publication; ni la thèse ni de longs extraits de celle-ci ne doivent être imprimés ou autrement reproduits sans l'autorisation écrite de l'auteur.

Date

July 3, 1984

Signature

Ellen El-Khatib

The University of Alberta

DETECTION AND PREVENTION OF LUNG DAMAGE IN LARGE FIELD
IRRADIATION WITH X-RAYS

by

Ellen Elisabeth Grein El-Khatib

A THESIS

SUBMITTED TO THE FACULTY OF GRADUATE STUDIES AND RESEARCH

IN PARTIAL FULFILLMENT OF THE REQUIREMENTS FOR THE DEGREE

OF DOCTOR OF PHILOSOPHY

DEPARTMENT OF PHYSICS

EDMONTON, ALBERTA

FALL 1984

THE UNIVERSITY OF ALBERTA

RELEASE FORM

NAME OF AUTHOR   ELLEN EL-KHATIB

TITLE OF THESIS   DETECTION AND PREVENTION OF LUNG DAMAGE
                  IN LARGE FIELD IRRADIATION WITH X-RAYS

DEGREE FOR WHICH THESIS WAS PRESENTED DOCTOR OF PHILOSOPHY

YEAR THIS DEGREE GRANTED   1984

    Permission is hereby granted to THE UNIVERSITY OF

ALBERTA LIBRARY to reproduce single copies of this

thesis and to lend or sell such copies for private,

scholarly or scientific research purposes only.

    The author reserves other publication rights, and

neither the thesis nor extensive extracts from it may

be printed or otherwise reproduced without the author's

written permission.

                              (Signed)

                              PERMANENT ADDRESS:

                              151 MICHENER PARK

                              EDMONTON, ALBERTA

                              CANADA

DATED   JUNE 1 1984

THE UNIVERSITY OF ALBERTA

FACULTY OF GRADUATE STUDIES AND RESEARCH

The undersigned certify that they have read, and

recommend to the Faculty of Graduate Studies and Research,

for acceptance, a thesis entitled

DETECTION AND PREVENTION OF LUNG DAMAGE IN

LARGE FIELD X-IRRADIATION

Submitted by Ellen El-Khatib

in partial fulfillment of the requirements for the degree of

Doctor of Philosophy

in Medical Physics

....
Supervisor

....

....

....

....
External Examiner

Date: May 31/84

To my husband Ziad

      -for his help and encouragement

and to my children

ABSTRACT

In radiation therapy there are many instances in which irradiation of the lung is unavoidable. In particular, in large field irradiations with X-rays there is a potential for serious pulmonary complications which may be fatal. The occurrence and severity of lung damage is related to the volume of lung irradiated, the total dose, the dose-rate, the overall duration of radiation therapy, as well as the variable physiological response of individual patients.

The present research deals with radiation-induced pneumonitis in two ways:

(1) A non-invasive diagnostic test based on X-ray computed tomography (CT) for quantifying lung damage early after irradiation, and

(2) Improved accuracy of lung dose calculations for planning radiation therapy.

The reaction of the lung to radiation is monitored in groups of animals which have been irradiated to various single doses to the thorax. This test was able to detect the radiation damage, its time course, and dose response in a large number of mice. In order to compare this test to other "in-vivo" diagnostic tests, such as conventional X-radiography and nuclear medicine studies, however, larger animals (i.e. dogs) were subsequently used. To further evaluate the technique in a clinical setting, the

densitometry test is applied to radiotherapy patients at different times before and after radiation therapy.

Once the respiratory distress of radiation pneumonitis occurs, treatment is often not effective. However, the treatment of radiation pneumonitis is an area of active research. This provides sufficient incentive to develop an early quantitative assay of the efficacy (and perhaps mechanism) of new treatment methods. With a reliable diagnostic test, more timely intervention may become possible.

The second way to deal with radiation pneumonitis is to reduce its incidence by limiting and controlling the dose delivered to lung. For this purpose it is necessary to have an accurate method of calculating the dose actually delivered to lung. This work also deals with such radiation dose calculations and dosimetry in large (half-body) fields. Various lung dose calculation methods simple as well as complex, are compared to measured doses in simple geometrical phantoms in order to study their range of applicability. These methods are also tested in more complex situations and in a humanoid phantom exposed to 6 MV X-rays.

ACKNOWLEDGMENTS

- Dr. L.D. Armstrong of the Animal Disease Section who performed the autopsy and lung pathology for mice.

- Dr. L. Genest who allowed use of human lung scans for CT densitometry.

- Mr. L. Stenger and the machine shop crew for help in obtaining and making various phantoms.

- Mr. K. Liesner and the audio-visual department for their expert help in the preparation of graphs and figures used in publications and in this thesis.

- Mr. J. Van Dyk and Dr. J. Cunningham who hosted me at the Princess Margaret Hospital in Toronto and provided training and assistance in performing dose calculations with the equivalent TAR method.

- Miss K. Mah who scanned our Rando Phantom on the Picker CT scanner in Toronto.

- Mr. R. Crilly who assisted in obtaining TLD doses.

- Mrs. S. Connors who assisted in obtaining the radiation profiles on the accelerator and also helped in calibrating the CT dose probe.

- Mr. C. Field for his help and advice on use of the VAX computer.

I also wish to thank my fellow graduate students, particularly Dr. A. Zenari and Mr. R. Mackie for many interesting discussions and helpful suggestions, and I thank the medical physics group for having been such a pleasant group to work with for the past four years.

Financial support for this work was provided by the

viii

TABLE OF CONTENTS

LIST OF TABLES

LIST OF FIGURES

1. INTRODUCTION

1.1 Radiation Pneumonitis

In radiation therapy there are many instances in which irradiation of the lung is unavoidable. For example, these include treatments of the lung itself, or of the esophagus, or the breast. In these cases, the tolerance of the lung to radiation usually limits the dose which can be prescribed to the diseased site. However, because only a portion of lung is irradiated, severe respiratory complications can be avoided.

There has been a gradual trend towards the use of larger or "magna" radiation fields which encompass much larger volumes of both lungs. Such irradiation, originally aimed at treating distributed lymph nodes (as in Hodgkin's disease) and reducing the incidence of metastases, has evolved into half-body and total body techniques. Half-body irradiation (HBI) has become a standard procedure for treating widespread metastatic cancer and for relief of pain to improve quality of life during the remainder of the patient's life (100). This technique is also an adjuvant form of radical therapy for oat cell carcinoma as well as Ewing's sarcoma (128). Here, at the Cross Cancer Institute HBI is used in combination with chemotherapy to treat oat cell carcinoma (122). Total body irradiation techniques are also used prior to bone marrow transplantation for leukemia patients

(6,59).

In large field irradiations, large volumes of both lungs are irradiated to a high dose, and there is a potential for severe respiratory complication which may be fatal. The occurence and severity of lung damage is related to the volume of lung irradiated, the total dose, dose rate of delivery, overall duration of radiation therapy, as well as the variable physiological response of individual patients (14,35). When complications develop, the response of lung to such irradiation has been called the " acute pneumonitis syndrome" (28,30) and becomes evident clinically only several months after exposure to the radiation. In humans, the symptoms develop after 1 to 7 months, with a peak incidence occuring near 3 months. Its occurence as a function of dose (delivered in a single fraction) to the entire lung has been documented by Fryer et al.(30) and refined by Van Dyk et al.(128). The clinical symptoms include increasing cough with dyspnea and fever. Chest radiographs taken at this time reveal opacities. Once these signs have developed, the patient's condition deteriorates rapidly and death may ensue within 2 to 3 weeks. In some cases, treatment with antibiotics and prednisone diminishes the severity of the radiation response, and steroid withdrawal may precipitate the syndrome. Chemotherapy, when used in combination with radiation, is also an exacerbating factor (35). If the acute radiation pneumonitis subsides or does not occur,

fibrosis in lung may still occur at later times up to one year after irradiation (86), in which case, this becomes the limiting factor in radiation therapy.

Microscopic findings in humans at autopsy show a combination of the following features: atypical septal cell proliferation, vascular changes, and at later times widespread hyaline membrane formation (14,35). Some degree of fibrosis may be observed in every lung exposed to therapeutic doses of radiation at times of 9 to 12 months after radiotherapy, but the incidence of acute radiation pneumonitis is less common. There seems to be little correlation between the acute syndrome and the later fibrotic changes (14), suggesting that different cells may be responsible for early and late damage. A good review of damage to different cell types in humans as well as animals has been given by Gross (35,38). In the lung, the cells with the highest mitotic rates in which radiation-induced chromosomal damage is expected to be most pronounced are: the bronchial epithelial cells, the capillary endothelial cells, and type-2 pneumocytes. Although these histologic changes in human lung have been observed repeatedly at autopsy, no systematic study has been (ethically) possible, prepneumonitis changes in human lung have certainly not been available. Thus, most of the knowledge obtained on radiation reponse of lung has been acquired through animal experiments and it is not known how well events occuring in animals correspond to events

occuring in humans. Indeed, there is indication that the time course of radiation damage in lung not only differs between humans and animals, but that it also differs within species and even among different strains of mice (24).

Until now the management of radiation pneumonitis has consisted of prevention by reducing the dose to lung or reducing the volume of lung irradiated. As can be seen from the data of Van Dyk (128), the incidence of radiation pneumonitis rises sharply as a function of single dose to total lung, reaching 100% for 11 Gy. However, evaluating dose to lung accurately is a difficult dosimetry problem since there are large differences in lung geometry and density from patient to patient, and there are also variations of lung density even within a patient (125,129).

1.2 Animal Findings

In order to better understand the processes which give rise to radiation pneumonitis, animal models have been developed. Histologic changes in mouse lung following irradiation are well documented, and are listed in Table 1.1. The time course of these changes has been divided into three periods: acute, intermediate, and late (or chronic). The intermediate phase overlaps the acute and late phases. According to Travis (116), the extent of the histological lesions observed in each phase is

dose-dependent, although the time course is not. The threshold dose for acute and intermediate effects in CBA male mice was determined to be 11 Gy, while the threshold dose for late effects was determined to be 13 Gy. For a dose of 15 Gy mortality occurred in the acute phase for all animals (73,116). However, the radiation sensitivity of mouse lung may be different in different strains of mice. The LD(50/160) and LD(50/180) for lung irradiation in different strains of mice have been reported to lie

Table 1.1: Radiation-induced changes in mouse lung

(Adapted from Travis (116) and Maisin (73))

Phase	Time (weeks)	Peak Activity (weeks)	Lesions
Acute	10-30	16-22	Edema
			Macrophage infiltration
			Fibrin in air space
			Alveolar walls thickened
			Lumina reduced to a slit
Intermediate	22-54	36	Increased septal cellularit
			Large cells in air spaces
			and debris
Late	>33	permanent damage	Collagen deposition
			Cells diminished in number

between 13.5 to 16.1 Gy (106,132). Death rates of animal groups is the assay and LD(50/160) and LD(50/180) are the lethal doses required to achieve a mortality rate of 50% assayed at 160 and 180 days, respectively, after irradiation. For Balb/c mice used at our Institute (102), the LD(50/160) was determined to be 13 Gy, in agreement with the above data. Within the acute and intermediate phases, there is a period during which the maximum effect is observed. For the acute phase, this peak response occurs between 16 and 22 weeks. The observations during this peak period correspond closely to those of the "radiation pneumonitis syndrome" in man (30,52). The peak activity for the intermediate phase occurs at approximately 36 weeks. No peak develops for the late stage because fibrosis is a chronic effect resulting from irreversible and cumulative lung damage.

Detection of some lung damage at times earlier than the acute phase was achieved by Sharplin and Franko (102). They found an increase in the mass of lung at 6 weeks after irradiation to lower doses as low as 2 Gy. Their experiments suggest that measurement of lung mass in the "prepneumonitis" period may be a more sensitive and earlier indicator of lung damage. The mass increase was dose-dependent up to a dose of 10 Gy. An increase of 18% in lung mass was detected following irradiation with a dose of 7 Gy, and an increase of 28% was detected with a

Ultra-early changes within 2 weeks after irradiation are possible by electron microscopy as discussed for dogs by Moosavi et al.(77). The capillary endothelium appears to be the initial site of damage. As in the mouse studies,the time course of events is not dose-dependent, but the severity of damage is.

1.3 Diagnostic Tests

Various tests can be used to detect radiation damage to lung, and these are listed in Table 1.2. They are of several categories; morphometric, physiological, biochemical and radiological. The changes occurring in lung, listed in Table 1.1, are all expected to produce an increase in density of lung. Therefore measurement of changes in lung mass and/or density is expected to be a good indicator of lung damage. For this reason, the application of X-ray computed tomography to early detection of pneumonitis was developed in this work (see Chapter 2).

Most of the tests listed in Table 1.2 show a dose-related increase in severity of the effect, and there is a threshold dose below which no changes can be detected. This threshold dose for detection is not the same for all these tests because a different aspect of pneumonitis (i.e. specificity) is being observed and the tests have different sensitivity (i.e. inherent precision). For example, cellular changes are detected

Table 1.2: Tests used to detect radiation damage to lung

Changes in lung	Instrumentation	Reference
A. Morphologic		
1. visible changes in cells at histologic and ultrastructural level	light microscope, electron microscope	35,73,95,116
B. Physiologic		
1. decrease in lung volume and compliance	densitometry, lung mass, spirometry	45,102,104
2. decreased ventilation	133Xe gas inhalation	86
3. vascular changes such as perfusion reduction increased permeability	nuclear medicine alveolar lavage	29,38,45,86
4. increase in breathing frequency at time of pneumonitis	plethysmograph	119
5. changes in arterial blood gases	arterial pH, pO , pCO	86,105
C. Biochemical		
1. surfactant release	radioisotope labelling and alveolar lavage	38,96,97,98
2. phospholipid increase, excess of protein in alveolar fluid	radioisotope labelling	36,37,38
3. collagen deposition (late)	hydrolyzation immunofluorescence	63 76
D. Physical		
1. quantification of edema	lung weight, densitometry	45,102
2. changes in density	X-ray computed tomography Compton tomography	25,45 135,136
E. Radiological		
1. opacities or structural changes	planar X-rays conventional tomography X-ray computed tomography Compton tomography	65,115 79 9

early and at low doses by electron microscopy, whereas
radiological changes appear much later and for greater
doses.

Most of the tests detect the lung damage during the
acute pneumonitis phase. At this time, treatment is often
too late and the course of the syndrome cannot be halted
or reversed. Therefore it might be useful to have
"prepneumonitis" tests that detect lung damage in the
"latent" period of several weeks before the onset of
pneumonitis. Such sensitive tests are the biochemical and
electron microscopy tests which can show changes several
days after irradiation. Also, lung mass increases have
been observed in mouse as early as 6 weeks after
irradiation and at low doses (102).

The tests with earliest detection, (surfactant
release, electron microscopy, and lung mass increase) are
unfortunately invasive and not applicable to the
management of patients developing radiation pneumonitis.
The earliest in-vivo test which can be applied to patients
to monitor lung changes has been described by Prato (86).
Regional blood flow in lung is assessed by injecting
radioactive Xenon-133 dissolved in saline and monitoring
activity over the lung using a gamma camera. A reduction
in activity indicates a reduction in number of particles
reaching lung which in turn signifies a reduction in blood
flow to the lung. A study on radiotherapy patients has
indicated a reduction in blood flow as early as three

weeks after the start of radiotherapy. The limitation of this test is that in patients with lung tumor, it cannot be distinguished whether the changes in blood flow are due to radiation damage or progression or regression of the tumor itself. To overcome this, a radiograph may be taken to localize the tumor and exclude this region during analysis of blood flow.

Another non-invasive method which can locate the tumor as well as detect lung density changes in-vivo is X-ray computed tomography (CT). This method has been used by several authors in the study of human lung and found to be superior to planar chest X-rays. Encouraged by the early increases in mass observed by Sharplin and Franko (102), the present work was initiated in order to determine whether the increase in mass observed early after irradiation might also be detected as an increase in density by using such CT scans. This test will be described in detail in Chapter 2.

In all tests, the aim is to quantify early lung damage non-invasively, and to establish whether such damage is predictive of later treatment complications (117). It is assumed that an early signal of severe lung damage exists during the "latent" period. Then procedures and drugs designed to modify this response might be actively sought so that the clinical symptoms of radiation pneumonitis may be relieved or avoided altogether. The non-invasive methods would then monitor the effectiveness

of any strategy used to reverse or suppress radiation pneumonitis.

1.4 Treatment of Radiation Pneumonitis

Since an inflammatory reaction is part of radiation pneumonitis, corticosteroids are expected to suppress this reaction, because these drugs are anti-inflammatory, suppressing connective tissue reactions and decreasing cellular infiltrations. Indeed, prednisone administration prior to irradiation and until 60 days after was found to reduce mortality due to radiation pneumonitis (35). Cortisone has been found to reduce the severity of the radiation response in lung assessed by measuring changes in total chest compliance in rats (78). If steroids are withdrawn in patients already on steroid therapy, the symptoms of radiation pneumonitis are aggravated. Antibiotics have no effect on the radiation response but are beneficial in minimizing opportunistic infections which are often concurrent with pneumonitis. Radioprotective or radiosensitizing agents which render lung tumors more sensitive to radiation than normal lung tissue can be considered to reduce incidence of radiation pneumonitis. Fractionated radiotherapy instead of single doses causes more damage to tumor relative to normal lung tissue due to different repair capacities (32,84). A preliminary study using a Chinese herb medicine named HH-6075 to modify radiation response of lung was reported

by Shen and Liu (68,103). Radiation changes were observed in rat lungs by microscopy and electron microscopy. Lung damage was observed to be much less severe at all times after irradiation in the treated rats. The proposed mechanism of action of this medicine is prevention of blood vessel spasms, an anti-inflammatory action and inhibition of collagen production. None of these treatments consider all aspects of radiation pneumonitis and therefore radiation pneumonitis and its treatment is still an area of active research. This has provided sufficient incentive to develop early detection techniques which will permit more timely intervention, and assay the efficacy of treatment methods under investigation.

1.5 Guide to Thesis

In this thesis radiation pneumonitis is dealt with in two ways. In Chapter 2 a non-invasive quantitative test based on X-ray computed tomography for detecting lung damage early after irradiation is investigated. The reaction of the lung to radiation is monitored in groups of animals which have been irradiated to various single doses to the thorax.It is determined how well this test can detect radiation damage, its time course, and dose response. For this part of the work, large numbers of animals were required so that mice were used. In order to compare this test to other in-vivo tests, such as conventional X-radiography and nuclear medicine studies,

however, larger animals (i.e. dogs) were required. To further evaluate the technique in a clinical setting, the densitometry test has been applied to radiotherapy patients at different times after therapy. How well CT monitors lung density changes in these cases is reported in section 2.4.

In Chapter 3, radiation dosimetry in large half-body fields is dealt with and various methods to calculate accurately the dose to lung per se are intercompared. The various lung dose calculation methods are compared to measured doses in simple geometrical phantoms in order to study their range of applicability. These methods have also been tested in a humanoid phantom. A detailed dose distribution in a transverse slice of the phantom is calculated and compared to measured dose values, and to the "manual" planning methods presently used for hemi-body irradiation at the Cross Cancer Institute.

2. DETECTION OF LUNG DAMAGE BY COMPUTED DENSITOMETRY

2.1 X-ray Computed Tomography (CT)

2.1.1 Principles

X-ray computed tomography (CT) is a body imaging technique that permits viewing of a cross-section or "slice" without interference from adjacent layers. X-ray transmission measurements made at several angles or projections through a plane of interest, may be used with an appropriate algorithm to synthesize the contents of the layer of interest. This technique is significantly better in terms of tissue contrast resolution in comparison with radiography and conventional focal-plane tomography. However, it does not compete with film imaging techniques in terms of spatial resolution (at high contrast). Thus computed tomography is particularly suitable for imaging soft tissues (e.g. lung), while film radiography and tomography are more suitable for diagnosing bone fractures.

The mathematics of construction of an image of an object from projection data obtained at a number of angular views was first developed in 1917 by Radon (87). Other techniques were developed in 1956 by Bracewell working in radioastronomy (15). In 1975, Gordon et al. cited more than 1500 references related to image construction (34)!

The first medical application of image synthesis from

radiological projections was published by Oldendorf in
1961 (81). Other important experiments were carried out
in 1963 by Kuhl and colleagues utilizing a tomographic
image scanner for radionuclide detection (61), and by
Cormack using radiographic techniques (18,19). Hounsfield
pioneered the first clinically useful computed tomography
system, and it was installed in 1971 in the Atkinson
Morley Hospital near London, England (2,47).

2.1.2 Transmission Data Acquisition

The simplest CT system consists of an X-ray tube
collimated to produce a pencil beam incident on a
detector. The plane to be scanned is placed between X-ray
tube and detector as shown in Figure 2.1. The first step
is to move the X-ray tube and detector assembly linearly
across the object for a fixed angle. Readings are
obtained at a large number of points during the linear
motion, and the fluence profile of the transmitted X-rays
is detected to form a projection. When a linear scan is
complete, the tube and detector rotate together through a
small angle and the linear scan is repeated. In this same
manner, many sets of projections are measured. If one
defines a coordinate system X-Y through the object, then
each point along the ray is specified by its coordinates
x,y and a function $\mu(x,y)$ is defined at every point. For
X-ray transmission measurements, this function is actually
the linear attenuation coefficient $\mu(cm^{-1})$. The line

integral of $\mu(x,y)$ along a path ds is called a ray-projection p: (16)

$$p = \int \mu(x,y) \, ds$$

For monoenergetic photons, the transmitted beam fluence Φ_t is given by:

$$\Phi_t = \Phi_o \exp \left[-\int \mu(x,y) ds \right]$$

where: Φ_o is the incident beam fluence.
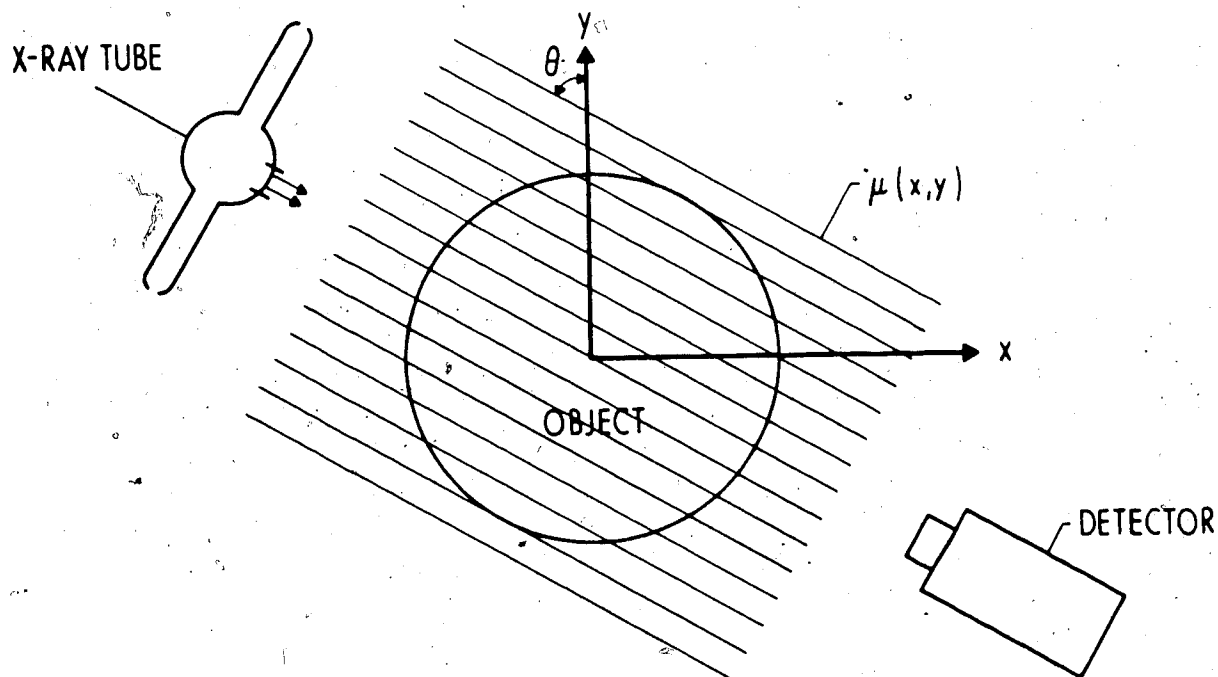
Fig. 2.1 Simplest CT system consisting of X-ray tube and detector moving linearly across the object, and then rotating about the object.

Therefore the ray-projection is measured as:

$$p = -\ln (\Phi_t / \Phi_o)$$

The ray-projections p from many directions can be stored in a computer and the problem is then to invert a large number of such measured ray-projections, p, to solve for $\mu(x,y)$. Actually the rays are of finite widths and the μ's obtained are the average μ in a volume element (voxel) of finite volume. The reconstruction process then, will create a map of μ's throughout the irradiated plane.

2.1.3 An Image Reconstruction Technique

Suppose there is an object with a dense pin at its centre. Views from several angles will give the projection profiles shown in Figure 2.2. A first attempt at reconstruction would be to "back-project" these profiles (i.e. evenly distribute the profile value along a ray). Summing back-projections from all directions gives a star-like image as shown in Figure 2.3. This, however, is a blurred image of the pin; the image contrast is impaired and the true nature of the real object is obscured. This image can be deblurred or deconvolved by pre-filtering each profile prior to back-projection and summation. In our example, Figure 2.2, the profile would be filtered so that it had both negative and positive lobes as shown in Figure 2.4. When
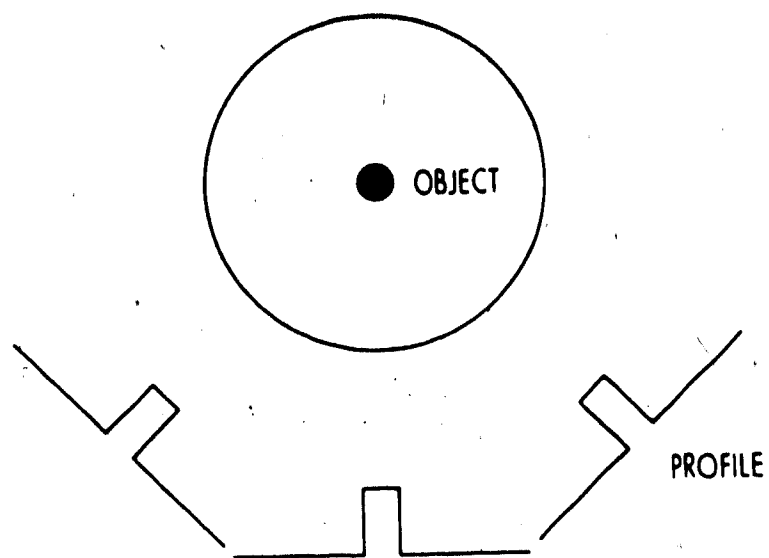
Fig. 2.2 Projection profiles of an object with a

dense pin.
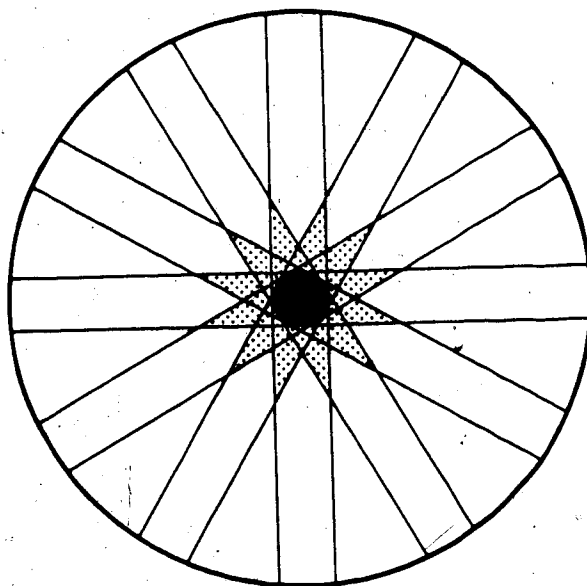
Fig. 2.3 Image of a dense pin formed by simple back-

projections. Note the "star"-like artefact.
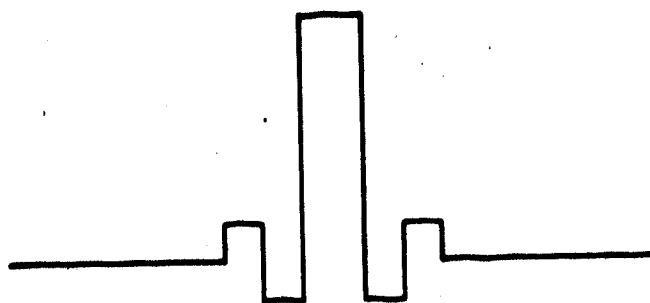
Fig. 2.4 Profile after modification with a filter
          function.

the filtered back projection values are then summed, the
negative values cancel positive values and the spokes of
Figure 2.3 disappear. If the filter function is correct,
the cancellation will be exact, and the reconstructed
image will be a correct image of the object (31). This
procedure is now used on all commercially-available CT
scanners.

2.1.4 GE CT/T 8800 Scanner

    The scanner used in our experiments is a " third
generation" scanner which uses an incident fan beam of
X-rays, multiple detectors and rotational motion only to
acquire data. Elimination of the linear motion makes
scanning possible in less than 10 seconds per slice. This

type of scanner is illustrated in Figure 2.5. The detectors are arranged on an arc which rotates with the X-ray tube about the patient. The patient is on a table which can be moved longitudinally through the opening (or "donut") in the gantry to produce a series of slice images.

The X-ray tube delivers a pulsed beam of X-rays collimated to a wide fan beam. The generator-tube combination permits variation in the current up to 600 mA per pulse, but the voltage is fixed at 120 kVp. The number of pulses per rotation may be selected as either
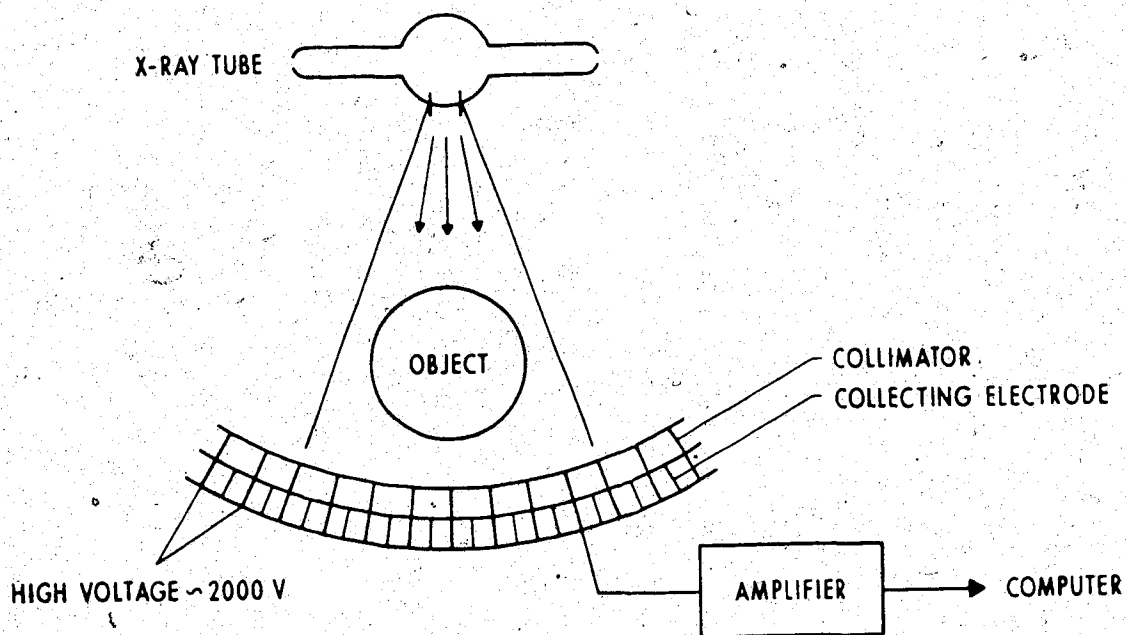
Fig. 2.5 Third generation CT scanner using fan beam of X-rays, array of detectors and rotational motion only.

288 or 576, and the pulse duration is variable up to 3.3 msec.

The original (Hounsfield) CT scanner used one sodium iodide detector coupled to a photomultiplier tube. Other scintillator crystals such as cesium-iodide, bismuth-germinate, and cadmium tungstate have since been used to achieve better light conversion and response times. The main disadvantage of using crystals and photomultipliers, however, is that it is difficult to "pack" many of these closely enough (eg. 2 mm) to achieve high spatial resolution. More specifically, photomultipliers cannot be made smaller than 1 cm in diameter and are expensive (53,54). For this reason, photodiodes are used instead of photomultipliers on some scanners.

An alternative approach is to use a fan array of ion chambers filled with pressurized Xenon. Each detector element is about 25 mm long with an aperture of 1.05x1.05 mm². Each ion chamber consists of a planar collecting electrode between two tantalum or tungsten plates, filled with Xenon at 27 atmosphere or more. Such a chamber can absorb more than 70% of the incident radiation energy (53,54).

The General Electric CT/T 8800 system used in our experiments uses the components listed in Table 2.1.

Table 2.1: Components of the General Electric CT/T 8800
         scanner

Tube type	Rotating anode
Detector type	Xenon ion chambers
Detector elements	523 of which 12 "end" detectors provide reference readings
Rotation	360°
Scan time (sec)	4.8 or 9.6
Number of pulses/rotation	288 or 576
current/pulse	up to 600 mA
pulse duration	1.1 or 2.2 or 3.3 msec
voltage	120 kVp (fixed)
image matrix	320x320
pixel size	0.8, 1.1, 1.3 mm

2.1.5 Tissue Densitometry

Rather than specifying the μ's, a related quantity,
the CT number N_{CT} has been defined as:

$$N_{CT} = 1000 \left(\frac{\mu - \mu_w}{\mu_w} \right) \tag{1}$$

where:

$N_{CT} =$ the CT number in Hounsfield (H) units

$\mu =$ linear attenuation coefficient (cm^{-1}) of
imaged tissue

μ_w = linear attenuation coefficient (cm^{-1}) of water. On this scale then, each Hounsfield unit is equivalent to 0.1% of the attenuation coefficient of water. Thus, the CT number scale is fine enough to distinguish fractional percent changes in the attenuation coefficient of tissue. Air with negligible attenuation has N_{CT} = -1000, and dense bone approaches +1000. Most "soft" tissues lie within -100 to +100 Hounsfields, except for air-filled lung which has a typical CT number value of -750.

The two-dimensional matrix of CT numbers may be displayed as a grey-level or colour image on a video screen where each picture element (or "pixel") is assigned a shade of grey or colour, depending on its CT number value. The range of CT numbers displayed on the grey scale is determined by setting a window, while the level specifies the CT number value assigned ███ mid-grey tone.

μ as well as CT number depend on the type of tissue and on the incident photon energy. However, an advantage in the use of the CT number instead of μ is that it is less dependent on the effective energy of the incident beam. This is because the ratio μ/μ_w varies much less with change in photon energy than does μ. In the diagnostic energy range used in computed tomography (60 to 80 keV), there are three important mechanisms of photon interaction with tissue: Rayleigh scattering, photoelectric absorption, and Compton scattering (54,75).

The relative importance of each of these processes for a typical energy of 65 keV (e.g. X-ray tube operated at 120 kVp) is shown in Table 2.2. The total attenuation coefficient due to all three types of competing interactions is

Table 2.2: Relative importance of Rayleigh scattering, photoelectric absorption, and Compton scattering to total attenuation at 65 keV (9,75)

Type of interaction	contribution to total attenuation at 65 keV		depends on:
	muscle	bone (ICRU)	
Rayleigh	4%	6%	ρ_e Z^2 $1/E^{1.9}$
Photoelectric	7%	28%	ρ_e Z^4 $1/E^{3.2}$
Compton	89%	67%	ρ_e Z^0 $f(E)$

where:

ρ_e = electron density (e/cm³)

ρ = physical density (g/cm³)

N = Avogadro's number

Z = atomic number

A = mass number

ρ_e = (NZ/A)ρ

E = photon energy

$$\mu = \rho_e \left[\sigma_R^e(\widetilde{E}, \widetilde{Z}_R) + \sigma_\tau^e(\widetilde{E}, \widetilde{Z}_\tau) + \sigma_C^e(\widetilde{E}) \right] \qquad (2)$$

where σ^e and $\widetilde{Z}$ are the electronic cross section (cm^2 /e) and effective atomic number for each type of interaction. Then, using equation (1) and (2) one can obtain the electron density of tissue, relative to water, ρ_e' as (9):

$$\rho_e' = \rho_e / \rho_{ew} = R_\sigma (1.000 + 0.001\ N_{CT}) \qquad (3)$$

where R_σ is the ratio of total electronic cross-section for water to the total electronic cross section for tissue. In order to convert CT numbers to relative electron densities, R_σ must be known for different tissue compositions. For air, lung, and muscle R_σ is unity (9). Thus, for "soft" tissues with atomic composition similar to that of water, the CT numbers can be converted to relative electron densities according to:

$$\rho_e' = 1.000 + 0.001\ N_{CT} \qquad (4)$$

The above equation has been tested for various tissue-substitute materials (82), and for tissues in-vivo (9). For water-like tissues, it was found experimentally to be accurate to better than 3% (11). For tissues which differ from water in chemical composition (e.g. bone) however, the influence of atomic number is seen. For such tissues, R_σ must be pre-established with appropriate tissue- substitute materials or measured in-vivo using

dual energy CT scanning (9).

The gravimetric density of tissue is obtained from the electron density using the following relation:

$$\rho = \rho_e' \left[\frac{(NZ/A)_{water}}{(NZ/A)_{tissue}} \right] \tag{5}$$

If lung tissue is considered to be a mixture of air and water-like tissue, where the fraction of air by weight is negligible, then:

$$\left[\frac{(NZ/A)_{water}}{(NZ/A)_{tissue}} \right] = 1.00$$

and from equations (4) and (5), it follows that

$$\rho = 1.000 + 0.001\ N_{CT}. \tag{6}$$

Because CT numbers can be converted to tissue densities in lung, one has for the first time the possibility of obtaining quantitative values for lung density in-vivo. However, the lung is an inhomogeneous organ, with local density varying between that of air to that of soft tissue and blood: the composition includes blood vessels, air spaces of the alveoli and bronchi, and lung parenchyma. Therefore one is faced with the problem of choosing which lung region to sample in order to obtain a representative average density. In addition to spatial density gradients throughout the lung, density changes

occur with time during the breathing and cardiac cycles; such variations have been measured by CT for inspiration, expiration, and continuous breathing by Van Dyk et al. (129). In our experiments, several methods of obtaining an average density for lung were investigated, including sampling of small areas or linear profiles of the lung image. However, outlining the complete lung area, and averaging density therein, provided the most reproducible (although not the most sensitive) method. This method can also be extended to yield a measure of the proportion of overall lung area which has an altered density. This subject is discussed further in section 2.1.6.

The method of quantitative CT densitometry is applicable to diseases affecting the entire lung such as interstitial disease which includes pneumonitis and fibrosis, and diseases affecting the general fluid or air content of the lung (136). The method would be less suited to measure densities of very localized lesions because it would be difficult to reproduce the scan site and to avoid partial volume effects.

In summary then, CT densitometry of lung can be used to diagnose lung abnormalities such as interstitial disease, radiation injury (pneumonitis and fibrosis), edema, and emphysema. CT can also be used to record changes in physiological function of lung since diseases affect pulmonary perfusion and/or ventilation. CT densitometry has already been used in animal and human

studies as a non-invasive sensitive method for detecting small changes in lung density (see Table 2.3).

Recently CT has also become a useful tool for planning radiotherapy. As well as providing detailed three-dimensional internal anatomical data for the individual patient, it gives the electron densities of the inner structures which are necessary for accurate dose calculations (11,129).

2.1.6 Precision

For each scan session, pins of known material surrounded by water were placed in the scan field. The CT numbers of each pin as well as of the surrounding water were measured, thus providing a check on long-term reproducibility and scanner stability. Results are shown in Figure 2.6. Each point represents the average CT number for a particular pin for about 30 slices taken on the date indicated. The number of pixels per sampled region was 120. The "slice" dose per scan was 3.9 $\pm$ 0.1 cGy. The standard deviation in the average CT number for various materials for 30 slices was found to be ± 3 H, which corresponds to an uncertainty of $\pm 0.6\%$ for a lung density of 0.5 g/cm^3. This is the inherent precision or "noise" of the scanner when used for densitometry of inanimate specimens.

There is a loss in precision associated with reproducibly defining the sample region of interest. For

Table 2.3: Densitometry of lung

Species	Lung status	Remarks	Reference
human	emphysema and normal		Rosenblum (92)
human	normal		Rosenblum (93)
human	"normal"		Van Dyk (129)
human	abnormal lung		Wegener (136)
human	normal and abnormal	Xenon inhalation pulmonary ventilation	Herbert (44)
human	abnormal	Compton densitometry computed tomography	Dohring (23)
human	normal	changing air volume	Robinson (91)
human	radiation damage		Nabawi (79)
mouse	radiation damage		El-Khatib (25)
			Van Dyk (127)
rabbit	radiation damage	compare CT to X-ray and scintigraphy	Hermann (45)
dog	edema	oleic acid injury	Hedlund (40)
dog and baboon	changes in density due to changes in blood, extravascular fluid, or gas content		Hedlund (42)
dog	changes in density due to hemorrhage and rescuscitation		Hedlund (41)
primate and sheep	regional ventilation	Xenon inhalation	Gur (39)
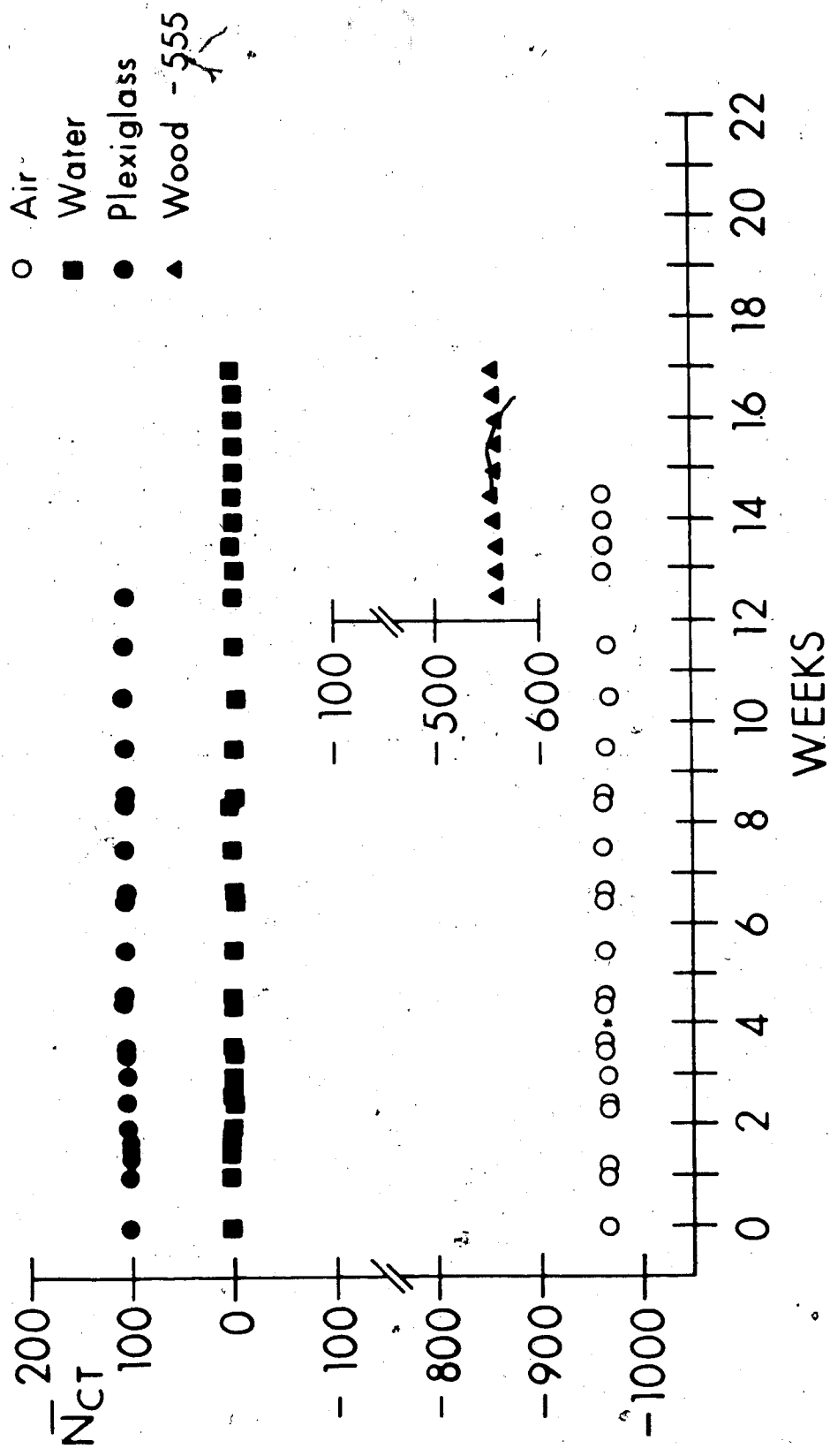
Fig. 2.6 The reproducibility of CT numbers over a period of 17 weeks.

an objective trace of the lung outline, it was necessary to standardize the viewing "window" and "level" settings (60). Using simple test objects, the best correlation was found between the traced area and the true area for a level setting half-way between the CT value of the structure of interest and that of the surrounding material. The window setting did not affect the area as significantly. Several tests were then performed in order to determine the most reproducible method of obtaining the average CT number (N_{CT}) of the sample region of lung in-vivo (92,129,136). The following methods, illustrated in Figure 2.7, were considered:

(a) adjust the level as above and trace close to the visible boundary of lung (2 users),

(b) place a rectangular region of interest (ROI) box inside the lung and obtain the average CT number therein,

(c) place a ROI inside lung, obtain the average CT number therein ($N_{CT} \pm \sigma$) where σ is the standard deviation. Then find all pixels having CT number values within $N_{CT} \pm 2\sigma$, and recompute the average.

(d) Print out the CT numbers for the lung region and calculate N_{CT} along a linear profile through lung.

These four methods were studied on a normal and an abnormal mouse lung. Results are shown in Table 2.4. The σ reported there is the standard deviation of the mean for numerous trials of each method and is thereby an indication of the reproducibility of each tracing method

(a)

TRACE

(b)

(c)

ROI BOX

(d)

PROFILE

POSITION

NCT
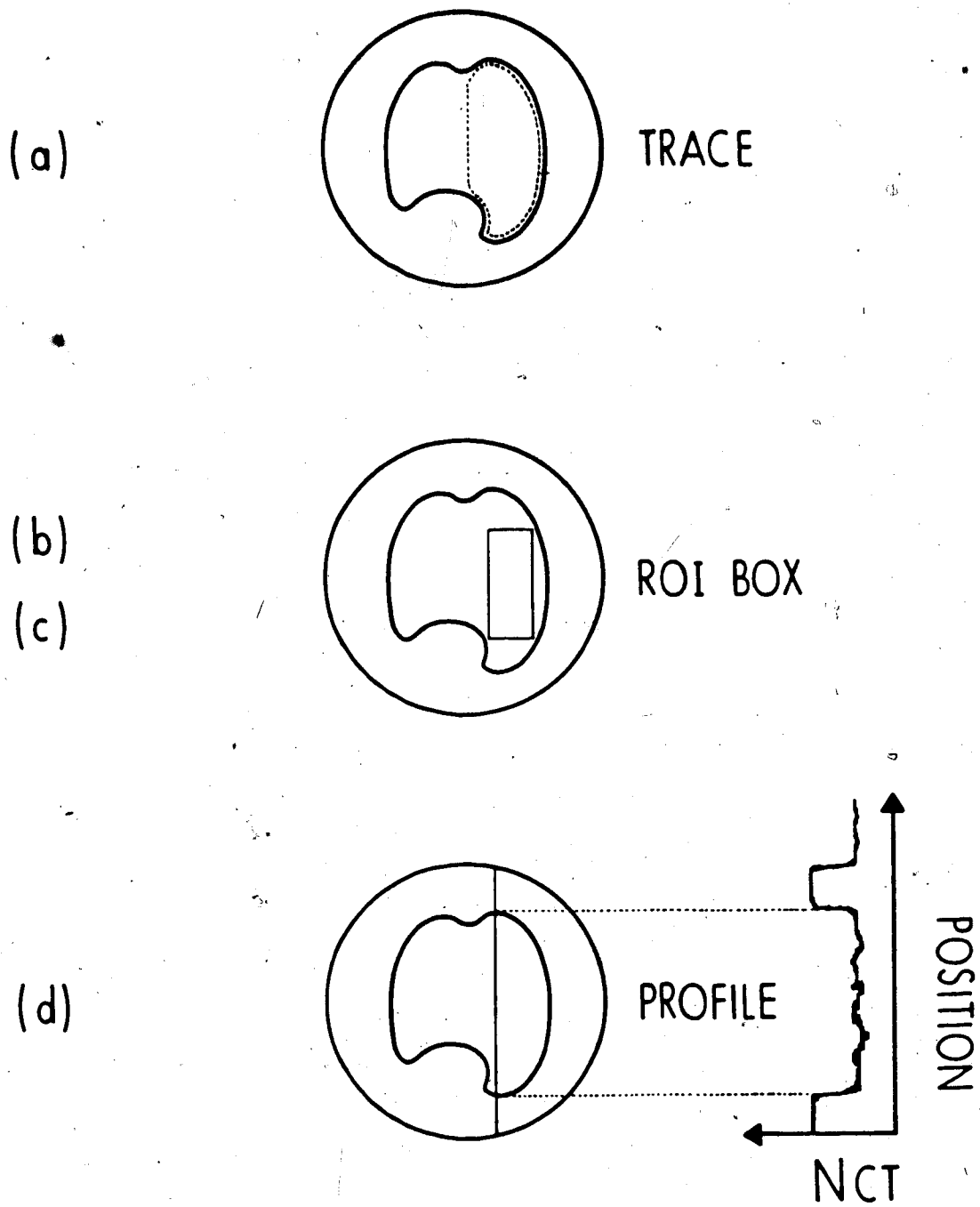
Fig. 2.7 Various sampling methods used to determine
the average density in lung.

Table 2.4: Average CT number as determined by various sampling tests

Method	Normal lung		Abnormal lung		Comments
	N_{CT}	σ	N_{CT}	σ	
(a)	-517.12	1.24		2.60	Sample entire lung Best reproducibility.
(b)	-534.13	10.47	-285.26	60.41	too dependent on position of region of interest
(c)	-522.38	9.86	-300.72		may exclude structures in abnormal lung
(d)	-485.45	36.45	-310.35	34.	position of profile chosen arbitrarily

per se. From this Table, it is apparent that method (a) is the most reproducible and objective for normal as well as abnormal lung.

In the dogs, the reproducibility of the scan site as well as the tracing procedure was verified by repeat scanning on the same dog on the same day. There were eight 1cm slices through the thorax from apex to diaphragm, the sternal notch being designated as origin. The average CT number N_{CT} was obtained for right and left lung in each slice. For both scans, CT values for right and left lung as well as area traced were compared for the eight nominal positions. The maximum difference in N_{CT} of a given slice was 27 H, but most differences were within 10 H. The average CT number $\overline{N}_{CT}$ for all slices for the dog was -798.81±57.3 in the right lung, and -777.72±45.11 in the left lung. On the repeat scan the average CT numbers were within 10 H of these values. The difference in average CT number for the entire dog lung therefore was 10 Hounsfields, which represents 5% in lung density. If one slice through a highly vascular area of dog lung is traced ten times according to method (a), Table 2.4, a standard deviation of 4.3 H in the mean CT number for the slice was obtained, indicating the reproducibility of the tracing method alone.

In the human, a repeat trace of the same slice ten times according to method (a) gave a standard deviation of 1.4 H in the mean CT number for the slice. This is lower

than for the dog due to the fact that the CT slice of human lung is more homogeneous and the boundary is better defined. Therefore we conclude that the reproducibility of method (a) is very good and this is the method adopted throughout this work. However, the sensitivity of this method in detecting localized changes is not very good, since these are diluted by the averaging procedure. Visual CT interpretation can be more appropriate for this case because pattern recognition is exercised by an experienced radiologist. CT densitometry is more suitable to detect subtle diffuse changes throughout the lung.

2.1.7 Accuracy

To obtain densities from CT numbers the following steps discussed above are used:

$$\mu / \mu_w \xrightarrow{\quad} N_{CT} \xrightarrow{R_\sigma} \rho_e / \rho_{ew} \xrightarrow{\dfrac{(NZ/A)_{water}}{(NZ/A)_{tissue}}} \rho$$

The errors involved in obtaining CT numbers from μ / μ_w will be due to beam hardening effects, system noise, and motion-induced artefacts (64,74,75). These must be checked for each system and may vary depending on size of object, motion, and scanning technique (eg. kVp). The conversion to relative electron density is performed using equation (3). Gravimetric densities are obtained from relative electron densities using equation (5) of section 2.1.5. Values of R_σ, $\dfrac{(NZ/A)_{water}}{(NZ/A)_{tissue}}$, relative electron

density, and gravimetric density for water, air, muscle, and some tissue-substitute plastics at an effective CT energy of 65 keV are given in Table 2.5. Often R_σ and $\dfrac{(NZ/A)_{water}}{(NZ/A)_{tissue}}$ are assumed to be unity and densities are obtained simply from equation (6) of section 2.1.5. The errors introduced by this simpler procedure for various materials are shown in Table 2.6. The densities calculated in this way are all underpredicted, relative to the true density. However, for soft tissue (e.g. muscle and lung) the underprediction is very small (0.7%). If greater accuracy is required, this offset could be corrected for. In this work, fractional changes in density, $\Delta\rho / \rho$, were measured and this correction was not applied.

In order to test the above theory, materials of known densities were scanned (see Table 2.7). Results are shown plotted in Figure 2.8. The cork and polystyrene values were obtained from several slabs of variable thickness (e.g. 0.5 cm) and with small inherent density differences. These slabs were piled and scanned. The cork slabs were variable in consistency and density, as well as having uneven edges. This made comparison of the measured density (sample volume 200 cm^3) to the CT calculated density (sample volume 5 cm^3) difficult. The composition of cork and wood is unknown, therefore R_σ and $(NZ/A)_{tissue}$ cannot be determined but setting them equal to 1 as in equation (6) gave acceptable agreement. This

Table 2.5: Physical quantities used in conversion of CT numbers to density

	Water	Air	Muscle	Polystyrene 1% TiO$_2$	Polystyrene clear	Polystyrene 4% TiO$_2$	Lucite	Nylon	Polyethylene
μ/ρ	0.1993	0.1810	0.1982	0.1855	0.1826	0.1942	0.1873	0.1893	0.1937
(NZ/A)x10^{23} (e/g)	3.343	3.006	3.312	3.234	3.238	3.222	3.248	3.2926	3.4457
σ_{tot}^{e} x10^{-23} (cm²/e)	0.0596	0.0602	0.0598	0.0574	0.0564	0.0603	0.0577	0.0575	0.0562
R_σ	1	0.990	0.997	1.038	1.057	0.988	1.033	1.037	1.060
$\frac{(NZ/A)_{water}}{(NZ/A)_{tissue}}$	1	1.112	1.009	1.034	1.032	1.038	1.029	1.015	0.970
ρ_e/ρ_{ew}	1	0.001	1.03	1.016	1.01	1.04	1.15	1.13	0.94
ρ	1	0.001	1.04	1.05	1.05	1.08	1.19	1.15	0.92
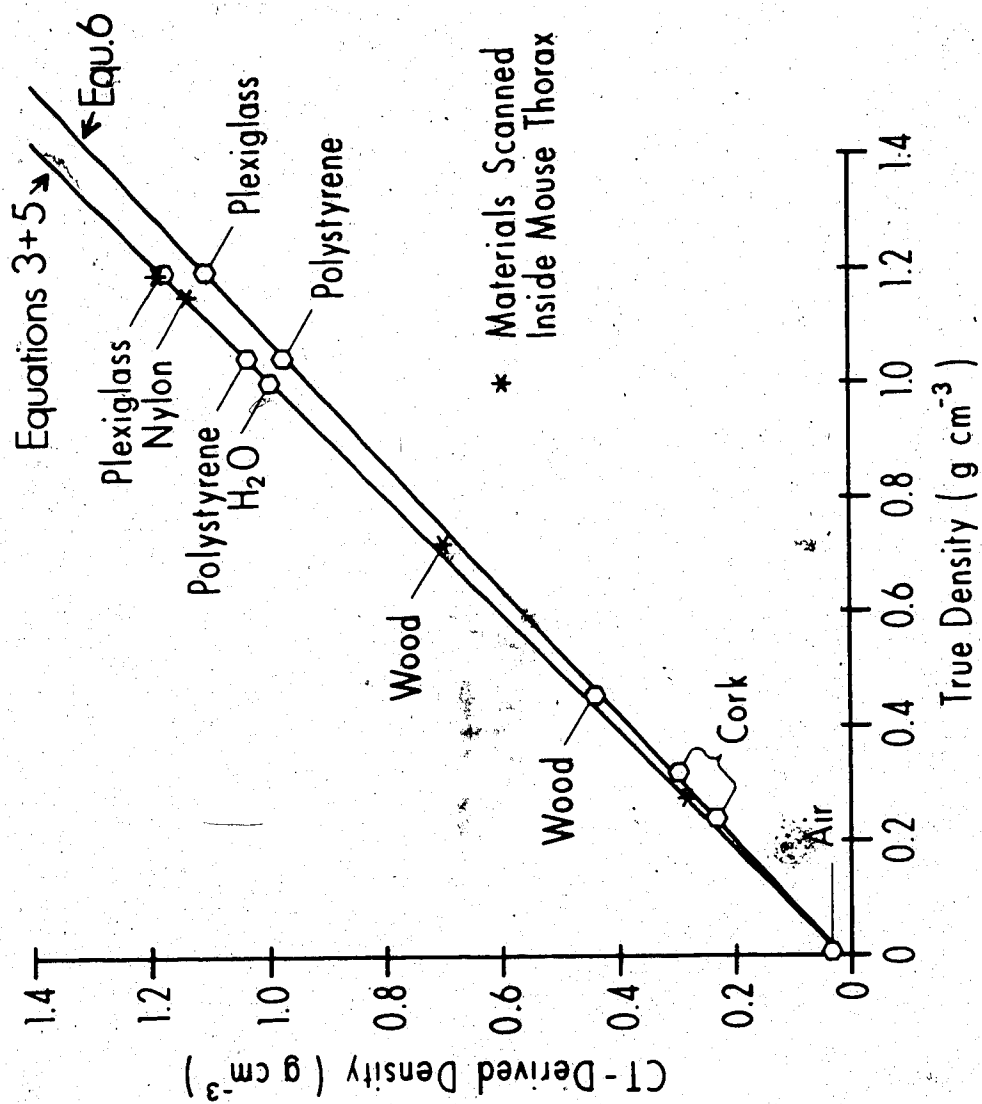
Fig. 2.8 Calculated versus measured densities for several tissue-substitute materials.

is reasonable since wood and cork are probably water-like biological materials. There was also an uncertainty in the physical density measurements ($\pm 7\%$) and variations in density from slab to slab. The polystyrene used was the opaque polystyrene containing a TiO_2 filler whose concentration may vary up to 4% by weight (137). The exact amount is unknown. In Table 2.7 density values for polystyrene are calculated assuming filler concentration of 1% and 4%.

In order to study the influence of sample size on accuracy of CT number, a test was performed in which three

---

Table 2.6: Conversion of CT numbers to densities

	$\mu / \mu_w \longrightarrow \rho_e / \rho_{ew} \longrightarrow \rho$		overall error, if equation (6) used instead of equations (3) and (5)
Air	+1%	-11%	-10%
Muscle	+0.3%	±1%	-0.7%
Lung	+0.3%	-1%	-0.7%
Polystyrene			
clear	-6%	-3%	-9%
Poly.+1% TiO_2	-4%	-3%	-7%
Poly.+4% TiO_2	+1.2%	-4%	-3%
Lucite	-3%	-3%	-6%
Nylon	-4%	-1.5%	-5.5%
Polyethylene	-6%	+3%	-3%

Table 2.7: Calculated and measured densities for several tissue-substitute materials

	N_{CT}	σ	calculated using equation (6) $\rho(g/cm^3)$	calculated using equations (3) and (5) $\rho(g/cm^3)$	measured $\rho(g/cm^3)$	agreement
Water	-0.97	2.6	.999	0.999	1.0	0.1%
Air	-964.92	1.5	0.035	0.039	0.0013	7.3%
Plexiglas	105.28	1.0	1.105	1.175	1.192	2.4%
Wood	-557.99	2.6	0.442		0.453	
Polystyrene	-28.03	4.8	0.972		1.04	0%
Poly.+1% TiO_2				1.04		4%
Poly.+4% TiO_2				0.997		
Cork (max)	-700.9		0.30		0.32	6%
Cork (min)	-770.0		0.23		0.24	4%

small cork cylinders of diameters 6 mm, 1.25 cm, and 1.9 cm were inserted in plexiglas sleeves of outer diameter 2.54 cm. These were then inserted in a water phantom and scanned. Results indicated variations of less than 12 H for sampled regions ranging from 0.045 cm^3 to 0.375 cm^3.

As a final test, 4 cylinders of materials of similar volume as mouse lungs were substituted into the mouse thorax. The mice were placed in the phantom and scanned in the usual manner. Results are included in Figure 2.8. This indicates that the calibration linearity of CT-derived density is maintained whether the samples are within the mouse or within calibration phantoms. The errors involved in obtaining lung densities from CT numbers are summarized in Table 2.8.

Table 2.8: Summary of errors involved in obtaining lung densities from CT numbers

Source	Error
Scanner instability	± 0.6%
Reproducibility of the tracing procedure for:	
mouse lung	± 0.003%
dog lung	± 0.017%
human lung	± 0.007%
Accuracy of the conversion of CT numbers to densities	± 0.7%

2.2 Experiments with Mice

This study was initiated in order to investigate whether the increase in mass observed early after irradiation (102) might also be detected in-vivo as an increase in density by CT scans. The mass increase of 18% observed at 6 weeks post-irradiation to 7 Gy by Sharplin et al. (102) would be easily detected by CT, assuming lung volume does not change. The work described in this section (2.2) has been published in the International Journal of Radiation Oncology Biology and Physics (25).

Female mice of the Balb/c Cr strain were obtained from the Small Animal Program of the University of Alberta. Mice weighing between 19 and 23g were irradiated at 12 weeks of age. In order to minimize the risk of infection, oxytetracycline at a concentration of 425 mg/liter was added to the drinking water. Tetracycline controls most bacterial infections in laboratory mice, but does not control mycoplasm – a common virus infection in pneumonitis. Autopsies of sample animals, however, revealed no bacterial or mycoplasm infections. Thus, density increases could be attributed solely to the effect of the irradiation.

2.2.1 Methods

The mice were irradiated with an X-ray unit (Picker Vanguard) using the parameters given in Figure 2.9. The mice were restrained at the neck in a plastic jig
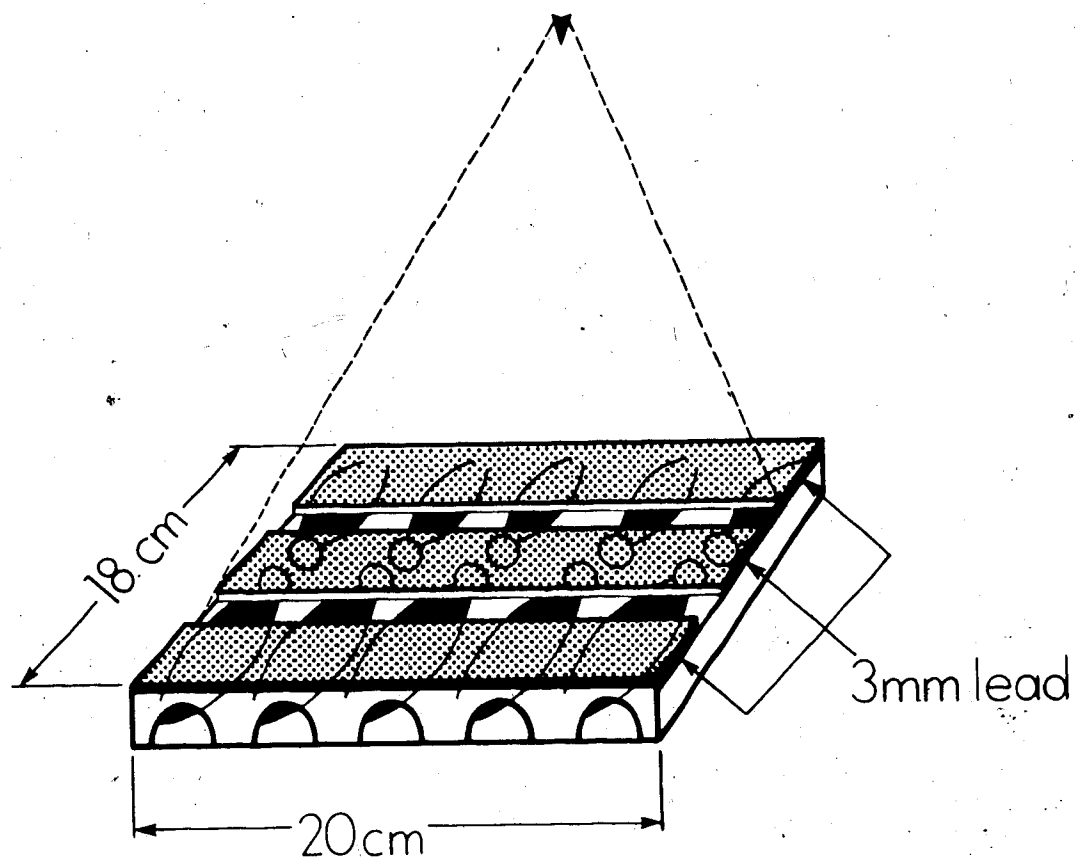
Fig. 2.9 Mice in the irradiation jig. The thorax
was irradiated, while the abdomen and
head were shielded by 3 mm of lead.
X-ray technique: Tube voltage: 260 kVp;
Tube current: 19 mA; Half-value layer:
1.1 mm Cu; Field size: 20x20 cm^2; SSD: 50 cm.

described elsewhere (102). The unanesthetized animals were placed securely in individual "half-tunnels" Figure 2.9. All parts of the mice except the thorax were shielded by 3 mm of lead to reduce the body dose to 4.1% of the lung dose. The mean dose rate was 0.73 Gy per minute with a dose uniformity of ± 0.04 for the 20×20 cm^2 field used. This was measured using an air ionization chamber in conjunction with an electrometer (Capintec Model 192).

The phantom which is recommended by the American Association of Physicists in Medicine for CT scanner performance evaluation (55) was modified to hold the mice during the imaging session (see Figure 2.10). An acrylic resin (Lucite) end plate with nine tubes, 2.8 cm in diameter, and each 8 cm long was constructed. In addition, acrylic resin cylinders of smaller diameters were constructed; the mice slipped easily into these inner cylinders, which were then inserted into the outer "sleeve" tubes. The mice were reasonably well immobilized without anesthetic and without having any part of their body tied or compressed.

Five slices, each 1.5mm in thickness, and spaced 2mm apart spanned the complete mouse lung longitudinally from apex to diaphragm. A slice through the phantom with all mice in place is shown in Figure 2.11. The appearance of the CT slices at various positions in the lung is shown in Figure 2.12. The data presented here were obtained from

45

Fig. 2.10 Animals in phantom for CT scanning.

46
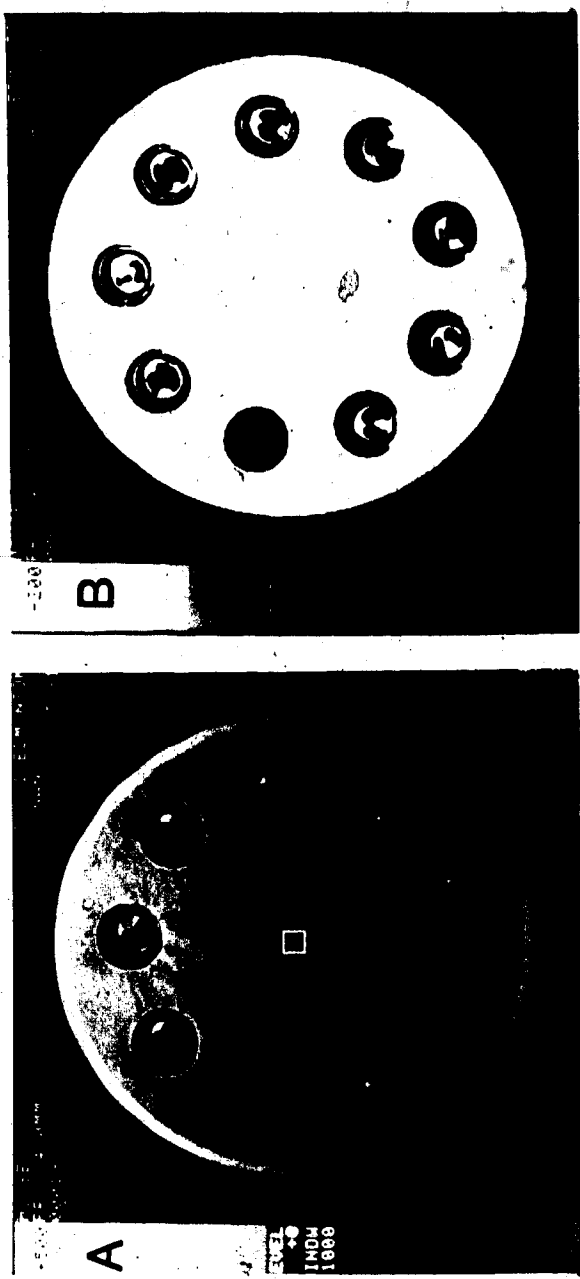
Fig. 2.11 A CT slice through the phantom with all mice in place;

(A) with a level setting of 0 H and a window setting of 1000 H,
(B) with a level setting of -250 H and a window setting of 100 H.
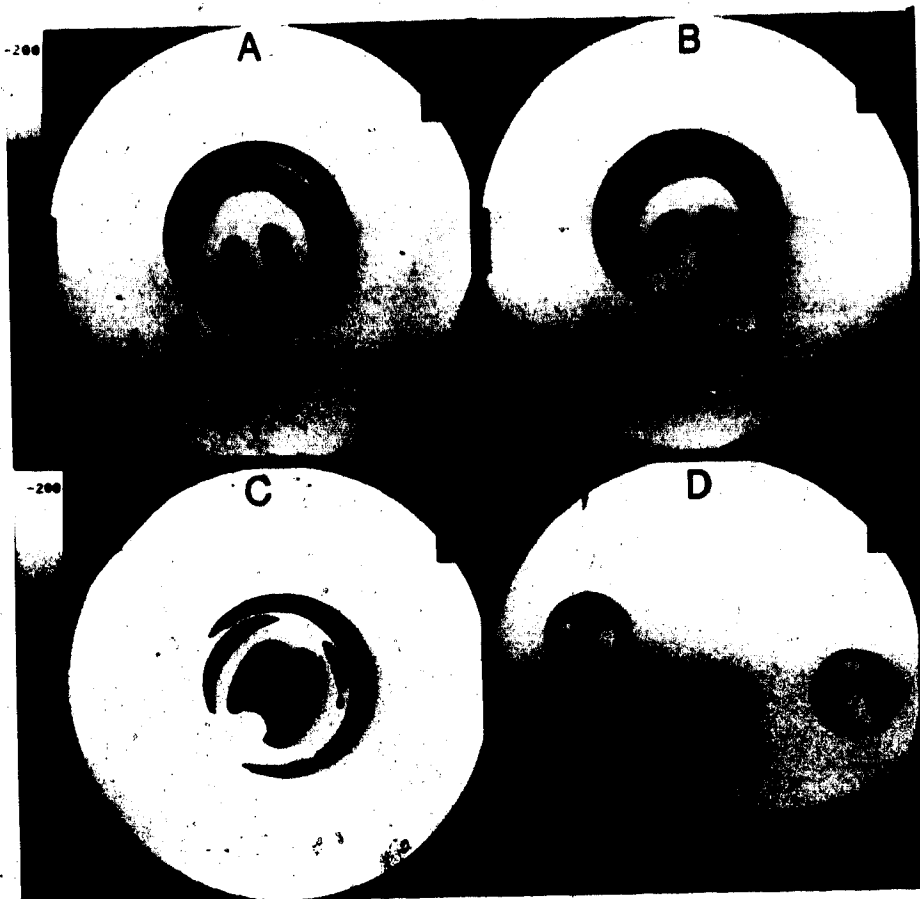
Fig. 2.12 Appearance of the CT slice at different
longitudinal positions through mouse lung
(A) near the apex, (B) and (C) mid-lung,
(D) near the diaphragm.

the mid-lung slices, the location of which was judged in terms of largest cross-sectional area of lung in the CT image. The mice were scanned with the CT scanner described in section 2.1.4. Starting at 6 weeks after irradiation the mice were scanned once every two weeks until 14 weeks, after which they were scanned once per week. For mouse lung, the viewing "level" was set at a value of -250 Hounsfields and the "window" at 100 Hounsfields to facilitate tracing of the lung outline (60). Under these conditions, the lungs appeared black and the surrounding tissue appeared white. An area of interest was traced as close as possible to the boundary of the lung. The only possible disadvantage of this tracing technique is that radiation effects near the pleura may be excluded, and thus changes in lung density were probably underestimated.

In mid-lung the boundary between the right and left lung was not always clearly visible. However, since both lungs were irradiated and showed similar effects, the definition of the right-left boundary was not critical. Examples of an unirradiated normal, as well as an irradiated mouse lung are shown in Figure 2.13 for different window settings. Note that the density increases observed during radiation pneumonitis are localized as dense patches.

The radiation dose received during one scanning procedure was 0.039 ± 0.001 Gy (112). Over the whole
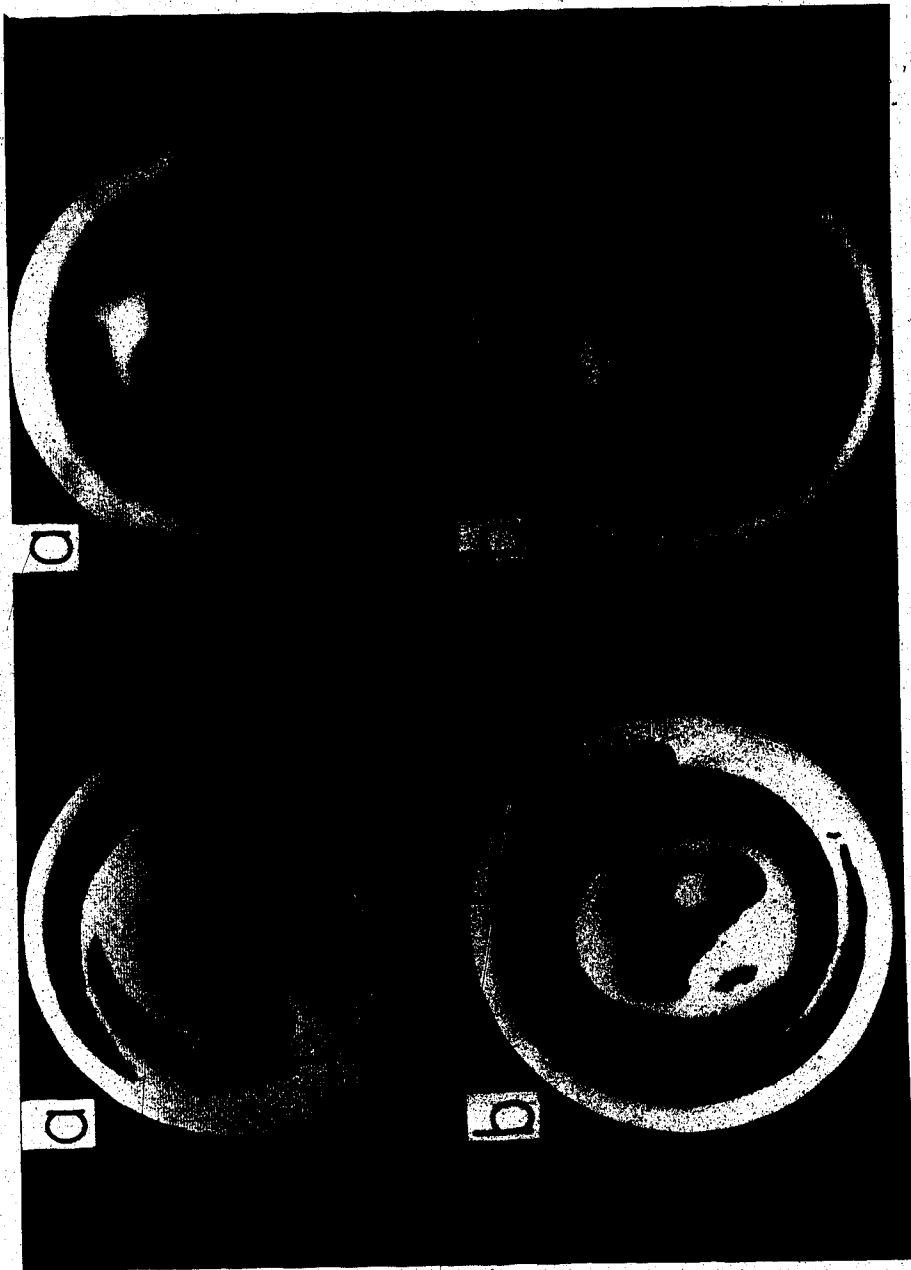
Fig. 2.13 CT slice at window settings of 100 H on the left, 1000 H on the right of (a) a normal mouse lung, (b) an abnormal mouse lung. An area of interest from which N_{CT} is calculated is traced. The level setting is fixed at -250 H.

scanning regimen of 25 weeks (16 procedures), the mice would therefore receive an additional dose of 0.62 Gy. This dose is certainly significant in magnitude but since the lungs have capacity to repair sublethal damage, a dose of 0.62 Gy in 16 fractions over 25 weeks is expected to produce no additional effect (132). However, the mice used in our studies did exhibit much less tolerance to the radiation than was expected. The LD(50/160) and LD(50/180) for lung irradiation in different strains of mice have been reported to lie between 13.5 to 16.1 Gy (106,132). For Balb/c mice used in other experiments at our Institute (102), the LD(50/160) was determined to be 13 Gy, in agreement with the above data. These mice were irradiated (but not scanned) and kept under conditions similar to those used in the experiments reported here. It is speculated that the additional dose of 0.62 Gy and the stress of weekly handling exacerbated the lung damage or interfered with recovery.

2.2.2 Results

A total of 142 mice were used for these experiments with the dose received reported in Table 2.9.

The average CT number for an individual animal, $\overline{N}_{CT}$ was measured in the right and left lung. The average CT number for an animal group irradiated to the same dose, was also calculated and is designated $\overline{\overline{N}}_{CT}$, for right and left lungs separately.

The CT numbers for control lungs of the individual animals ($\overline{N}_{CT}$) were found to lie between -475 and -550, corresponding to a normal range of lung densities of 0.45 to 0.52 g/cm^3. A plot of N_{CT} for individual animals is shown in Figure 2.14. The average CT number for this control group ($\overline{\overline{N}}_{CT}$) was -525 with a standard deviation of 30 Hounsfields for the group. No significant deviation from these values was found at any time for mice irradiated to doses of 5 and 7 Gy. A plot of the CT number for all control animals ($\overline{\overline{N}}_{CT}$), as well as those irradiated to 7 Gy are shown in Figure 2.15. For the control groups and the groups irradiated to 5 and 7 Gy, the standard deviation from the mean was maintained at 30 Hounsfields. This demonstrates that the CT numbers for

Table 2.9: Number of mice irradiated at 12 weeks of age
to the various radiation doses

Dose (Gy)	No. of Animals	Surviving at 25 weeks
0	23	23
5	18	18
7	28	28
10	28	5
12	15	0
13	15	0
14	15	1
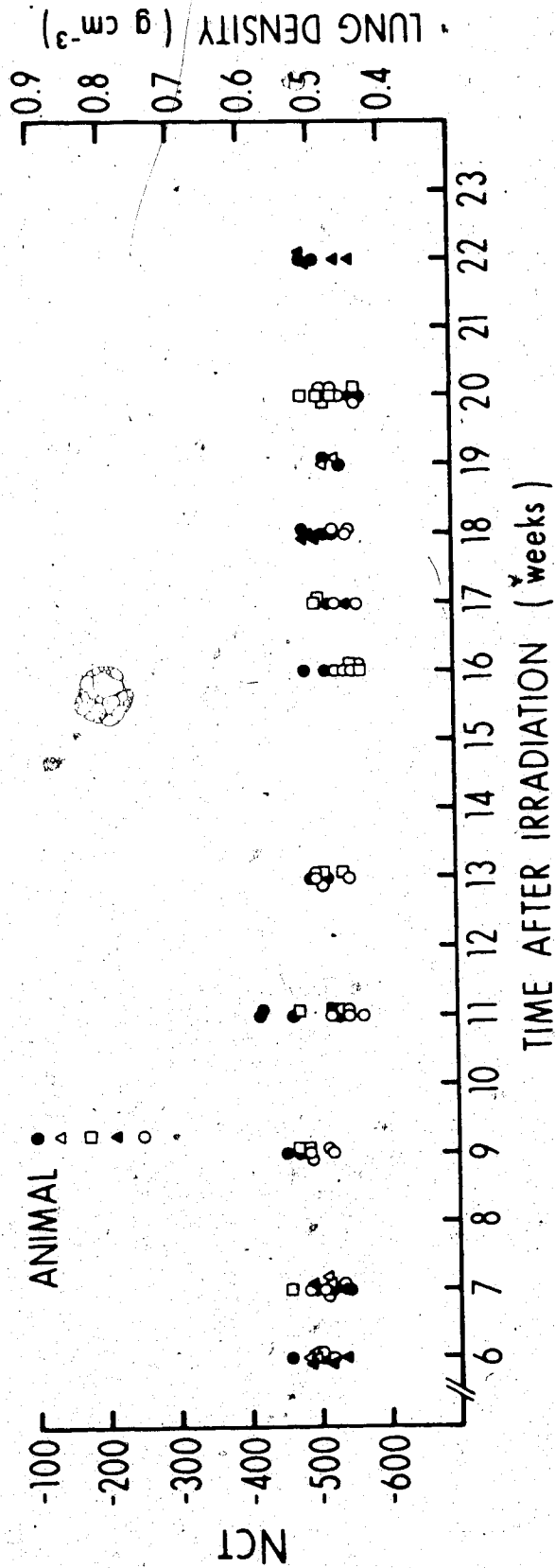
Fig. 2.14 The lung density of individual control mice. N_{CT} is the average
CT number for each slice through mid-lung.

53
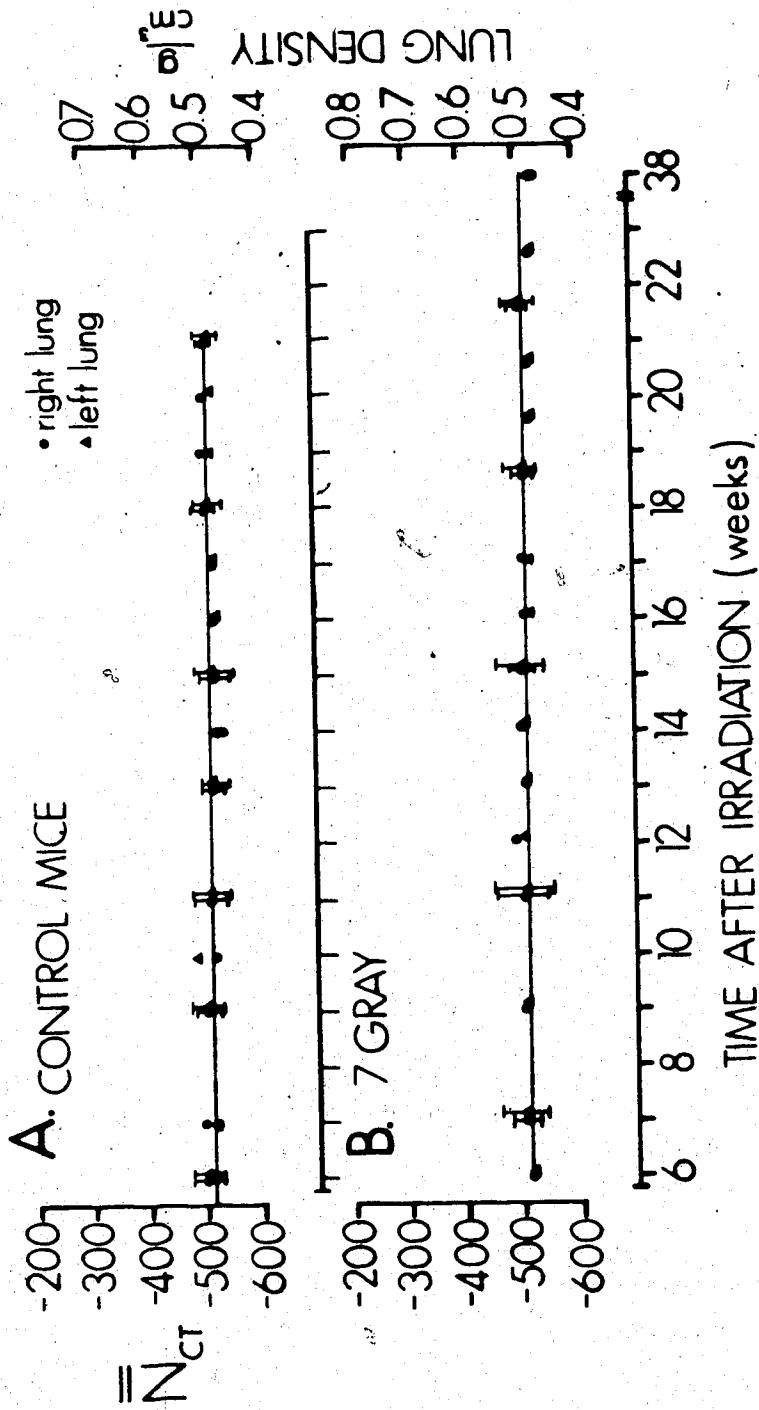
Fig. 2.15 (A) Average CT number ($\overline{\overline{N}}_{CT}$) for the control group of mice as a function of time after irradiation, (B,) Average CT number ($\overline{\overline{N}}_{CT}$) for the group of mice irradiated to 7 Gy. Corresponding densities are shown on the right ordinate. Typical error bars representing the standard deviation from the group mean are shown. The right lung and left lung data are plotted separately.

animal lungs were reproducible to within 6% (i.e. 30/500). This variation is attributed mainly to biological differences within the animal groups since the reproducibility of the CT scanner data alone is 0.6% for lung-substitute materials, as noted in section 2.1.6.

2.2.2.1 Acute Phase

Mice receiving doses of more than 10 Gy showed a gradual increase in density beginning at 15 weeks following irradiation, with large variations in individual animals, as shown in Figure 2.16.

The time course of density changes for mice receiving 13 and 14 Gy are also shown. These curves are similar, with more severe changes observed for increasing doses (see Figures 2.19, 2.20). The appearance of the scans as the mice go through the pneumonitis phase is shown in Figure 2.17 for 3 individual mice. At 7 weeks no effect is visible or measured as a density increase. At 16 weeks no effect is visible but a significant CT number increase is noted. At 18 weeks CT number changes are both measured and clearly visible. For the mouse irradiated to 7 Gy no change is visible or measurable at any time. The large individual variation is illustrated in Figure 2.18 where N_{CT} is plotted for 5 individual animals irradiated to 10 Gy.

Student's t-test was performed to test the statistical significance of the density increase at 1
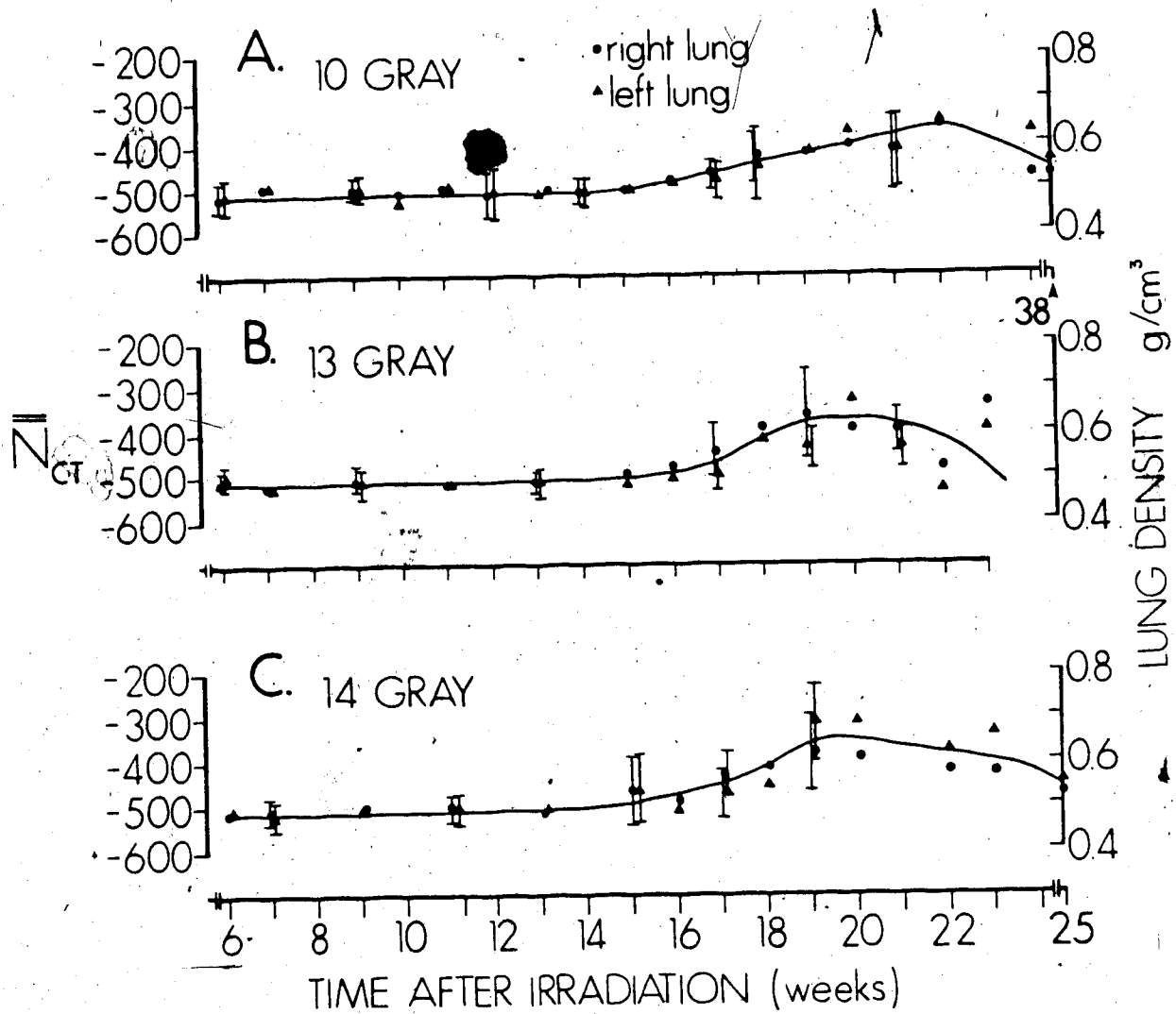
Fig. 2.16 Average CT number ($\overline{\overline{N}}_{CT}$) for: (A) group of mice irradiated to 10 Gy, (B) group of mice irradiated to 13 Gy, (C) group of mice irradiated to 14 Gy. Corresponding densities are shown on the right ordinate. Typical error bars represent the standard deviation from the mean of the group. Error bars increase during the pneumonitis phase (16-22 weeks) because of greater variations in response of individual surviving animals.
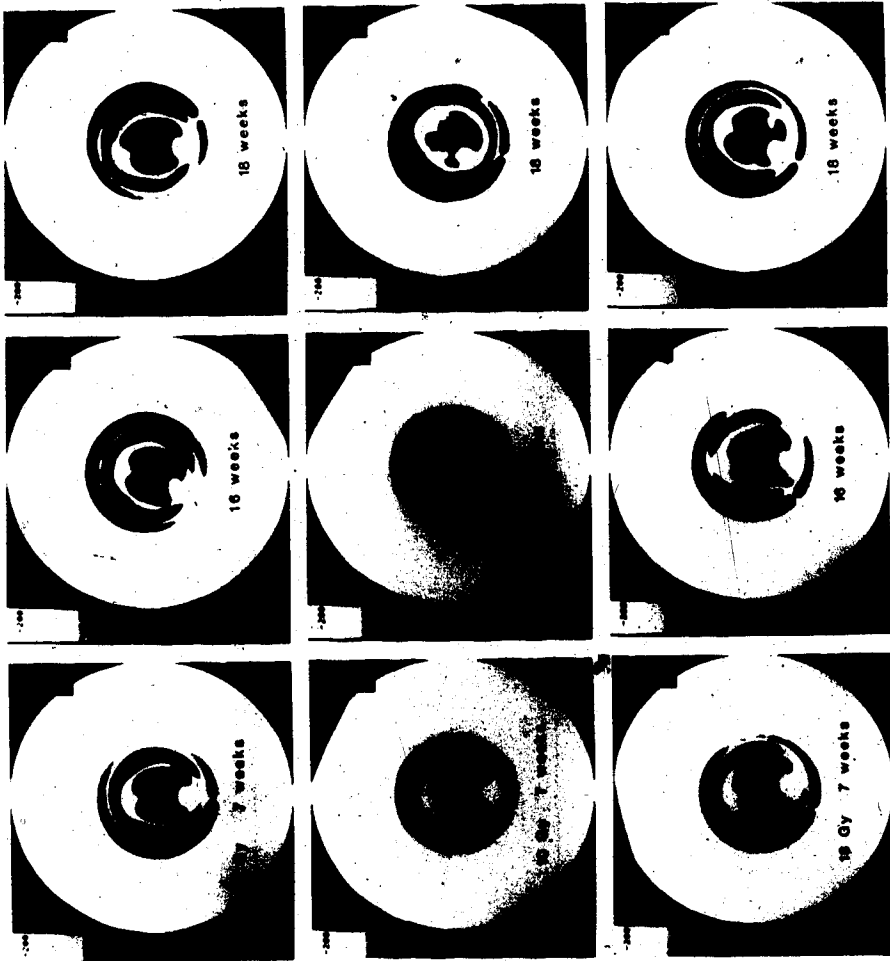
Fig. 2.17 CT scans of mouse lungs showing radiation-induced changes at 7 weeks, 16 weeks, 18 weeks.

57
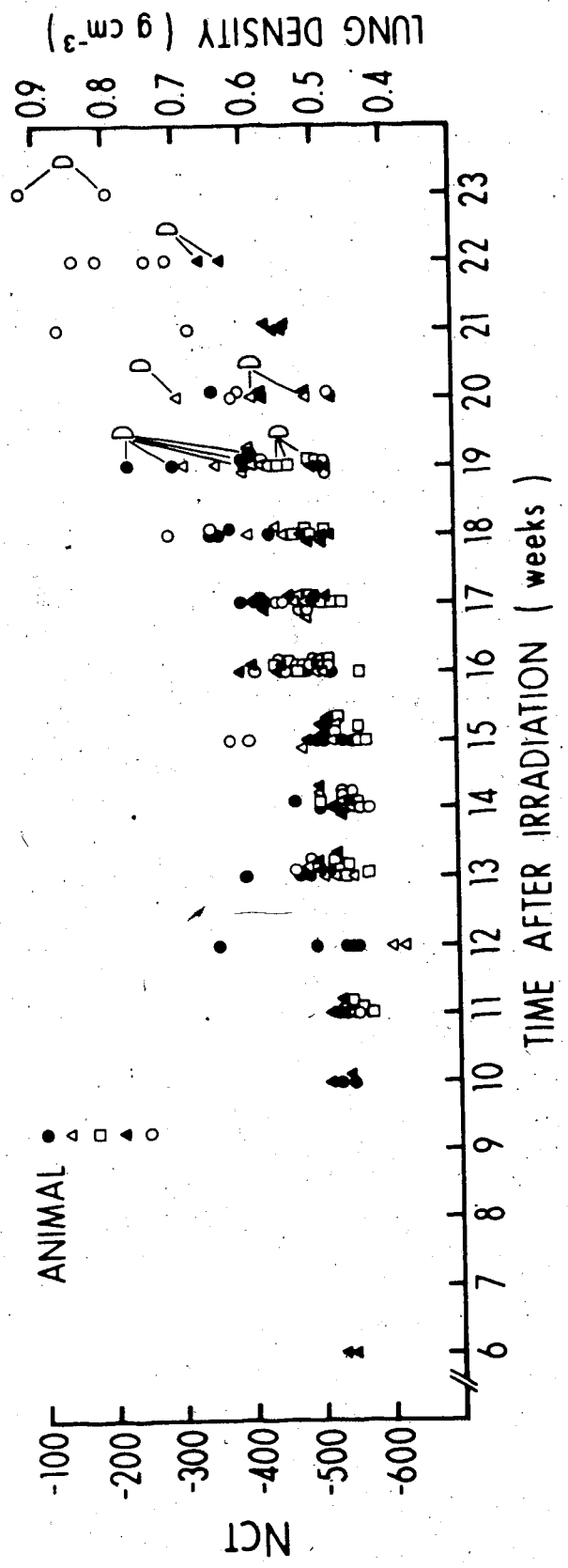
Fig. 2.18 The lung density for individual mice irradiated to 10 Gy.

N_{CT} is the average CT number for each slice through mid-lung.

weeks after irradiation to 10 Gy. The level of significance was found to be larger than 99.99%. The changes observed at later times and at the larger doses were as significant.

Deaths occurred between 19 and 24 weeks. Mice whose lung density in both lungs increased by more than 40% from a normal value of 0.5 g/cm^3 to $\geq$ 0.7 g/cm^3, would generally die within the ensuing 2 weeks of such change. The above data are summarized in a different manner in Figures 2.19 and 2.20. In Figure 2.19, the time course of the changes in density is shown. The percent incidence of animals with a threshold increase of greater than 40% in lung density is plotted as a function of time. Figure 2.19 shows that major changes occur in the time period of 16 to 21 weeks with more severe effects occuring slightly earlier at the higher doses, in good agreement with the data of Travis et al. (116,118).

Figure 2.20 presents the same data plotted instead as a function of radiation dose for the "acute" phase of 15 to 21 weeks. This plot suggests that the severity of the effect increases with time as well as with dose, again in agreement with the findings of Travis et al. (116,118). However, the 40% increase in density chosen is an arbitrary threshold. Thus, Figures 2.19 and 2.20 might be different if other threshold values are chosen.

Two of the mice were autopsied and the histopathological findings in lung corresponded to the
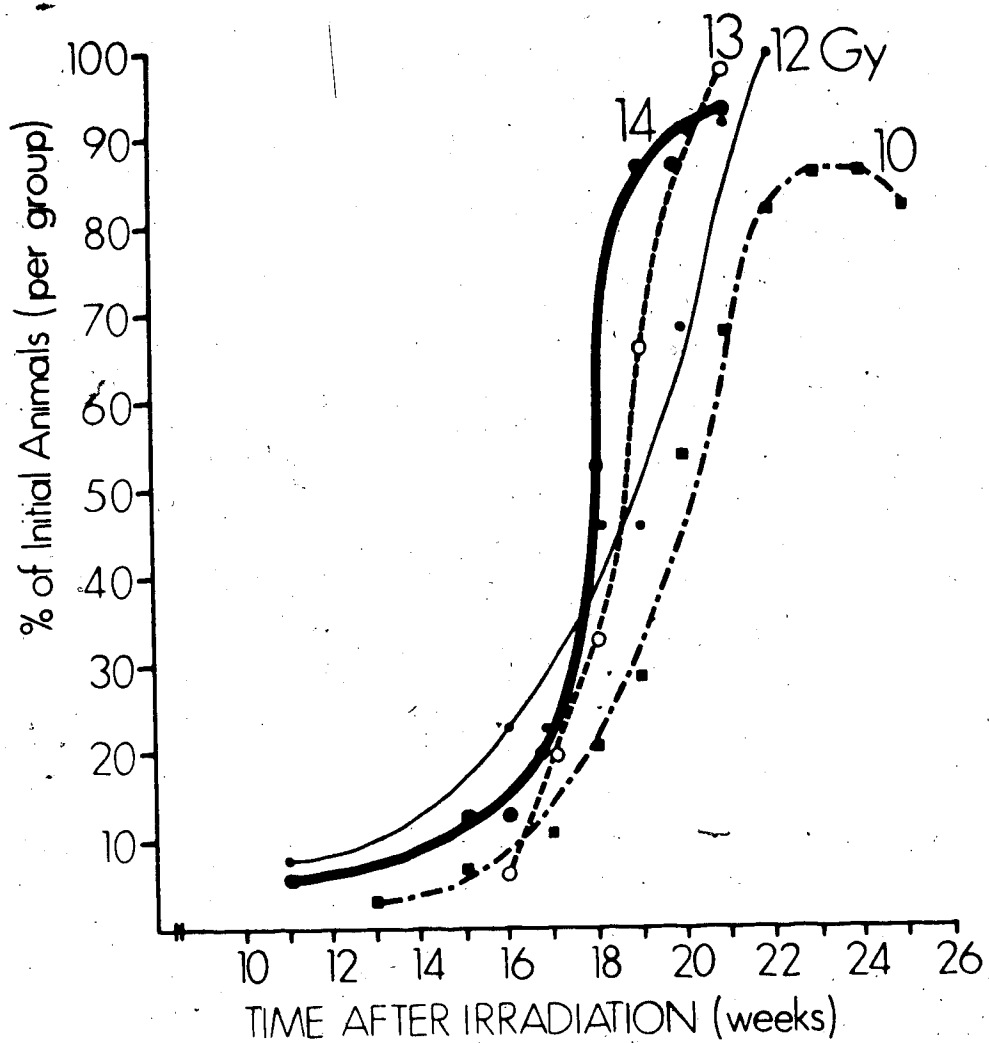
Fig. 2.19 The percent of animals whose lung density increased by more than 40% is plotted as a function of time after irradiation for the groups of mice irradiated to 10, 12, 13, and 14 Gy. The incidence is defined with reference to the initial number of animals (100%) in each dose group.
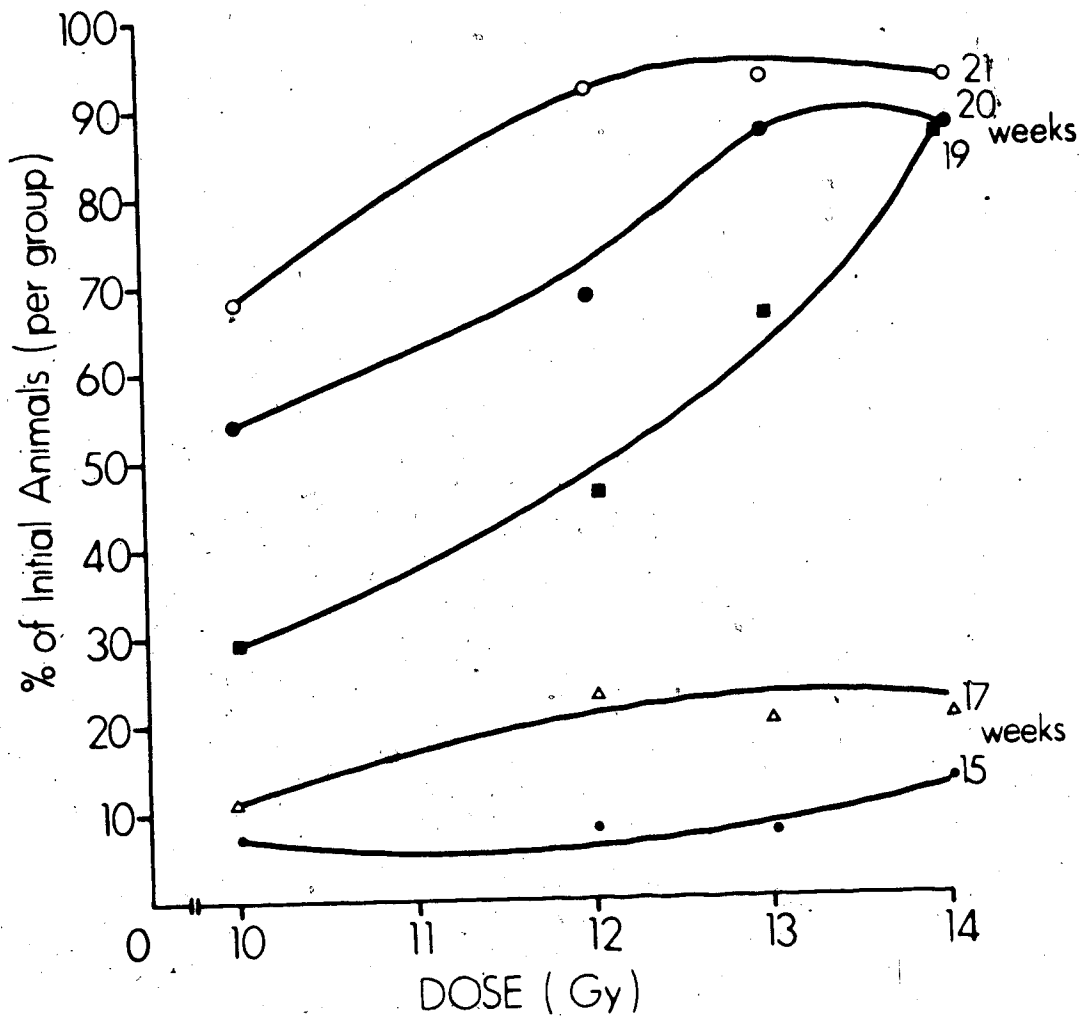
Fig. 2.20 The percent of animals whose lung density increased by more than 40% is plotted as a function of dose during the acute (radiation pneumonitis) phase 15-21 weeks. The number of animals with severe effects increases with dose.

classical description of radiation pneumonitis.

Histopathology report as obtained from Dr. L.D. Armstrong, Animal Disease Section, Laboratory Services, University of Alberta.

"Mouse No.1 - The lung tissue examined was much more cellular than normal with large numbers of alveolar macrophages present in the alveoli. These macrophages were swollen and vacuolated with some golden brown staining pigment. Interstitial areas or alveolar walls themselves were thickened due to cellular infiltration which was primarily macrophage and mononuclear in nature. Some interstitial areas showed evidence of fibrin accumulation and this is what was judged to be in some of the macrophages, giving them a ground glass appearance. Occasional double nucleated macrophages were encountered. Very slight mononuclear accumulations were noted adjacent to some of the airways. Airway epithelium itself was moderately uniform with moderate anisocytosis of nuclei and with some jumbling up of cells into multiple layers. The lumenal border of these epithelium cells was jagged with individual cells protruding and having rounded borders (Clara cells). A few macrophages were evident in the lumeni of airways.

Mouse No.2 - Was similar although more pronounced in these changes, large numbers of macrophages ranging in sizes from normal to gigantic were found within the alveoli. These macrophages contained dark golden brown pigment or were very large and pale staining with apparent protenaceous edema fluid. Some edema was found in this particular lung along with more focal distribution of hypercellularity to the alveolar walls with the predominant cell type being macrophages and mononuclears. Similar changes were found in the epithelium of the airways, being slightly hyperplastic, uniform in outline and numerous epithelioid or macrophage type cells in the lumen. Mononuclear accumulations were more prominent adjacent to airways in this mouse."

The lungs of several mice were also examined post mortem by microscope. The lungs were severely edematous with few functional alveoli. The appearance was dark red, and no pus, normally indicative of infection, was observed. Thus

the changes are entirely attributed to radiation effects.

Only one animal irradiated to 14 Gy survived the early acute phase but died at 30 weeks. Data for this anecdotal case are shown in Figure 2.21. The CT numbers for the right and left lung are plotted separately. The density increases during the acute phase were confined to the apex and diaphragm CT slices for this mouse. There was no density increase in the three mid-lung slices. Therefore the volume of lung affected by radiation pneumonitis was much smaller for this mouse, which explains its longer survival. However, the density increased progressively in mid-lung with the left lung showing more pronounced effects. At the same time the appearance of the lung took on a different shape as is shown in Figure 2.22, with the pleural boundary being very irregular. This case suggests re-organization of lung structure to cope with damage. However, despite this remodelling, the mouse died during the late acute phase.

2.2.2.2 Intermediate Phase

At 30 weeks after irradiation, there were no survivors among mice irradiated to doses of 12, 13, and 14 Gy. However, at a sublethal dose of 10 Gy, 5 of 28 (18%) animals survived the acute phase. Between 22 and 39 weeks after irradiation, the average CT number for this group ($\overline{\overline{N}}_{CT}$) resolved to near-normal values, lying between -420 to -460 Hounsfields, (i.e. densities in the range of 0.54
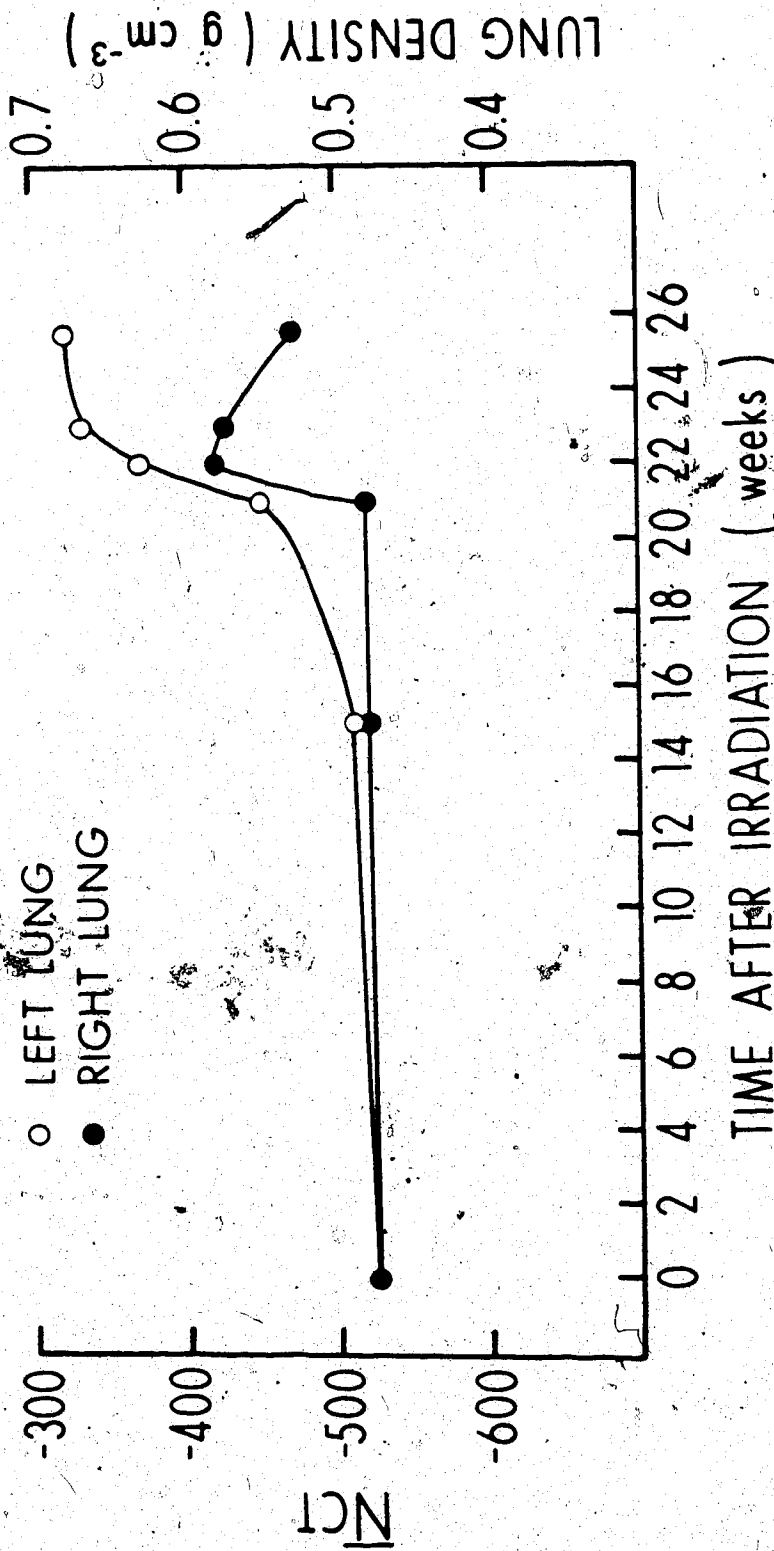
Fig. 2.21 The average CT number ($\bar{N}_{CT}$) for an individual mouse irradiated to 14 Gy.
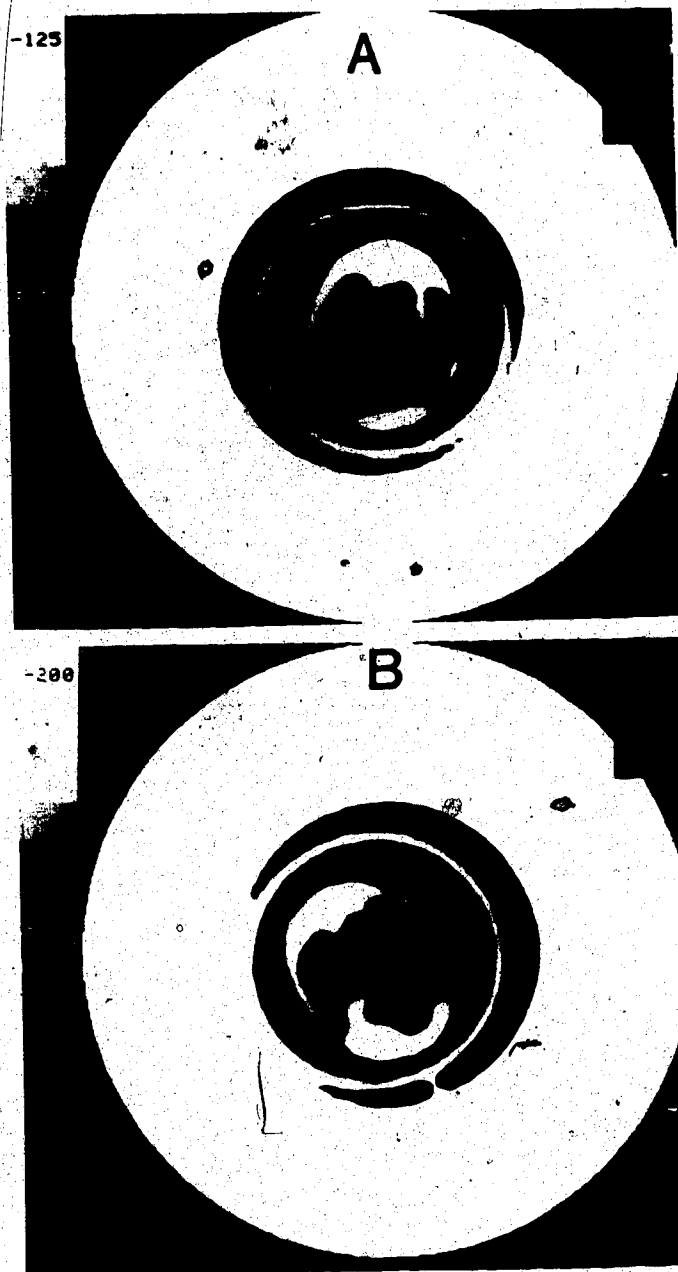
Fig. 2.22 CT scan of a mouse lung irradiated to 14 Gy

(A) 23 weeks after irradiation,

(B) 25.5 weeks after irradiation.

The altered shape of the lung is apparent,

particularly in the pleural region.

to 0.58 g/cm^3). However, with so few animals surviving the acute phase, data on the intermediate and late phases are very limited.

2.2.2.3 Late Phase

Two mice irradiated to 10 Gy survived at 52 weeks after irradiation, at which time a final scan was performed. The following values were obtained:

Animal	R-lung		L-lung	
	$\overline{N}_{CT}$	ρ (g/cm^3)	$\overline{N}_{CT}$	ρ (g/cm^3)
1	-492.09	0.508	-373.27	0.627
2	-486.52	0.513	-342.78	0.657

In comparison to control density values at this time,

	-520.95	0.479	-517.48	0.483

Thus the density is elevated with an appearance as shown in Figure 2.23. One of the mice showed slight structural changes, again indicating lung remodelling. For both mice the left lung was more affected than the right. The reasons for this right-left asymmetry are not clear, although it is known that structurally each side is different in the number and size of component lobes. These mice were subsequently sacrificed and preserved for analysis by immonufluorescence to quantify collagen deposition during late fibrosis (76).
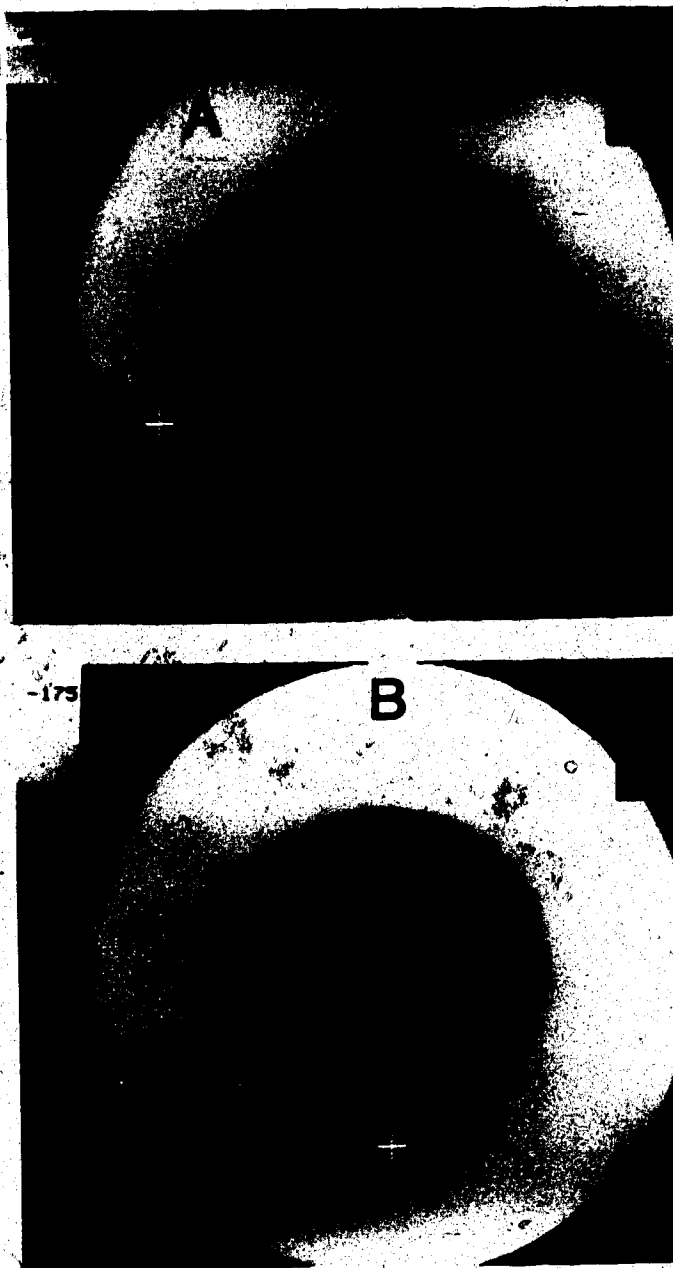
Fig. 2.23 CT scans of two mice irradiated to 10 Gy
52 weeks after irradiation (A) mouse 1,
(B) mouse 2. Structural changes are
apparent only in (A).

2.2.3 Comparison with Mass Measurements

2.2.3.1 Radiation-Induced Changes

No increases in density were found at 6 weeks after irradiation, the time at which an increase in lung mass had been reported (102). Assuming a constant lung volume, an increase in mass was expected to produce a corresponding increase in density. However, a comparison of mass increases with CT density increases for 9 mice irradiated to 11.5 Gy at 17.5 weeks after irradiation indicated a very poor correlation. This disparity is probably due to differences in vo͟͟͟͟͟ density of excised lung in com͟͟͟ with in-vivo lung.

2.2.3.2 Adrenaline-Induced Changes

A further comparison was made by inducing changes in lung density in a more controlled way, without using radiation. An injection of adrenaline produces edema in the lungs within minutes, the͟͟ increasing lung density (94). Mice which were injected, sacrificed and had their lungs weighed showed a͟ increase in lung mass relative to control mice, and this effect lasted about 15 minutes. After this time, the edema began to clear slowly. In order to obtain different mass increases, various concentrations of adrenaline were injected until the desired range of lung mass increases was achieved. The concentration of adrenaline, (Epinephrine Hydrochloride Solution, Parke-Davis 1mg/1ml) was varied between 0.07

mg/ml and 0.2 mg/ml. Thirty-six animals were used in this experiment. The dose, normalized to the animal body mass, varied between 0.69 mg/g to 1.58 mg/g. The animals were scanned before injection to obtain control density values. Then the animals received the adrenaline injection into the thigh muscle, and were scanned immediately afterwards. Two to three CT slices through lung were obtained and CT data were calculated in the usual manner. The animals were subsequently taken from the phantom and sacrificed immediately so that the total time from time of injection to time of death was less than 20 minutes, i.e. within the time that the adrenaline effect lasts. The excised lungs were weighed, and the mass increase determined according to the assay developed by Sharplin and Franko (102). This mass increase was then compared to the in-vivo increase in CT density for individual animals. The increase in CT density is relative to the mean for the controls (0.475 g/cm^3) and the increase in mass is relative to a baseline lung mass calculated for a "standard mouse" weighing 21 gm (99). Comparing the percent increase in post-mortem mass to the percent increase in in-vivo CT density and analysing the data using linear regression, a correlation coefficient of 0.7 was determined. Assuming a constant lung volume, a straight line with an intercept of 0.0 and a slope of 1.0 was expected, but not observed. A 25% increase in mass only increased the density by 6%, which can only be

detected with modest (67%) confidence by CT. The measurement of mass, although invasive, is a more sensitive indicator of lung damage since the entire lung is sampled. The CT tracing procedure avoids the pleural boundary of the lung, thereby excluding possible pleural changes. The density increase which often occurs as localized patches (see Figure 2.17) is thus underestimated. Also it is speculated that the volume of lung changes with the adrenaline (and possibly with irradiation), and that a comparison of changes in <u>mass</u> to changes in <u>density</u> is not possible without simultaneous measurement of volume. Furthermore, there are reasons to expect that such changes will certainly be different in excised as opposed to in-vivo lungs.

2.2.3.3 Volume Measurements

In inanimate objects of regular shape, it is possibile to obtain accurate measurements of volume by CT scanning a series of contiguous slices (see section 2.1.6 and (10)). In the live mouse, this is much more difficult due to voluntary and respiratory movement of the mouse, and the variable shape of the lung from slice to slice. It is equally difficult to obtain reliable volume measurements <u>ex-situ</u> due to problems with excision - possible leakage of blood or air, and the difficulty measuring the small volume using Archimedean methodology. Nonetheless an attempt was made correlate density and

volume measurements by CT with mass and volume measurements ex-situ. Measurements were obtained on 16 mice irradiated to 8 Gy at 6.5 weeks after irradiation. The data are plotted in Figure 2.24. The method of obtaining lung volume ex-situ was as follows. The excised lungs were tied at the bronchi to avoid the escape of air and were immersed in a vial with saline. This vial was weighed, lungs were removed, the vial was refilled with saline again and weighed. The difference between these two values gave the air volume according to Archimedes' principle. The lungs were then removed, bronchi cut away, and weighed. This weight divided by 1.05 (tissue density) gave the tissue volume. The ex-situ lung volume then was the sum of tissue volume and air volume. If both methods measure volume and density accurately the values would lie on the equal volume and density lines. However, volumes as measured by CT were lower and CT measurements consistently gave higher values for density.

In order to improve accuracy, larger animals such as rats (Sprague-Dawley) were used for mass, volume, and density measurements by CT scan and ex-situ measurements. The rat lung (2-12ml) is more than ten times greater in volume than mouse lung (0.4 ml) as seen in Figure 2.25. Agreement of in-vivo and ex-situ measurement of lung, was better for rats than for mice, but CT density and volume values were still generally higher. These differences are too large and variable to be explained by systematic

71
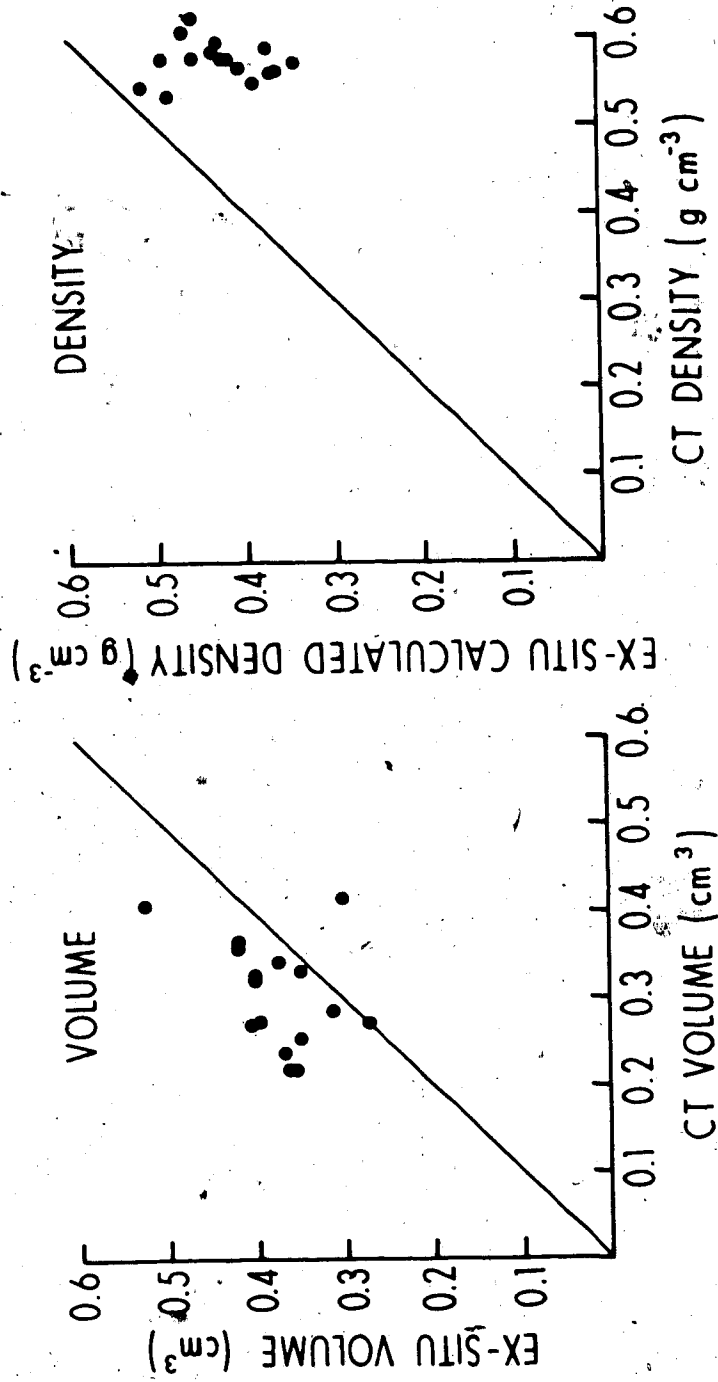
Fig. 2.24 Comparison of in-vivo (CT) density and volume measurements to ex-situ mass and volume measurements for irradiated mouse lung.

72
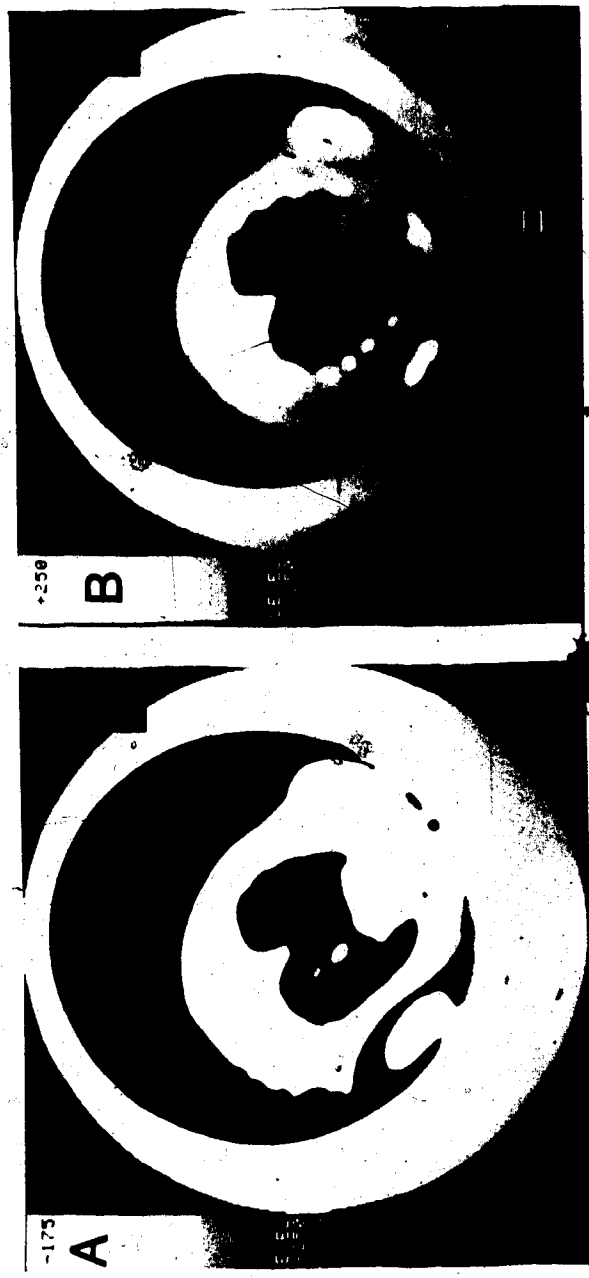
Fig. 2.25 CT scan of a rat lung (A) with a level setting of -250 H and a window setting of 150 H, (B) at the same level setting but with a larger window setting of 1000 H.

differences in data acquisition or analysis by both methods. Lung volume and density are highly dependent on air content (ventilation) and blood content (perfusion) in the lung which in turn is related to blood pressure. These are much different in the live breathing animal than in the excised lung (42); this is the most likely explanation for discrepancies observed between the in-vivo CT and the ex-situ measurements. Since the air content was controlled in our experiments by sealing off the trachea, differences in lung perfusion were further investigated.

In order to test whether a change in blood pressure affects lung density, the following experiment was performed. Eight mice were anesthetized with an intraperitoneal injection of Tribromoethanol. They also received an injection of 0.2 ml of an anticoagulant (Heparin Sodium, Hepalean) into the thigh muscle. They were then scanned in the usual manner. When mid-lung slices were reached, the animals were bled from the jugular vein and re-scanned immmediately. Mice bled by various amounts, but all were still alive at the end of the experiment. Three control mice were also scanned; these mice received the same injections of anesthetic and anticoagulant as the experimental animals, but were not bled. These mice had slightly higher average lung densities (0.512 g/cm³) than the control value established in earlier work (0.475 g/cm³).

A definite decrease in lung density from baseline was produced when blood pressure was reduced by bleeding the animal. These amounts varied from a 9% decrease to a 67% decrease depending on blood loss. This effect has already been reported in dogs (41). Therefore, the loss of blood and resultant decrease in blood pressure in lung produce when the lung is excised from the body, explains the lower density measured for the excised lung as compared to in-vivo CT densities. At present, The CT measurement gives the most accurate value for in-vivo lung density. Any method measuring density and volume in excised lung is therefore subject to a systematic error because of blood loss during excision. This conclusion, however, does not invalidate any experiments performed measuring post-mortem changes because relative (%) changes are usually measured. Such changes are independent of the absolute value of the parameter being measured.

An attempt was made to correlate the blood loss and the decrease in CT density. Mice were anesthetized and bled from a vein near the eye, where the blood could be taken up in a syringe and weighed. This first attempt failed as the anesthetized mice showed patchy density increases throughout the lung, and it was not possible to measure an accurate decrease in density. This was in contrast to the previous experiment, where mice had received a heparin injection in addition to the anesthetic and a slight homogeneous density increase had been

observed.

2.2.4 Conclusions

This part of the study has indicated that an increase in density of mouse lung caused by irradiation can be detected easily by CT scanning. The time course of the density changes, the time of peak response, and the dose dependence correspond well with the histological findings (116). Therefore the CT scan is a good indicator of the changes occuring during the acute response of the lung to irradiation. Indeed a change of more than 40% in lung density is predictive of mortality. Moreover, CT data were obtained weekly from the same animals, so that they served as their own controls during progression of the effects. This non-invasive technique has an advantage over other approaches in which data are obtained from different animals by excising the lung post-mortem. As well CT densitometry gives the most accurate value for in-vivo lung density. This non-invasive method could be applied to monitor lung tissue damage in patients who have received radiotherapy. In fact it has already been demonstrated to be advantageous over conventional radiography in this regard (79,89). In our Institute we have designed such a clinical study for patients, receiving upper half-body radiotherapy. Results are presented in section 2.4.

2.3 Experiments with Dogs

2.3.1 Introduction

The studies with mice reported in the previous section proved useful in establishing the validity of CT densitometry as a method of assaying lung damage in-vivo. However, several difficulties were encountered due to the small size of the mouse lungs, including the definition of the actual lung volume. To overcome these problems, experiments with a larger animal was desirable in order to: (a) sample a larger volume of lung, (b) study changes near the pleural boundary of lung and (c) compare to other in-vivo diagnostic tests, such as standard X-radiography and nuclear scintigraphy. For the intercomparison studies, the animal was sacrificed as soon as the dog was in the pneumonitis phase and all tests became abnormal. Histology and electron microscopy were also used to analyse the lung sections in order to correlate the extent and severity of lung damage with the diagnostic findings. The only limitation to the dog study was the restriction in the number of animals that could be managed. Thus the time course of pneumonitis was studied in individual rather than groups of dogs.

2.3.2 Irradiation

Ten dogs were irradiated with a single dose of 20 Gy to the mid-lung in the inferior zone of the right lung

only. Two dogs were irradiated to a lower dose of 10 Gy. The Cobalt-60 irradiation was delivered with a parallel-opposed pair of 5x7cm^2 fields to achieve a uniformity of approximately 10% in lung dose. The dose was chosen high enough so as to produce a significant likelihood of damage in a restricted volume of lung, but irradiation of heart or mediastinum as well as esophagus was minimized. This is significantly different from the irradiation protocol used for the mouse work.

2.3.3 Diagnostic Tests

The animals were mongrel dogs of both sexes with an average body weight of 21 kg. During all procedures the dogs were anesthetized with pentobarbital (30 mg/kg) lying supine and breathing spontaneously. Besides CT scanning, conventional X-radiographs of the dog lungs were also obtained. In addition, clearance of radioactive sodium pertechnetate (TcO_4^-) aerosol from lung, and lung perfusion using 99mTc-labelled macroaggregated albumin (MAA) scanning were monitored using standard nuclear medicine instrumentation. Details of these nuclear medicine studies are reported in a separate thesis submitted by I. Ahmed (Department of Medicine).

The dogs were CT scanned every two weeks starting at 3 weeks post-irradiation. Pre-irradiation scans were obtained and served as controls. A digital radiograph (or "scout scan") of the thorax was first performed for

positional referencing with respect to the area of irradiation. Approximately 10-12 slices, each 1cm thick and spaced 1.5cm apart were acquired in order to cover the complete dog lung from apex to diaphragm. In each slice the complete lung area was outlined for left and right lung, and the average density calculated therein. The best correlation between traced area and true area for dog lung was obtained at a level setting of -370 Hounsfields. A window setting of 100 Hounsfields was used, although this setting is not as critical. The area of interest was traced as close as possible to the pleura of the lung. An example of an irradiated and unirradiated dog lung and the tracings are shown in Figure 2.26.

In the dog there is an intrinsic density gradient from apex to diaphragm as well as from anterior to posterior presumably due to blood pooling caused by gravity. This gradient is apparent in Figure 2.27 where N_{CT} is plotted as a function of distance from apex to diaphragm, relative to the sternal notch at 0 cm. A slice near the apex and one near the diaphragm is shown in Figure 2.28, to demonstrate the density gradient in a pictorial manner. The denser areas are more vascular.

The right and left lungs do not have the same shape and longitudinal position in the thoracic cage. Therefore the left lung slices at the same longitudinal position could not be used as controls in these experiments even though they were unirradiated. In the inferior zone,

Fig. 2.26 CT slice of (A) a normal dog lung, (B) a dog
lung after irradiation. An area of interest
from which N_{CT} is calculated is traced.
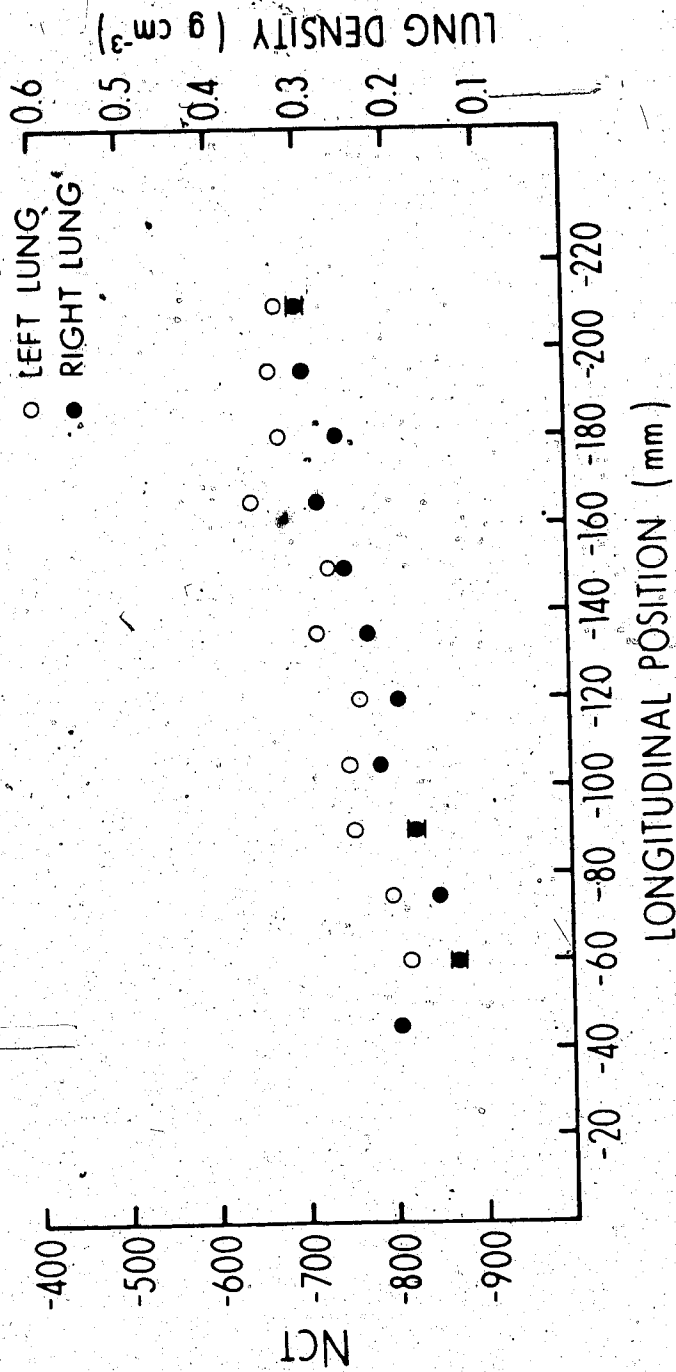
Fig. 2.27 The average CT number per slice ($\overline{N}_{CT}$) in dog lung for various longitudinal positions in the thorax.
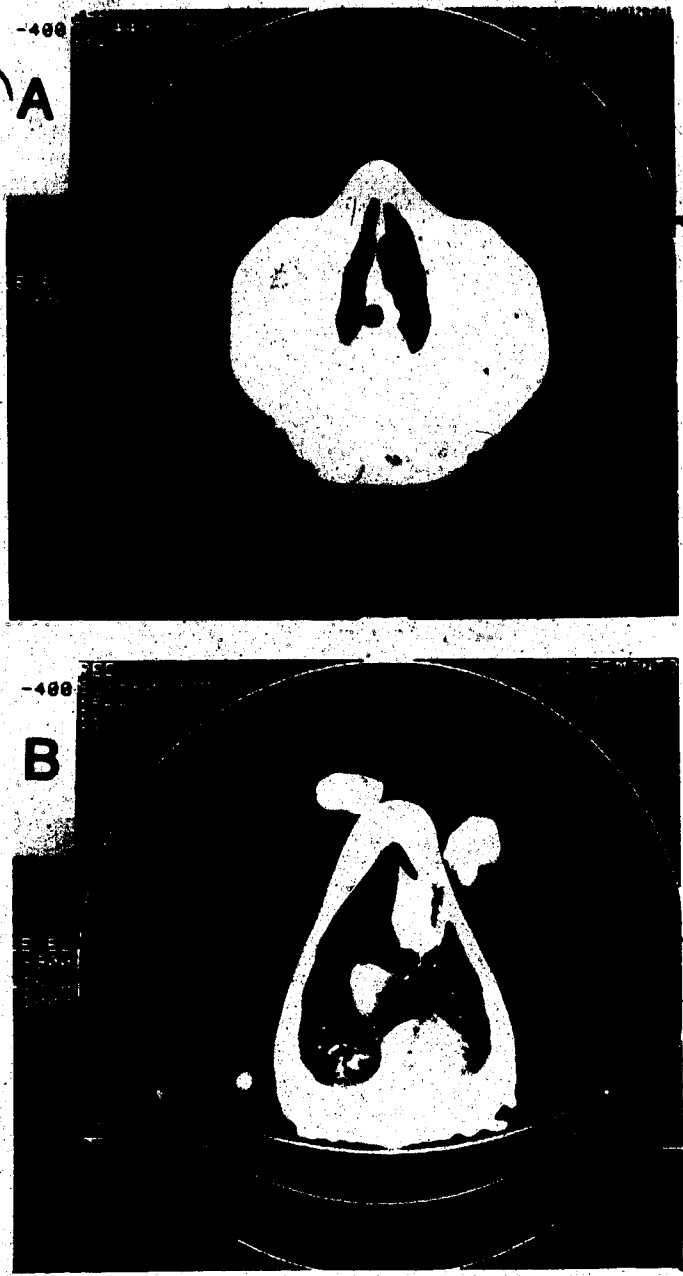
Fig. 2.28 CT slice of dog lung (A) near the apex,
(B) near the diaphragm.

there is an additional problem due to the diaphragm which interferes with the left side "lung" slices, Figure 2.28.

The radiation dose received during each scanning procedure depends upon the tech_____ed. The X-ray tube voltage was fixed at 120 _____urrent and pulse width was varied depen_____e size of the dog. Representative maximum doses measured at the dog skin are shown in Table 2:10. These doses were measured using a specialized air ionization chamber (112).

Table 2.10: Radiation dose to dog lung and technique used during the scanning procedure

	Dog 1	Dog 2
Current	160 ma	250 ma
No. of pulses/scan	576	576
Pulse width	3.3 msec	3.3 msec
scan time	307 mA-s	480 mA-s
Dose	2.17 cGy	3.69 cGy

2.3.4 Results

As noted earlier, ten dogs were irradiated to 20 Gy, while two dogs were irradiated to 10 Gy. Pre-irradiation scans were performed on the dogs to establish control values of density. Typically the inferior 4 slices of the right lung were through the irradiated zone. CT number

values were averaged for these slices only. Lung was outlined in the same manner as with the mice, and an average density for the slices was calculated. The control values were obtained for the same volume of lung, prior to irradiation. Control values were also obtained in a different way by sampling the unirradiated left lung. Thus, at each scan time, a value $\Delta N_{CT} = N_{CT}$ (left) $- N_{CT}$ (right) was determined. The data analysed using either the pre-irradiation right lung scans, or the different left lung scans as controls gave similar results. Only the results obtained using the pre-irradiated right lungs as controls are reported here.

The average CT number for the 12 dogs was -753 ± 29 which corresponds to a density of 0.25 ± 0.03 g/cm^3. This value is considerably less than that of mice, and much closer to values reported for humans (129). The CT number and density values for the individual dogs are shown in Figures 2.29 A,B and 2.30 for different times after irradiation. For the dogs irradiated to 20 Gy, one dog showed a significant increase in density as early as three weeks after irradiation (C-568). Another dog (C-694) showed a significant increase in density at 4 weeks. Two dogs died of unknown causes before tests became abnormal. Of the remaining dogs, all but one (C-566) showed significant changes by 10 weeks after irradiation. Infection was ruled out since dogs were given weekly injections of Penicillin.
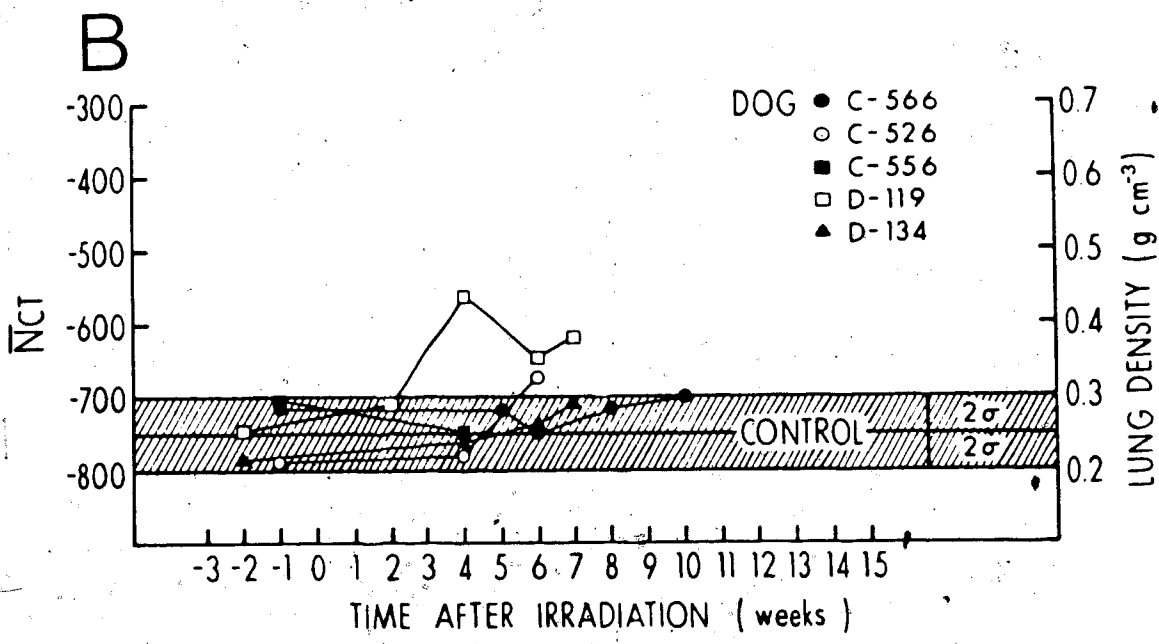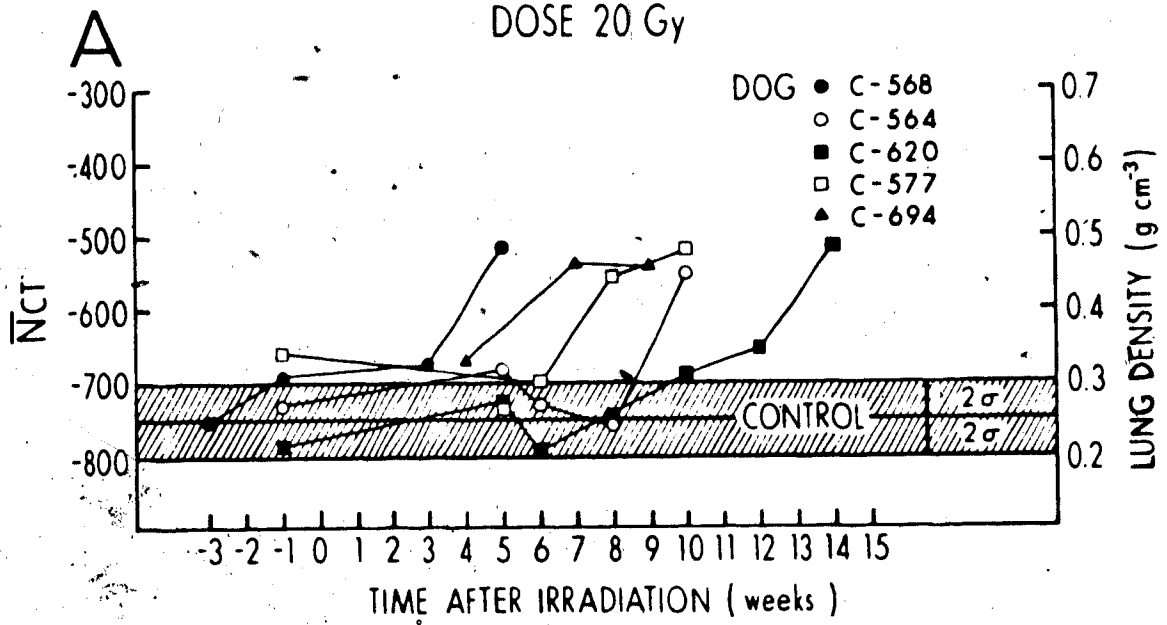
Fig. 2.29 A,B Average CT number ($\overline{N}_{CT}$) for each dog irradiated to 20 Gy.
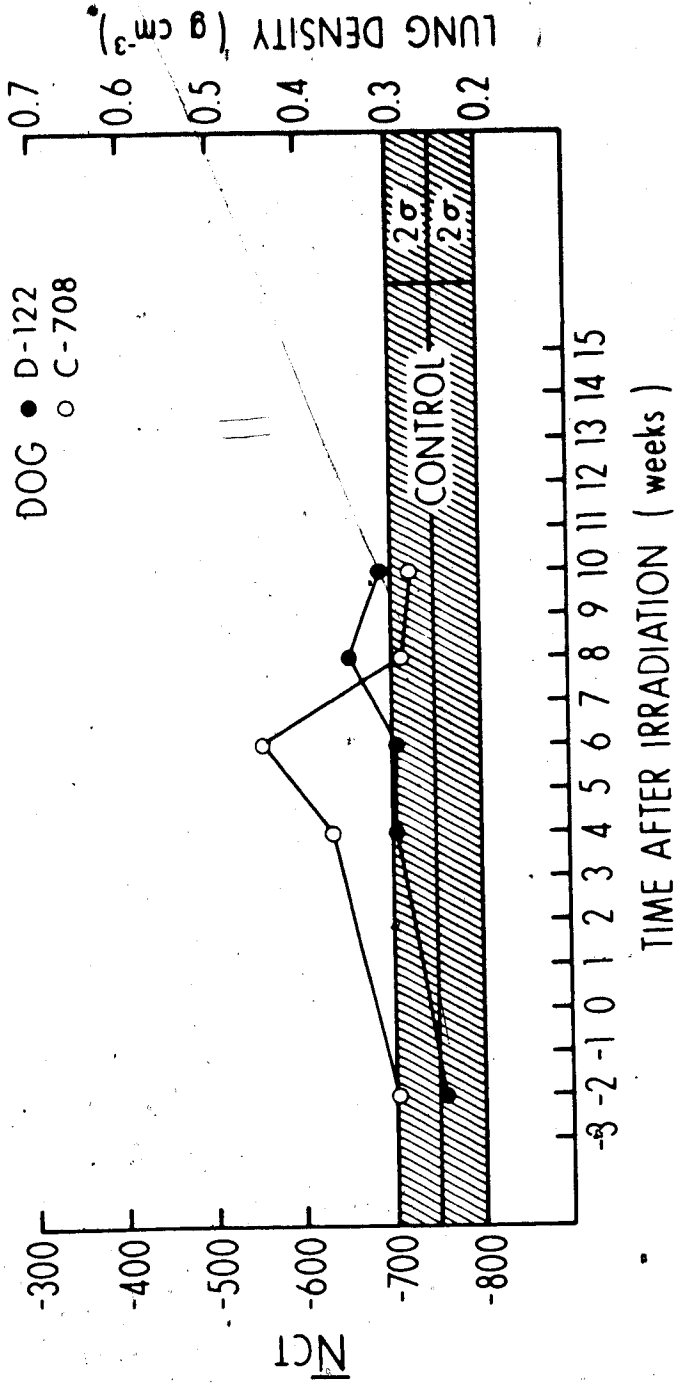
Fig. 2.30 Average CT number ($\bar{N}_{CT}$) for each dog irradiated to 10 Gy.

Of the dogs irradiated to the lower dose (10. Gy) one showed a significant density increase at 4 weeks after irradiation, which increased further at 6 weeks but returned towards normal at 8 weeks. After this time this dog showed normal results on all tests, and it seemed that the early effect had resolved. This supports the concept of lung repair. The other dog became abnormal at 8 weeks. Both dogs were sacrificed after ten weeks.

The onset of radiation pneumonitis seemed to occur earlier in the dog than in the mouse. Because the animals were sacrificed when tests indicated abnormal values, long term follow-up was unavailable. Therefore it is not known whether the initial pneumonitis phase resolved, and if severe early changes are predictive of severe complications in the later portion of the acute pneumonitis phase.

The earliest onset of abnormality as observed on all tests, is shown in Table 2.11. A visual inspection of the dog CT scans was done by an experienced lung radiologist and visual onset of abnormality was recorded. The values for the radioaerosol and MAA perfusion scan as well as those for X-ray were obtained from I. Ahmed (private communication). In this study, the objective was to see which test was the earliest indicator of radiation damage to lung. It is seen that a visual inspection of CT images is advantageous because of overall pattern recognition of damage. However, visual CT is subjective and varies with

experience and image viewing conditions (e.g. level). Moreover it is not useful for quantitative follow-up studies. CT densitometry is more objective since it uses "absolute" CT values, but strict criteria for the tracing procedure, level and window settings and boundary definition must be established. This method of averaging CT numbers, however, dilutes the density increases, which can occur in very localized patches or near the pleura.

Table 2.11: Earliest onset of abnormality (weeks) in dog lung as observed on various tests (M.Sc. thesis I. Ahmed, U of A)

Dog	Radioaerosol (clearance)	MAA (perfusion)	X-ray	CT visual	density
C-566	2	9	8	6	-
C-526	2	6	7	6	6
C-577	1	7	10	5	8
C-694	2	9	9	4	4
C-620	2	14	13	10	10
C-564	6	11	10	10	10
C-568	2	4	4	3	3
D-119	3	6	6	2	4
D-134	4	6	7	7	-
Mean	2.67	8.00	8.22	5.89	6.13
S.D.	1.50	3.08	2.64	2.64	2.69

The CT scan is expected to be superior to conventional X-radiography because the superimposition of structures is avoided. CT is able to detect smaller differences in density, both of small low-contrast focal lesions and of more global increases in the density of the homogeneous structure. Therefore obtaining an average density for a slice of lung should detect such changes.

The earliest indication of radiation damage was shown in a change in clearance of radioaerosol. Visual and quantitative CT showed changes 3 to 4 weeks later. The MAA perfusion scan and conventional X-radiography were the last to indicate changes in lung at roughly 2-4 weeks after the CT results. In this study the MAA perfusion scan was not an early test for radiation damage, as had been expected from the work of Prato (86).

2.3.5 Limitations

As shown previously, the density of dog lung is more variable than in the mouse or human, with a gradient towards higher values from apex to diaphragm, the lower lung being highly vascular as shown in Figure 2.28. This makes the tracing procedure more difficult since we need to exclude large blood vessels.

Radiation changes were observed mostly near the pleura, and may be excluded by the CT averaging procedure. Therefore, the CT number averaging procedure used here may be a conservative estimate of true damage. Furthermore it

is difficult to judge position of the irradiated zone from scan to scan in a dynamic organ such as the lung. Skin markings mark the area on the dog, but the lung seems to wander in and out of this mark, Figure 2.31. Irradiation of the entire dog lung would avoid some of these problems.

Another unknown factor is the short-term and long-term effect of anesthetizing the dogs weekly. It has been pointed out by Hedlund et al. (41) that atelectasis may occur in lung of anesthetized supine dogs breathing spontaneously. A long time was required to perform all tests so that the dogs would be scanned following these tests after being under the influence of anesthetics for 8 hours. There are probably some effects due to the anesthetic, observed occasionally as dense local patches in the lung, suggestive of lung collapse. Anesthetic administered just prior to CT scanning had produced such an effect in mice (section 2.2.3).
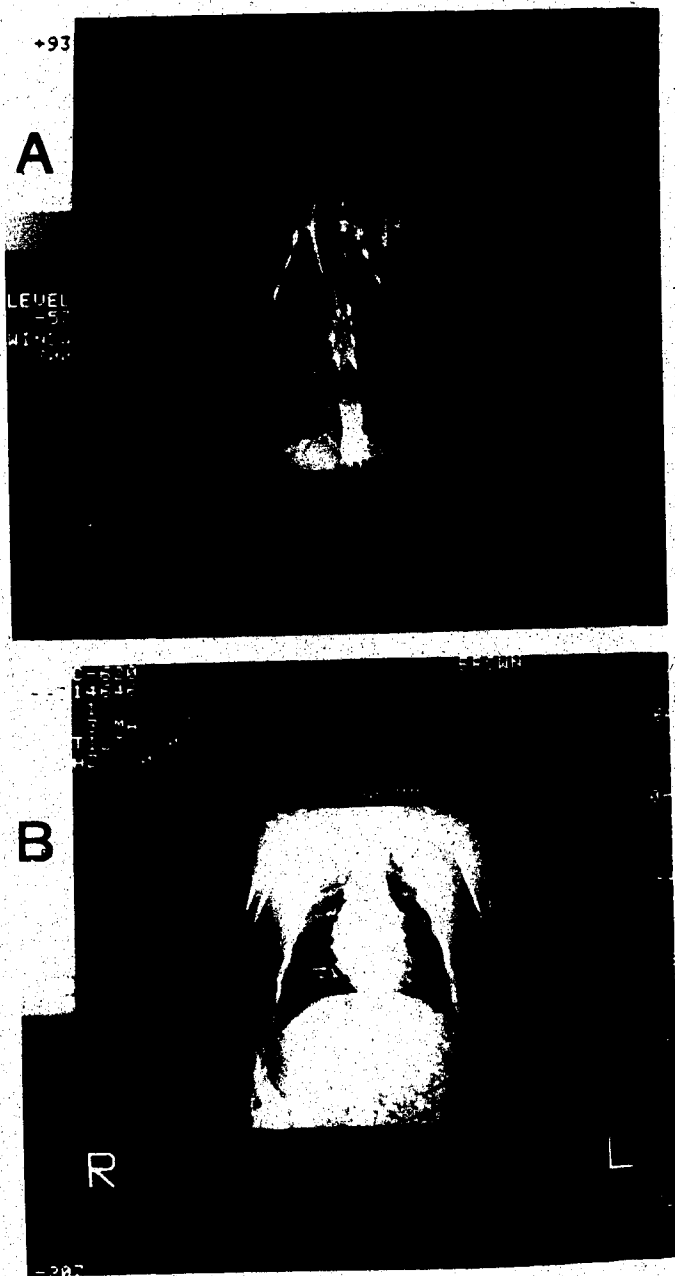
Fig. 2.31 Digital radiograph ("scout scan") of dog
thorax. The boundaries of the radiation
field are marked by positioning clips
on skin marks.

2.4 Clinical Study in Humans

2.4.1 Retrospective Study

In order to determine whether a densitometry study in humans would be useful, 70 thorax CT scans of patients at this Institute were analysed retrospectively. Large blood vessels and obvious carcinomas in lung were excluded during the tracing procedure. The average CT number for lung for 52 patients (of both sexes, aged 50 to 80 years,) was found to be -803.15 ± 34.8 H which corresponds to a lung density of 0.197 g/cm^3. These patients were scanned while holding their breath at _full inspiration_; this reproduced the lung volume for serial scans and also reduced motion artefacts. For each patient there were usually 10 to 17 slices, each 1.0 cm thick through lung. These densities are 12% higher than those published by Van Dyk (129) for this age group at full inspiration. This may be due to the fact that Van Dyk excluded patients with carcinoma in lung, whereas in our study these patients were included; although visible tumor was circumvented during the tracing procedure.

Three cases have been selected to illustrate how quantitative CT compares with other tests such as visual interpretation of the CT scan by a radiologist, conventional chest X-rays, and bronchoscopy. All these cases had tumor in lung. Relevant clinical data is summarized in Table 2.12. CT scans at different times

Table 2.12: Clinical data for three radiotherapy patients

	Case 1	Case 2	Case 3
Patient	65 year old male	66 year old male	63 year old male
Diagnosis	epidermoid carcinoma	epidermoid carcinoma	epidermoid carcinoma
Position of tumor	right upper lobe	left upper lobe	right upper lobe and main bronchus
Radiotherapy	6 MV X-rays 29/12/80-10/02/81	6 MV X-rays 28/01/81-11/03/81	6 MV X-rays 19/02/81-1/04/81
Dose	60 Gy/30 fractions	60 Gy/30 fractions	60 Gy/30 fractions
Field Size	19x14 cm²	16x14 cm²	18.5x17.5 cm²
Position of Field	centre 8.6 cm inferior to the sternal notch, 1.5 cm to the right of mid-line	center 6.3 cm inferior to the sternal notch, 2.9 cm to the left of mid-line	center 6 cm inferior to the sternal notch, 0.5 cm to the right of mid-line

before and after radiotherapy were available for each of these cases.

Case 1: The first CT scan was done 1.5 weeks prior to radiotherapy. The second and third scan were obtained 8 weeks and 21 weeks after a completed course of radiotherapy. CT number data, plotted as a function of longitudinal position in the thorax, are shown in Figure 2.32 A,B,C. The origin is at the sternal notch. The longitudinal border of the radiation field is indicated in Figure 2.32 B,C. The lateral boundaries of the radiation field have also been taken into account. Thus only that part of lung which lies within these borders was sampled in each slice to obtain the CT number data.

In the pre-irradiation scan (Figure 2.32 A) density values in the left lung and lower right lung are normal. Density values in the upper right lung (which corresponds to the position of the tumor) are higher. Obvious solid tumor patches in this area were excluded during the tracing of the lung. Eight weeks after radiotherapy (Figure 2.32 B), there is an increase in density in the left lung throughout the area of the radiation field. In the right lung, at the position of the tumor, there is a decrease in density in some slices and an increase in others. Data in this area is difficult to interpret as there is radiation damage superimposed upon tumor regression. However, there is a definite radiation reaction in the opposite normal left lung. These findings

Fig. 2.32 The average CT number (N_{CT}) for each slice in lung for different longitudinal positions in the thorax (A) 1.5 weeks before radiotherapy, (B) 8 weeks after the end of radiotherapy, and (C) 21 weeks after the end of radiotherapy.

A. CASE No.1 1.5 Weeks Before Treatment

B. CASE No.1 8 Weeks After Treatment

C. CASE No.1 21 Weeks After Treatment
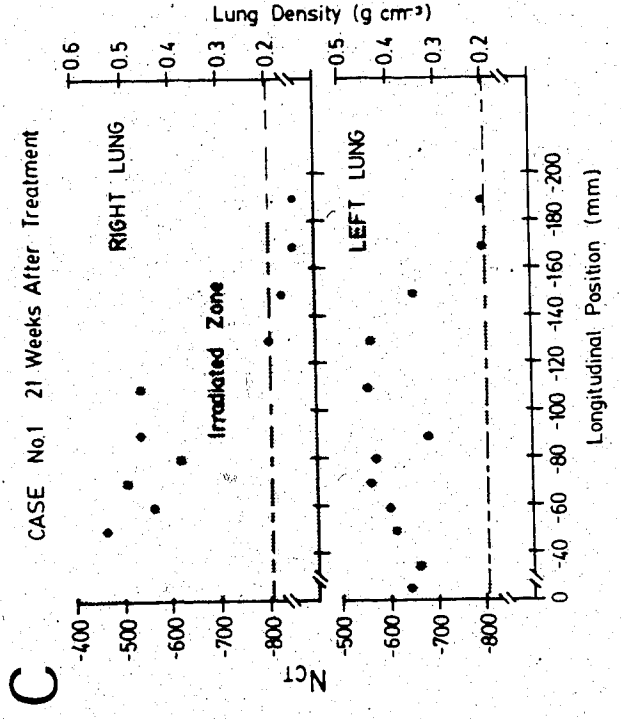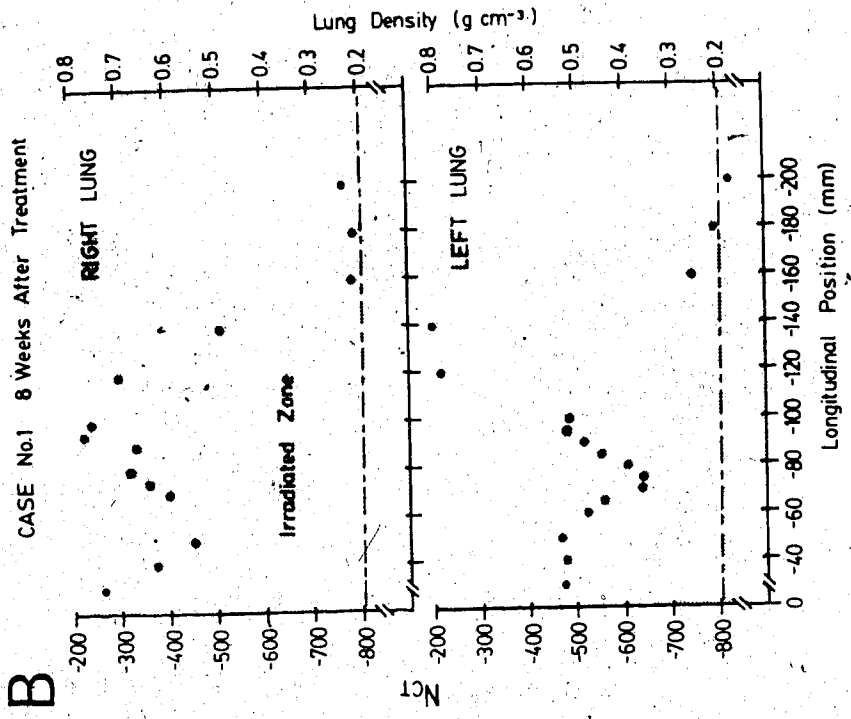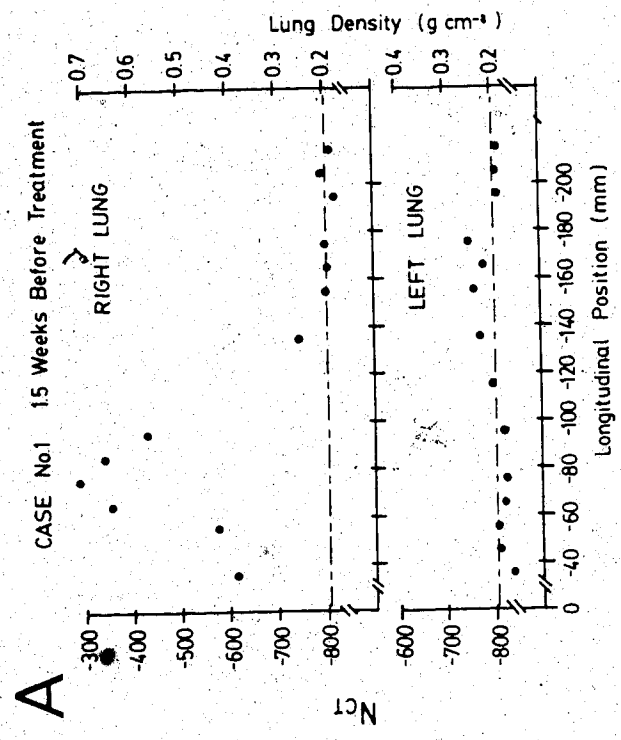
are confirmed by visual interpretation of the CT scan. No recurrent disease was detected by bronchoscopy.

Twenty-one weeks after radiation therapy (Figure 2.32 C), the radiation change in the left lung has resolved somewhat although density values have not returned to normal. There is a further decrease in density in the right lung, indicating further clearance of disease. However, normal density values are not observed, indicating residual disease and/or superimposed radiation damage. These findings are consistent with the radiologist's interpretation of the CT scan.

Case 2: The first scan was done one week prior to radiotherapy. The second and third scans were obtained 5 and 20 weeks after the end of radiotherapy. The CT number data are plotted as a function of longitudinal position in the thorax in Figure 2.33 A,B,C. Five weeks after radiotherapy, CT numbers are slightly higher in the right lung. The tumor in the left lung seems to have cleared, but the lung tissue is of higher density (0.28 g/cm^3) than normal, indicating possible radiation damage. No tumor is detected by visual inspection of the CT scan or on the chest X-ray. Twenty weeks after radiotherapy the density throughout the right lung remains the same. However, in the left lung there is an increase in density at the position of the primary tumor and within the radiation field, relative to the previous scan. This could be due to radiation change and/or recurrence of tumor; on visual

Fig. 2.33 The average CT number (N_{CT}) for each slice in lung for different longitudinal positions in the thorax (A) 1 week before radiotherapy,

(B) 5 weeks after the end of radiotherapy, and

(C) 20 weeks after the end of radiotherapy.

CASE No.2 5 Weeks After Treatment

CASE No.2 1 Week Before Treatment

CASE No.2 20 Weeks After Treatment
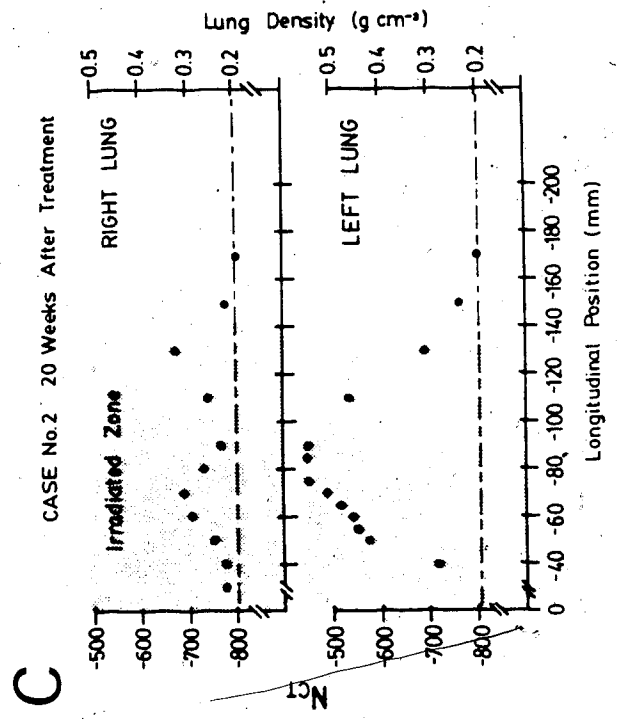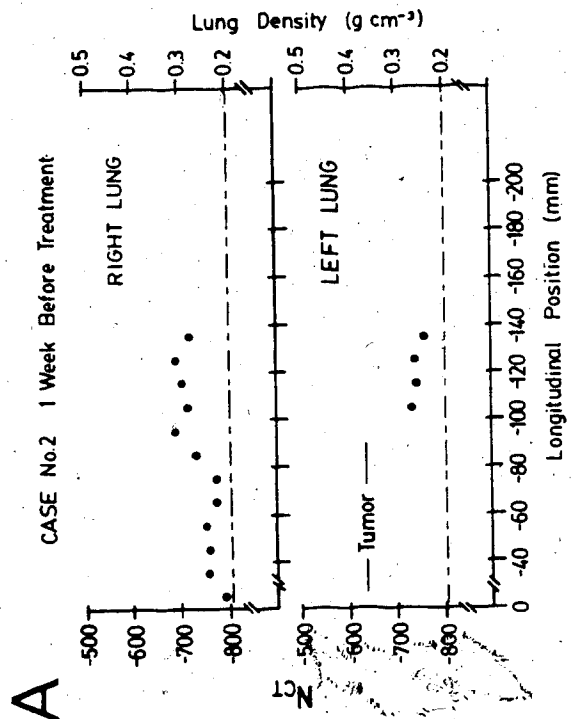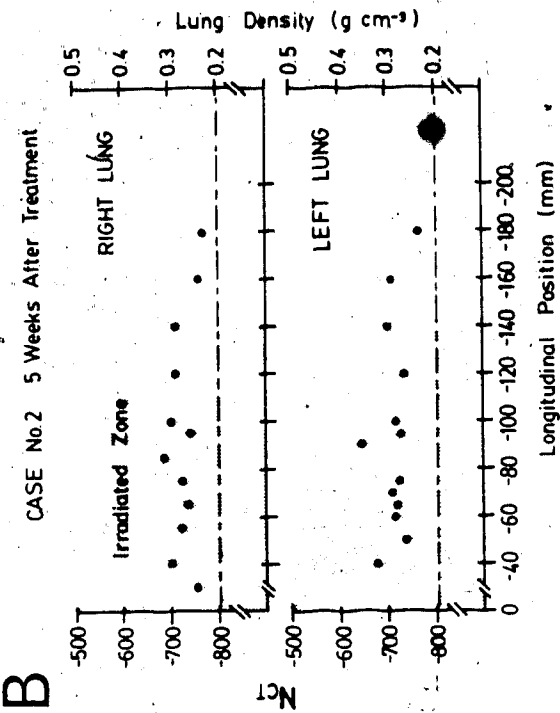
inspection, this "haziness" is suggestive of radiation changes, but residual disease cannot be ruled out. Thus the CT number analysis is consistent with other tests, particularly the CT image inspection. Comparisons to previous scans, however are essential for interpretation. The visual inspection of the CT image is subjective, whereas quantitative CT is more objective. It provides information on the extent and severity of lung damage.

Case 3: There is one clear case of radiation pneumonitis. The diagnosis was made by the radiologist from the CT scan and confirmed by a pathologist at autopsy. This patient received radiotherapy for epidermoid carcinoma of the lung to a dose of 50 Gy in 25 fractions over a period of 35 days. Two large fields (18.5x17.5 cm^2) were used initially in a parallel-opposed arrangement. At the end of this treatment, a "boosting" dose of 10 Gy in 5 fractions over 7 days, using two smaller fields (16x14 cm^2) was delivered. Two CT scans were available for this patient, one before irradiation and another five and a half weeks after treatment. For these two scans, CT numbers are plotted as a function of longitudinal lung position in Figure 2.34 A,B. Before irradiation, the CT number values in regions with no tumor lie in the normal range, but after irradiation CT numbers within the irradiated zone increase dramatically. This effect is confined to the radiation field as indicated in Figure 2.34 B. However, an unexpected result is also
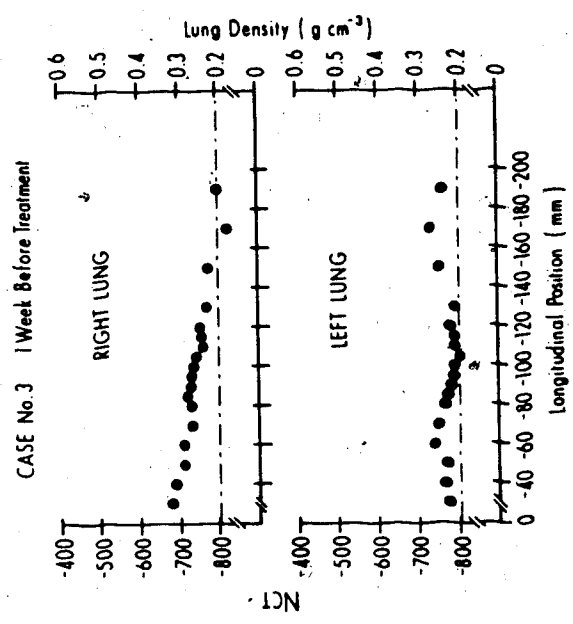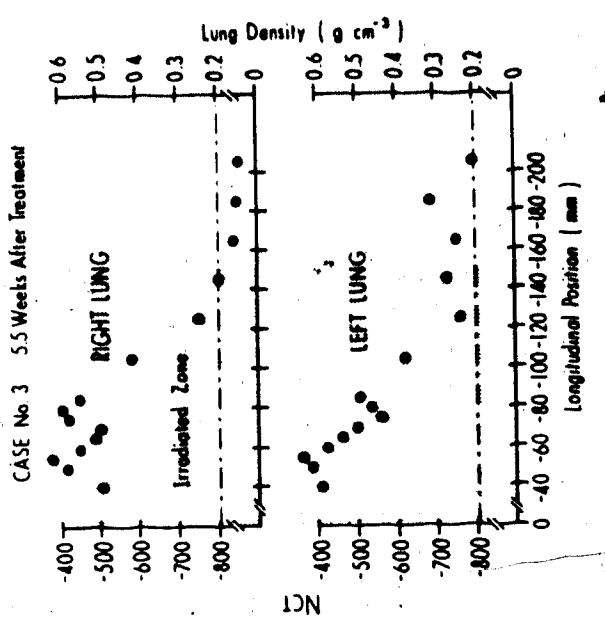
Fig. 2.34 The average CT number (N_{CT}) for each slice in lung for different longitudinal positions in the thorax (A) 1 week before radiotherapy.

(B) 5.5 weeks after the end of radiotherapy.

observed; lower density develops in the unirradiated lung. This is probably due to a compensatory effect causing the undamaged lung to overventilate. The patient deceased eight and a half weeks after completion of irradiation at which time all clinical symptoms of radiation pneumonitis were present. The appearance of radiation pneumonitis in humans is shown in the CT scan of Figure 2.35. This particular case is an extreme case where radiation pneumonitis was clearly visible and CT number analysis would hardly be necessary. Nevertheless, the severe changes were apparent three weeks before the patient's death.

2.4.2 Prospective Study

We expect CT number analysis to be more useful in cases where the entire lung is irradiated and diffuse changes may occur affecting the entire lung. Therefore a study was initiated in order to monitor lung density values at various intervals in patients receiving hemi-body irradiation at this Institute. The patients used in this study were diagnosed with small-(or "oat") cell lung cancer which is one of the most aggressive and lethal tumours (122). The treatment strategy may include chemotherapy, systemic and local radiotherapy, or combinations thereof (121,122).

2.4.2.1 Irradiation (UHBI) Protocol

Fig. 2.35 CT scan of human lung (A) normal lung
(B) radiation pneumonitis in lung. The
radiation damage is confined to within
the borders of the radiation field.

In order to obtain the large field necessary for upper half-body irradiation the patient lies on a couch near the floor at a distance (SAD) of 200cm from the source. Arms are at the side with forearms crossed on the chest. The field size is chosen large enough so as to enclose the entire upper body superior to the umbilicus. Dose is delivered with parallel-opposed 6 MV X-ray fields along the anterio-posterior direction. The anterio-posterior separation distance is measured in the mid-saggital plane of the patient at 10 cm intervals starting from the umbilicus. A mean separation is then calculated, and is used in dose calculations. A shield is used for the entire lung, thus allowing generally higher doses of radiation to be delivered to the disease sites. The typical field size is 40.5x40.5 cm^2, and the total dose of 20 Gy is delivered in 8 fractions; the lung dose (uncorrected, see section 3.2 of this thesis), is kept at 6 Gy/8 fractions at the position of mid-plane. The lung shields are beam divergent blocks of "cerrobend" 26mm in thickness (1 HVL=15 mm) constructed to match the individual patient by shape.

2.4.2.2 CT Densitometry

Scans were obtained according to the schedule shown in Figure 2.36.
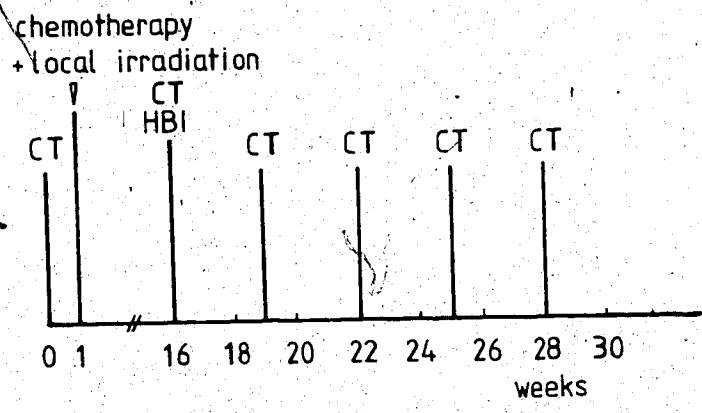
Fig. 2.36. Treatment schedule for hemi-body

radiotherapy patients

The actual time of scans deviated from these nominal times

because of difficulties in having patients comply to this

schedule; this group of patients is very ill, and some

deceased during the course of study.

During the scanning procedure, five transverse

slices, each 10 mm in thickness, were obtained through the

thorax. The CT number data are recorded and averaged as

described in the animal experiments (section 2.2). The

sternal notch is the reference landmark and anatomical

origin ("0" mm). The CT data are presented in Figure

2.37. The control density value is that given for the

"normal" patients of this age group as published by Van

Dyk (129). The data are plotted for the individual
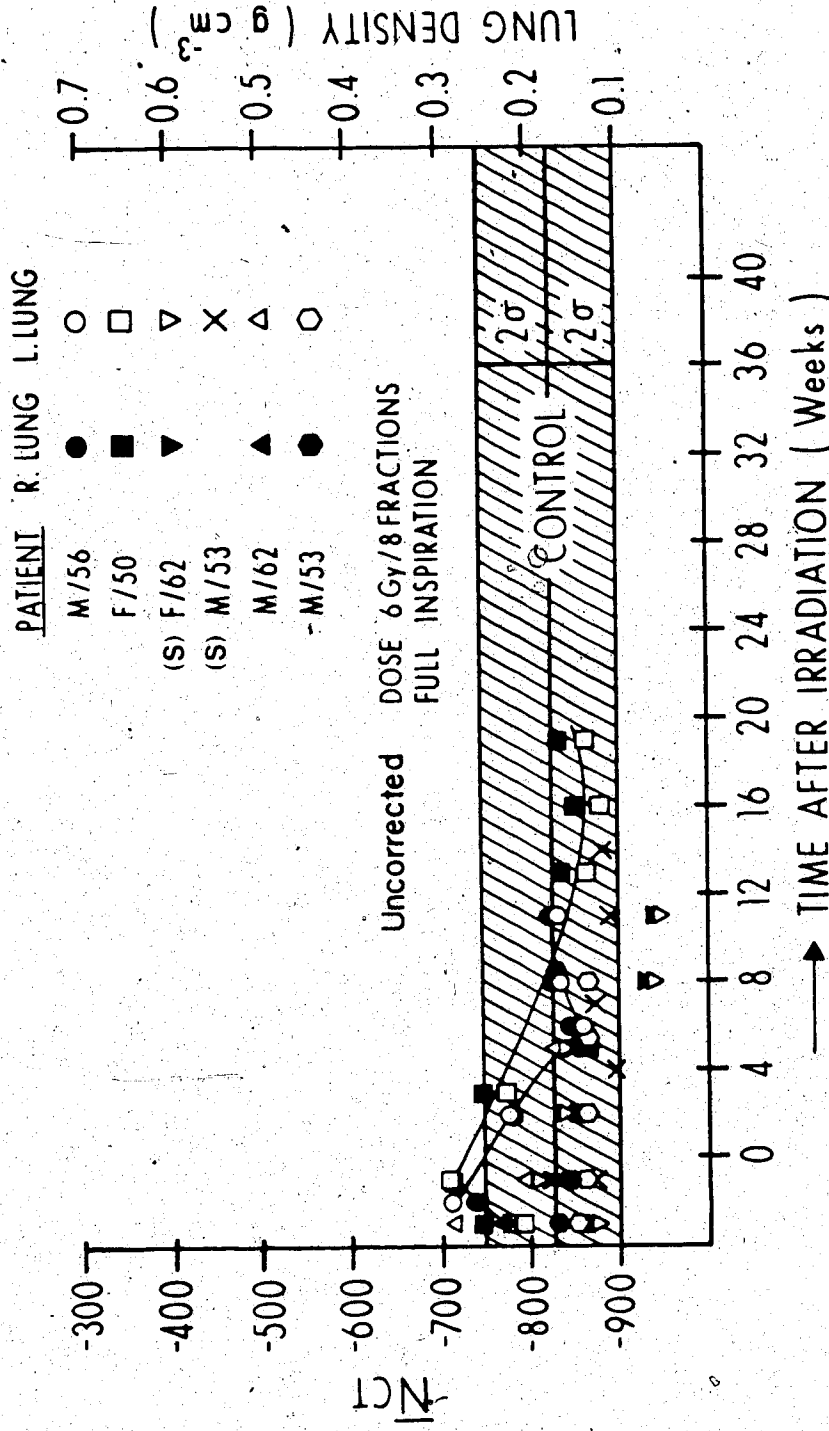
Fig. 2.37 Average CT number ($\bar{N}_{CT}$) for individual patients receiving hemi-body irradiation. Right and left lung data are plotted separately. The general decrease is due to clearance of disease and absence of pneumonitis.

patients, with right lung (R) and left lung (L), separately. Two of the patients, (S), had surgery as well and one notes that the remaining good lung is of lower density, presumably expanding in order to compensate, for the missing lung.

For all patients there is an initial decrease in density which is attributed to clearance of the primary disease, as seen repeatedly in the retrospective study. Thereafter, all values return to normal and remain there for the duration of the scans. This is an expected result since the dose delivered to lung (6 Gy (uncorrected) in 8 fractions), is not expected to produce radiation pneumonitis. At this dose level, there appears to be little synergistic effects of radiation and chemotherapy. Since this study was completed, the dose to lung has been increased to 10 Gy in 8 fractions by decreasing the thickness of the lung shields for all subsequent patients, with the intent of improving control of the disease.

2.5 Summary - CT Densitometry

The CT densitometry studies are summarized in Table 2.13:

Table 2.13: Summary of CT densitometry studies

Species	Number	Sample Volume	Doses	Observed Changes
Mouse	142	all	5 - 14 Gy	15 - 24 weeks
Dog	12	lower right	10, 20 Gy	4 - 14 weeks
Human	3	irradiated zone	60 Gy/30 fractions	5 weeks
Human	6	all	6 Gy/8 fractions	none

From the mouse study one notes that CT densitometry is sensitive enough to detect the histologic changes observed in lung during the acute pneumonitis phase in animals. The time-course and severity of changes corresponded to times of observed microscopic changes. Even though the mouse lung is very small, only 0.4 ml in volume, significant CT number changes were observed before any visible changes were apparent. The CT number changes quantify radiation damage; a change in density of more than 40% was predictive of death in the ensuing two weeks. Not enough animals survived this phase, so that the fibrosis (late) stage of lung damage could not be observed. Due to the large number of animals in the study, good statistics were obtained.

From the dog study it appears that radiation pneumonitis occurs at earlier times in this species than in the mouse. Due to the fact that the dogs received a high local dose to the lower zone of the right lung, CT visual changes were observed as early as CT number changes. Radioaerosol clearance was an even earlier indicator. But since there was no long term follow-up of the dogs, it is not known how well these early tests quantify later radiation damage. Since many cell types are involved in lung damage, it is not clear whether the cell that indicates an early change in function will be the cell type involved in the critical malfunctioning of the lung during the clinical manifestations of radiation pneumonitis. Long term follow-up and irradiation to the entire lung would be desirable in order to investigate which of the tests most accurately predicts a severe effect in the late portion of the acute pneumonitis phase. The most useful test for radiation damage to lung may not be the earliest test but the quantitative test which will give information as to what level of damage will predict severe complications. In addition, we wish to obtain a dose-response curve so that doses to lung can be kept within safe limits.

In the human (retrospective) study, CT number analysis yielded quantitative information about radiation damage as well as clearance or recurrence of tumor, and these findings agreed well with independent tests. In the

human hemi-body (prospective) study, CT numbers indicated initial clearance of disease and remained within normal limits thereafter. This is as expected, since dose to lung was too low to produce severe radiation damage. In subsequent patients, dose to lung has been increased to 10 Gy/8 fractions in order to improve the "therapeutic ratio" of disease control to complication.

FUTURE WORK

Since much work is being done in mice, and radiation effects in mouse lung are well documented, it would be desirable to follow a group of mice irradiated to sublethal doses into the intermediate and late fibrosis stage and continue the scanning. Such a study is now in progress (Dr. G. Miller, private communication).

For dogs, whole lung irradiation would facilitate interpretation, and long term follow-up might indicate which test quantifies relevant radiation damage, and whether the test showing a severe early response predicts the later response. A group of controls on whom all tests are done at the same time as the irradiated animals would be necessary in order to show what effect the weekly anesthetic or the tests per se have on the dogs.

In the humans, doses are kept low in order to avoid radiation damage to lung. The study is ongoing with new HBI patients receiving higher doses. But many patients are quite ill and very few complete the study. Possibly

patients receiving much higher doses <u>locally</u>, using multi-field irradiation, could be monitored.

From this work on CT densitometry of lung, the ideal experimental animal to use might be the rat, for the following reasons: 1. The lung of the rat is sufficiently large and has a nice homogeneous appearance on the CT scan as shown in Figure 2.25. 2. Rats could probably be well immobilized for CT scanning without anesthetic. 3. Facilities for keeping rats exist in many laboratories and many animals could be used in the study to obtain data with good statistics. As well, effects of fractionation, chemotherapy, and radiation response modifying drugs need to be investigated to obtain reliable dose-response curves.

3. RADIATION DOSE IN LUNG

3.1 Introduction

In many radiotherapy centres, radiation fields which encompass one half or the entire body are used to treat systemic or disseminated cancer. Total body irradiation (TBI) is used prior to bone marrow transplantation in the treatment of acute leukemia. Radiation doses to the total body in the range of 8 to 10 Gy destroy leukemic cells and also suppress the immune response in order to avoid graft rejection. Body doses of less magnitude (1 to 3 Gy) are used to treat radiosensitive malignant diseases such as lymphosarcoma, Hodgkin's disease, and Ewing's sarcoma (6, 32,59). Half-body irradiation (HBI) is used to treat widely disseminated and advanced disease (120,121), or as adjuvant therapy for tumors with poor prognosis. In these cases, the main result is rapid relief of pain, sometimes within 24 hours, in patients with severe pain which cannot be controlled even with high doses of analgesics. This palliative benefit often continues for the remainder of the patient's life. In addition, the tumor and metastatic burden is decreased, thus resulting in improved quality and quantity of survival for the patient. So far, clinical results are preliminary for both TBI prior to bone marrow transplant and for HBI but they are encouraging (27,100).

Different treatment techniques are used in the

various radiotherapy centres. These differences occur in the energy of radiation used, the patient positioning, the dose prescription, the dose rate, as well as the use of beam modifiers such as tissue compensators and shielding. Therefore direct comparisons of results are difficult. The techniques used in North America and England (reference 59), and in European centres (reference 6) have been reviewed elsewhere.

Patients receiving TBI or HBI treatment are often sick and uncomfortable; it is desirable to give the treatment as quickly as possible. In bone marrow grafting, the patient should also receive the marrow transplant as soon as possible. Thus, a single dose at high dose-rate (eg. 200 cGy per minute) is more desirable. However, from radiobiology studies this is not optimum from the viewpoint of normal tissue recovery. The maximum therapeutic ratio (i.e. "kill" of target cells relative to normal tissue damage) is the goal. Radiobiology studies indicate that the therapeutic ratio may be greater for irradiation at low dose-rates or for total dose delivered in multiple treatment sessions (83,84). All of the major organs subject to radiation toxicity during TBI and HBI have capacity to repair sublethal damage between dose fractions; this is often not the case for the target leukemic or cancer cells. In upper HBI, the lung is the dose-limiting organ. Clinically, the discrepancy between practicality and

radiobiological findings is only being reviewed now for dose fractionation in large field radiotherapy (120).

For TBI to be effective, a sufficiently high and uniform dose should be delivered to the entire body. However, significant dose inhomogeneity will occur because of variable tissue thickness and composition throughout the body. Therefore achieving a homogeneous dose distribution over the entire body is a difficult physical problem. Sometimes it may be desirable to obtain higher or lower doses to various parts of the body depending on the location of critical or previously-treated organs.

Generally, conventional treatment machines are used for these treatments. In order to produce large fields, extended source-to-patient distances are used, while dose uniformity is achieved with parallel opposed beams. Acceptable dose rates and dose-uniformity are obtained with high energy X-rays produced in linear accelerators (linacs) (1). In one institute, a specialized Cobalt-60 machine has been designed specifically for TBI and HBI (130).

For larger fields and distances, the dosimetry data obtained for smaller fields may not be appropriate and must be verified (124). Discrepancies have been reported because of differences in backscattering, electron contamination, dose ratios (e.g. tissue-air ratios), and corrections for tissue inhomogeneities. The following parameters are affected:

(a) Inverse square law

The inverse square law may not be appropriate because of substantial photon scattering from the surroundings (e.g. floor) and dose-rates must be verified at the large distance.

(b) Tissue-air ratios and Tissue-phantom ratios

The independence of TAR (tissue-air ratio) and TMR (tissue-maximum ratio) on distance to the source should be verified. TAR's and TMR's are usually measured in a semi-infinite phantom: In large field irradiation, the radiation field may be larger than the body, and a reduction in dose due to scattered radiation occurs relative to the "full" semi-infinite phantom. According to Faw and Glenn (26) the dose depends on the field size or the phantom size, whichever is smaller.

(c) Electron contamination

Electron contamination of the surface dose due to collimators and shielding block trays will be less of a problem since the patient surface is further away from them. However, surface dose may still be significant because of scattering from surrounding materials, including backscattering and scattering in the intervening volume of air. The position of maximum dose d_{max} should be verified. If sufficient backscattering material is not provided behind the patient, the exit dose may be low and that part of the patient may be underdosed (32).

(d) Inhomogeneity corrections

Since in HBI or TBI the complete lung will be irradiated, lung dose corrected for tissue heterogeneities must be determined accurately for individual patients. This is crucial because the radiation pneumonitis syndrome is significant when the total lung volume is irradiated to a high dose in a single (or a few) fraction(s). This has proven to be the major (and fatal) toxicity for upper HBI (100). A slight increase in dose produces a dramatic increase in incidence of radiation pneumonitis, but a sufficient dose must be delivered to achieve the therapeutic effect. There are several computational methods available to correct for inhomogeneous tissues and these will be discussed and validated in section 3.2. Dose perturbations due to bone inhomogeneities at megavoltage energies are usually small and neglected in HBI.

At our Institute, HBI is performed at a source to patient surface distance (SSD) of 200 cm and with a field size dependent on the size of patient. Dosimetry measurements reported in this thesis were performed for field sizes up to 60x60 cm^2 and at small and large distances from the source. A 6 MV linear accelerator (Siemens Mevatron VI) is used for the HBI treatments. Therefore most of the dosimetry was performed on this treatment unit. Some measurements were also performed on a Cobalt-60 unit as a reference "standard" radiation.

3.1.1 Linear Accelerators

The major source of radiation for radiotherapy since 1951 has been the photon emissions (1.17 and 1.33 MeV) of radioactive Cobalt-60. However, in the last decade the higher energy X-radiation produced in linear accelerators has predominated. The penetration characteristics of higher energy beams are better suited to the treatment of deep-seated tumors, while sparing surrounding normal tissue. Ideally, such a tumor should be treated with a radiation dose that is zero at the surface, rises to a maximum at the tumor location, and falls off rapidly beyond it. For an opposed parallel pair of radiation beams as used in TBI and HBI, the variation of dose with depth in a 25 cm patient for several of our treatment machines is shown in Figure 3.1. The more uniform dose distribution is obtained with the higher energy machines. The location of maximum dose is deeper for increasing energy. This is caused by the "build-up" of electrons set in motion by the incident photons. The dose at the surface and at shallow depths is affected by low energy electrons produced by the beam-shaping collimating system and any beam modifiers (eg. compensators) placed in the beam (5,54,72,101). The dose at deeper depths is greater for higher energies "primarily" because of the decreased attenuation of the primary beam.

The high energy X-ray beams used in radiotherapy are produced when an electron beam is accelerated to high
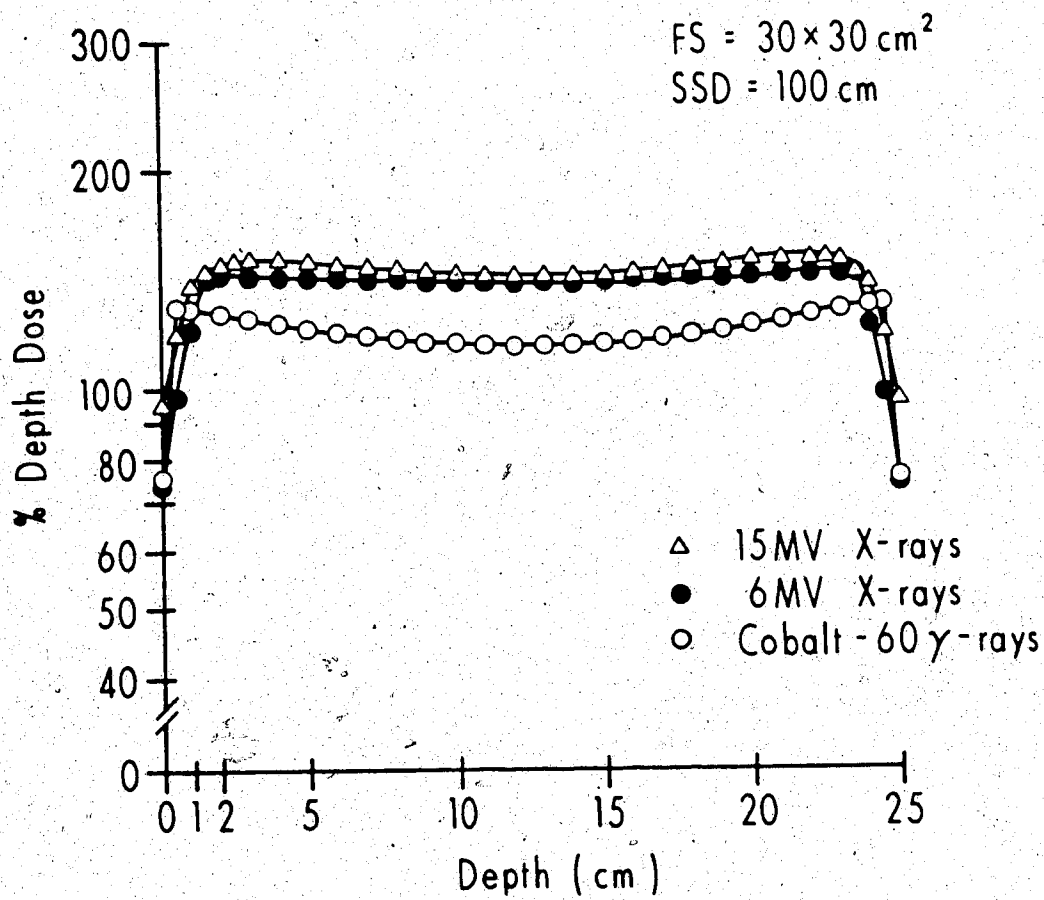
Fig. 3.1 Variation of dose with depth in a water
phantom for a parallel-opposed pair of
radiation fields (30x30 cm²). The
uniformity improves with energy.

velocity and made to strike a target where it produces bremsstrahlung photons. The linear accelerator consists of an electron gun which injects electrons into the accelerator space, and a suitable target for X-ray production. The source of electrons can be a hot filament or cathode in an evacuated tube. These electrons are accelerated to a final energy of the order of 4 MeV to 35 MeV in medical "linacs". Details of the accelerating principles have been reviewed by Karzmark and Morton (57).

On emerging from the accelerator, the pencil beam of electrons is bent by an achromatic 270 degree bending magnet, Figure 3.2. The beam is thereby focussed in 3 dimensions onto a very small "focal point". It can be used as such after scattering on a foil or raster scanning to spread the beam into a uniform electron field. A retractable X-ray target can also be inserted into the beam for photon therapy. These photons produced by high energy electrons are primarily emitted in the forward direction relative to the incident electron beam and an inhomogeneous field intensity is obtained. This problem is overcome by placing a "flattening" filter in the X-ray beam, as shown in Figure 3.2. If properly designed such a filter will produce a homogeneous photon fluence.

The "output" dose rate is monitored continuously by a system of ionization chambers. This system verifies field symmetry and also dosimetry to shut off the machine for a pre-determined dose. A light and mirror combination are

BENDING MAGNET

PENCIL e⁻BEAM

X-RAY TARGET

PRIMARY COLLIMATOR

FORWARD PEAKED X-RAY BEAM

SCATTERING FOIL
(e⁻ therapy)

FLATTENING FILTER
(x-ray therapy)

ION CHAMBERS

SECONDARY COLLIMATORS

SLOT FOR BEAM MODIFIERS, BLOCKS,
COMPENSATORS

"FLATTENED" X-RAY BEAM
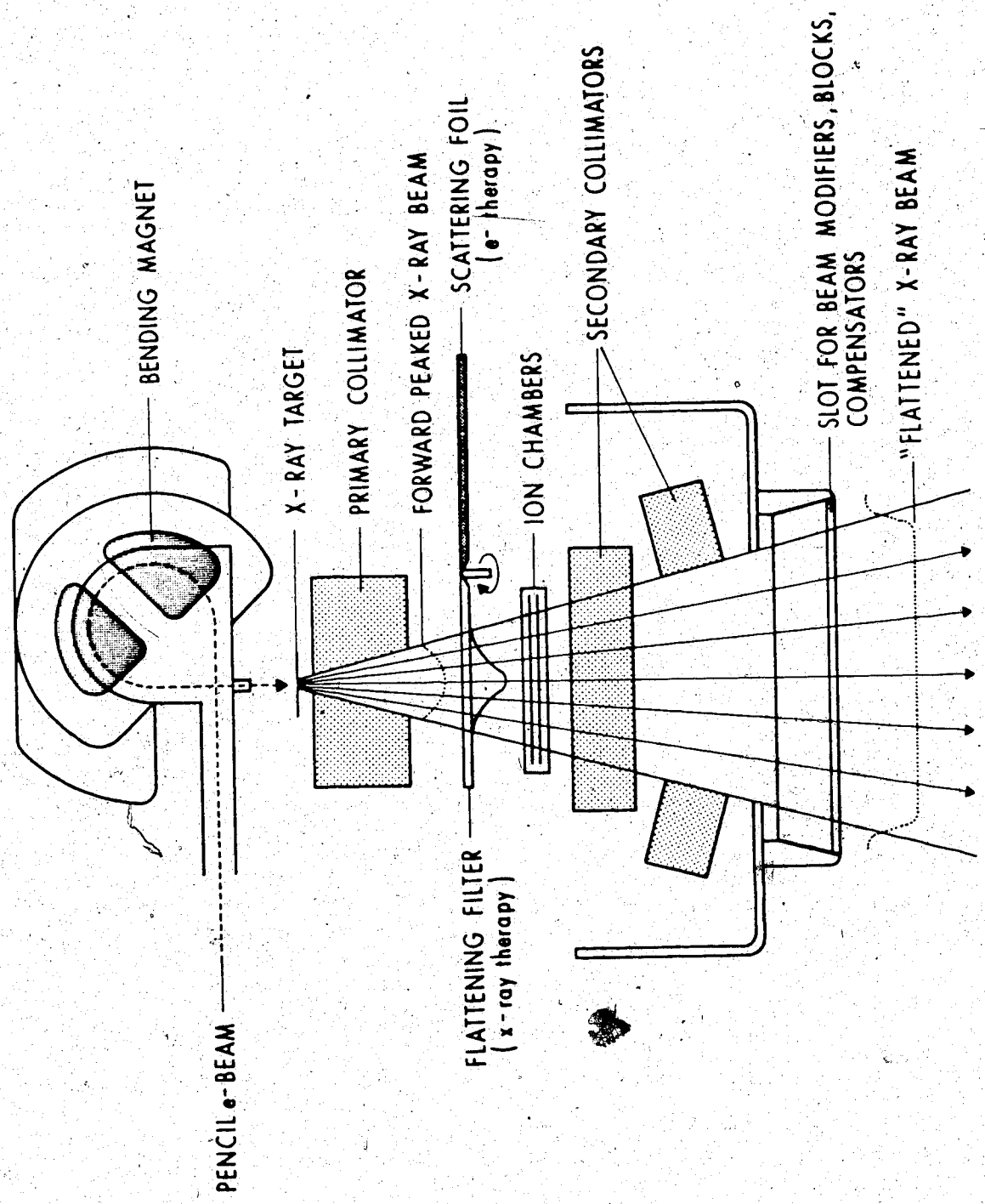
Fig. 3.2 Bending magnet and treatment head of a Siemens Mevatron VI
medical linear accelerator.

used to indicate visually the area of the treatment field. A quality assurance program is necessary to verify that these systems are operating reliably for clinical use (51,57).

A primary collimator limits the maximum field size which can be produced for X-ray therapy. The actual treatment field size is further determined by secondary collimators consisting of four thick metal blocks often made of tungsten. There are support trays which are designed to hold beam modifying devices such as wedges, tissue compensators, and shields.

The Siemens Mevatron VI linac used in our experiments is powered by a 2 MW magnetron, the accelerating structure is 0.82 meters long, of standing wave type. The isocentre is at 100 cm and the maximum field size at this distance is 40×40 cm^2 (57). In this work, large fields were obtained at a distance of 200 cm from the source.

3.1.2 Cobalt-60 Unit

In a Cobalt-60 unit used in radiotherapy the source of radiation is a radioactive isotope. A typical cobalt source contains approximately 278 TBq in a volume of 5 cm^3, and produces a dose rate of approximately 200 cGy/min. at 80 cm from the source. This source is placed at the centre of a lead-filled steel container. During treatment the source is moved opposite an aperture so that the radiation beam can emerge. Various safeguards have

been developed so that the source will always return to the shielded 'off' position, in the event of a machine failure.

Collimators are used to define the field size and a tray to hold beam modifiers is also available. In the experiments reported here, a Theratron 80 and a Theratron 780 (Atomic Energy of Canada) were used.

3.1.3 Dosimetry

The objective in radiation dosimetry is to measure accurately radiation dose at a point in a phantom or in air for calibration. The dosimeter should be small in order to minimize the perturbation in the medium caused by its presence (4). The instrument of dose measurement used in our experiments was primarily the air-ionization chamber. However, for measurements in a humanoid (RANDO) phantom, this dosimeter is impractical. Thermoluminescent dosimetry (TLD) capsules were used instead because they can be inserted into small cavities. Both of these dosimeters will be described briefly in this section.

3.1.3.1 Ionization Chamber

Radiation absorbed dose is defined as

$$D_m = d\bar{E}_{abs}/dm \qquad (1)$$

where D_m = absorbed dose in the irradiated medium

$d\bar{E}_{abs}/dm$ = the mean energy imparted to a small mass, dm.

In radiation dosimetry using ionization chambers, the dose to the medium is determined by measuring the ionization in a gas-filled cavity introduced into the medium. The principles involved are the Bragg-Gray theory and its refinements (4). The Bragg-Gray equation, appropriate for "small" chambers is:

$$D_m = Q/m \ (\overline{W}/e) \ \overline{s}_g^m \qquad (2)$$

where:

D_m = absorbed dose in the irradiated medium

Q = ionization charge collected

m = mass of gas.

$\overline{W}$ = average energy expended by electrons in the gas to produce an ion pair

e = charge of the electron

$\overline{s}_g^m$ = ratio of the mass stopping power of the medium to that of the gas averaged over the energy spectrum for the electrons crossing the cavity.

In order to determine the absolute absorbed dose the quantities m, $\overline{W}$, e, and $\overline{s}_g^m$ must be known, and the charge liberated, Q must be measured. The mass is obtained from a knowledge of the volume of the cavity as well as the density of the gas during the measurement. Generally, the accuracy of ion chamber measurements for megavoltage photon radiation is 2.3% (66), while the precision is excellent (<0.5%).

Two (or more) electrodes of the ionization chamber define the "sensitive" volume of the chamber and collect the charge produced by the radiation. If the radiation consists of photons, these first interact with the wall and gas of the chamber to produce electrons. These electrons then interact through numerous Coulomb collisions within the chamber gas and "strip" electrons from the gas molecules. The result is the production of positive ions and "knock-on" electrons which can attach themselves to other molecules which become negative ions. The electric field across the chamber electrodes collects these ion pairs, thus producing a current. The electrometer attached to the chamber then measures this current (dose rate) or the total charge produced in a certain period (dose), as in Figure 3.3.

In practical use, it is easiest to calibrate ionization chambers in a known radiation field such as Cobalt-60 radiation rather than to determine all the factors of equation (2). After such calibration, the absorbed dose at a point in a medium irradiated with radiation of quality λ may be expressed as (49):

$$(D_m)_\lambda = RN_c N_{TP} C_\lambda \qquad (3)$$

where

R : the ionization reading of the chamber-electrometer pair,

N_c : calibration factor for the reference radiation

GAS-FILLED CAVITY

COLLECTING ELECTRODE

CHAMBER WALL

INSULATOR

V

$$V = IR \longrightarrow \frac{dQ}{dt}$$
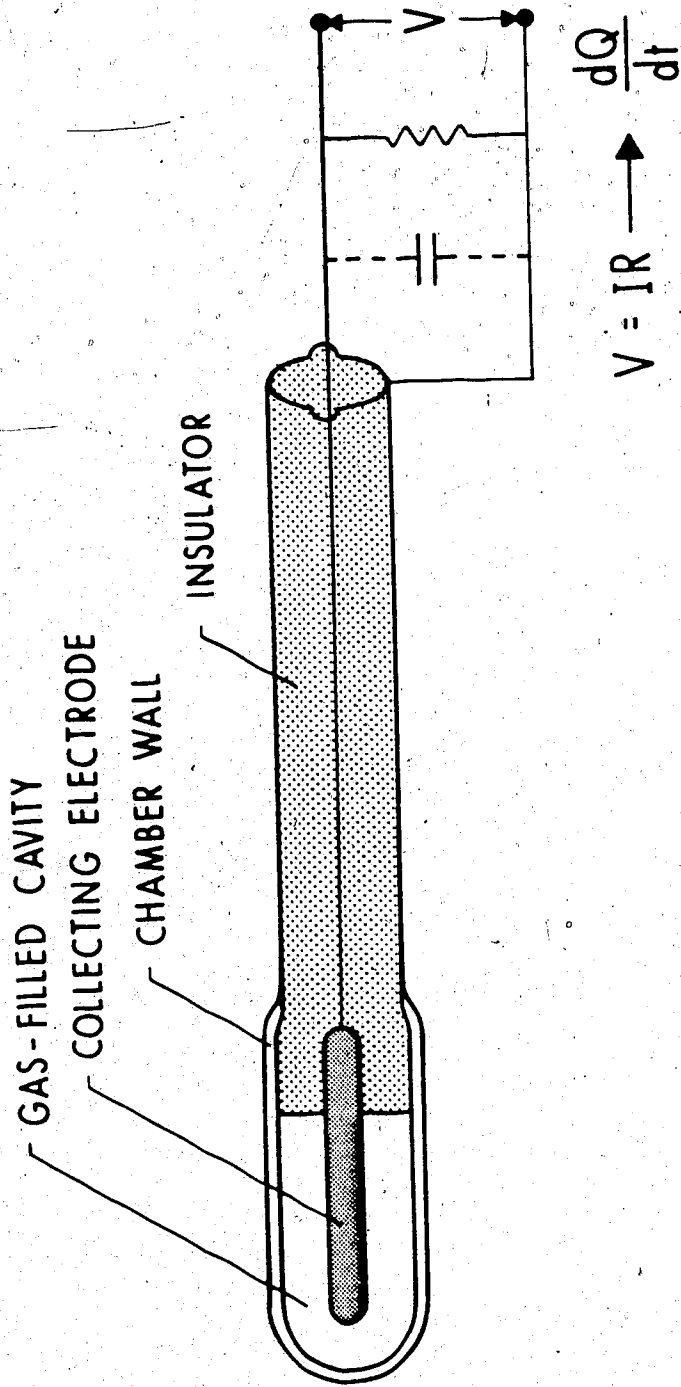
or

$$V = \frac{Q}{C} \longrightarrow \text{TOTAL } Q$$

Fig. 3.3 Schematic diagram of an ionization chamber with associated electrometer. The chamber can be used to measure dose rate (current mode) or dose (charge mode).

(usually Cobalt-60),

N_{TP} : temperature-pressure correction for the unsealed
chamber.

The factor C_λ includes all other factors necessary to
convert the reading for the reference radiation into
absorbed dose in the medium for the radiation energy being
used. The overall uncertainty in this determination of
absolute absorbed dose is 2.3% (49,54,66), mainly because
of this factor. The ionization chamber has great
precision or reproducibility (<0.5%) and can be used over
a wide range of photon energies (10 kV to 50 MV) and
fluences (10^{-3} cGy/min to 10^5 cGy/min) and various types
of radiations, including electrons and neutrons, for which
a different C_λ factor is needed.

In our dose measurements a Capintec PR-06C air
ionization chamber was used. The characteristics of this
chamber are listed in Table 3.1. This chamber was
connected to a calibrated electrometer (Capintec Model 192
A). Measurements in tissue-equivalent phantoms were
obtained with a 0.5 cm "build-up cap" in place. In
lung-equivalent cork, the build-up cap was removed in
order to observe the effects of electronic disequilibrium.
Under these circumstances, the diameter of the air cavity
was 7 mm, with a radiological wall thickness of only 0.5
mm.

Table 3.1: Characteristics of the PR-06C air ionization
chamber

Sensitivity: 0.200 nC/cGy (typical)

Precision: 0.001 cGy, cGy/min

Chamber Material: air equivalent plastic

Active Volume: 0.65 ml

Diameter: 7.0 mm

Length: 22 mm

Wall thickness: 0.28 mm, 50 mg/cm^2

3.1.3.2 Thermoluminescent Dosimetry (TLD)

TLD is a solid state dosimeter available in the form
of a loose powder, solid chip or rod, or
teflon-impregnated rod or flat disc. A thermoluminescent
phosphor has regular crystal structure, but when
impurities are included imperfections arise in the
lattice. Energy traps arise from these imperfections, and
when the phosphor is exposed to ionizing radiation, many
of the freed electrons (or holes) become trapped at these
locations. Subsequent heating of the crystal will raise
the energy of the electrons sufficiently to be released
from these traps and return to stable energy states with
the emission of light. If the light fluence is measured
and plotted as a function of temperature, the graph
obtained is called a "glow curve". There may be one or
more maxima on the "glow curve" as traps of various energy

depths are emptied.~ The relative amplitudes of the peaks

are an indication of the relative populations of trapped

electrons. The total light emitted during part or all of

the "glow curve", or the height of one or more of the

peaks is related to the absorbed dose in the phosphor (4).

TLD dosimeters are not absolute radiation detectors,

and must therefore be calibrated by exposing the dosimeter

to known amounts of radiation. The quantity directly

measured by TLD is. the energy absorbed by the phosphor

i.e. the dose to the phosphor. This response may be

related by calibration versus an ion chamber to the tissue

dose in Gy.

The instrumentation needed to observe TL is shown in

Figure 3.4. A heating element is used to heat the

phosphor electrically while a photomultiplier tube

measures the emitted optical light. The photomultiplier

current integrated over time is related to the absolute

dose. TL sensitivity is defined as the amount of light

released by the phosphor per unit of radiation dose, the

lower limit depending on the type of phosphor and the TL

reader. Most commercial TLD readers can measure doses as

low as 10 mcGy. ·The upper limit of the useful range is

generally limited by the phosphor alone; LiF is linear up

to 10^3 Gy (111). For normal dosimetry applications, a TL

phosphor must have good light conversion efficiency and be

able to retain electrons trapped for reasonable periods of

time at room temperature. The properties of LiF (Harshaw

128
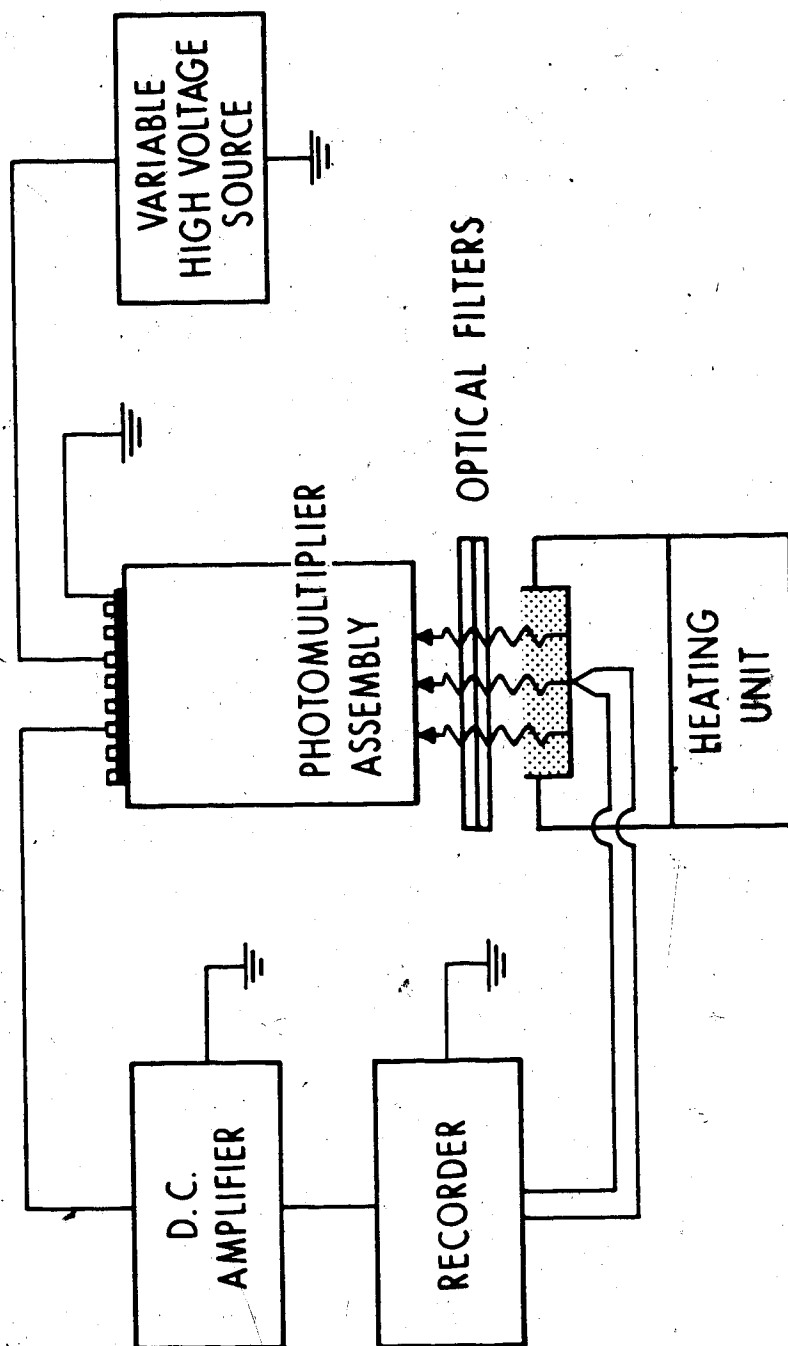
Fig. 3.4 Schematic of the instrumentation necessary to observe thermoluminescence.

TLD-700), the phosphor used in our dosimetry are given in Table 3.2.

The precision and reproducibility of the TL system is not as good as for the ion chamber. With best of care the precision is 3%. The accuracy is of similar magnitude. However, the small size and useful large dose range make the TL dosimeters very suitable for many clinical applications. TLD crystals can be made as small as 1 mm or less. The powder fused into teflon discs or rods can be used for direct insertion into body cavities and thus monitor the patient dose in-vivo. TLD is useful in regions where the dose varies rapidly in space, as near interstitial or intracavitary sources or in the "build-up" region or penumbrae of megavoltage radiation beams. The large useful range make it applicable for radiation protection as personnel monitors.

Table 3.2: Properties of LiF

Density:	2.64 g/cm^3
Effective Atomic Number:	$\tilde{Z} = 8.2$
Temperature of main glow peak:	$190^{\circ}C$
Useful Range:	10 mcGy $- 10^5$ cGy

3.1.4 Tissue-Substitute Materials

In order to obtain dose measurements in materials which can be related to doses in the patient, tissue-substitutes with comparable radiation absorption and scattering properties are used. If materials are to absorb and scatter photons and electrons in the same manner as tissue, all of the following quantities must be matched: mass attenuation coefficient (μ/ρ), mass energy absorption coefficient (μ_{en}/ρ), electron mass stopping power (S/ρ), electron mass angular scattering power ($\theta^2/\rho l$) and mass density, ρ (67).

Since tissues are composed largely of water which is also readily available as liquid is used routinely for measurements of absorbed dose. In our experiments, however, complex geometries and phantoms made of muscle-equivalent as well as lung equivalent materials were required. It would be inconvenient to immerse lung-substitute materials in water. Therefore we considered solid tissue and lung substitute phantoms rather than liquid. These can be cut into various shapes and sizes. The materials used as tissue-substitutes were polystyrene, prestwood (for muscle), and cork (for lung). The physical parameters for these materials are listed in Table 3.3. $\bar{S}/\rho$ is the average mass stopping power for the spectrum of electrons set in motion by photons of energy E , $\bar{\theta}^2/\rho l$ describes multiple scattering of electrons travelling a small path l in the scattering material and

Table 3.3: Physical properties of tissue-substitute materials

| | Photon Energy (E_0) | | | | | |
| | 1.25 MeV | | | 2 MeV (6 MV) | | |
	Water	Muscle	Polystyrene	Water	Muscle	Polystyrene
ρ (g/cm³)	1.000	1.040	1.044	1.000	1.040	1.044
NZ/A (e/g)	3.343×10^{23}	3.312×10^{23}	3.238×10^{23}	3.343×10^{23}	3.312×10^{23}	3.238×10^{23}
$\tilde{Z}$	7.51	7.64	5.74	7.51	7.64	5.74
μ/ρ (cm²/g)	0.0632	0.0626	0.0612	0.0494	0.0490	0.0478
μ_{en}/ρ (cm²/g)	0.0297	0.0294	0.0287	0.0261	0.0258	0.0253
$\bar{\bar{S}}/\rho$ (MeV cm²/g)	2.54	2.51	2.48	2.22	2.19	2.17
$\bar{\theta}^2/\rho l$ (rad² cm²/g)				1.16	1.13	0.911

being scattered, with a mean square scattering angle $\overline{\theta^2}$ (50,54). The densities (ρ) of cork were 0.32 and 0.28 g/cm^3, and of prestwood 1.02 g/cm^3. The relative electron densities (ρ_e') as measured by X-ray computed tomography were 0.32, 0.28, and 1.02. The composition of prestwood and cork is variable and uncertain. In order to validate the use of prestwood, tissue-maximum ratios (TMR's) were measured in prestwood and compared to those measured in water (see section 3.3). Tissue-maximum ratios are a ratio of a dose in the phantom at depth d to the maximum dose in the phantom at depth d_m (54) for a point at a fixed distance from the source. Tissue-maximum ratios were measured for field sizes from 5x5 cm^2 to 30x30 cm^2 for both prestwood and polystyrene. Values were found to be within 1% of those for water. We therefore conclude that polystyrene and prestwood were water equivalent in their radiation absorption, attenuation and scattering properties at the radiation energy used in our experiments (i.e. 6 MV X-rays).

3.1.5 Tissue-Air Ratios, Tissue-Phantom Ratios

Doses along the central axis in water-equivalent media are usually tabulated for different depths and field sizes as tissue-air-ratios (TAR) or tissue-phantom-ratios (TPR). These are defined as shown in Figure 3.5.

TAR = Dose (D)/Dose (D_a)

TPR = Dose (D)/Dose (D_p)

TAR
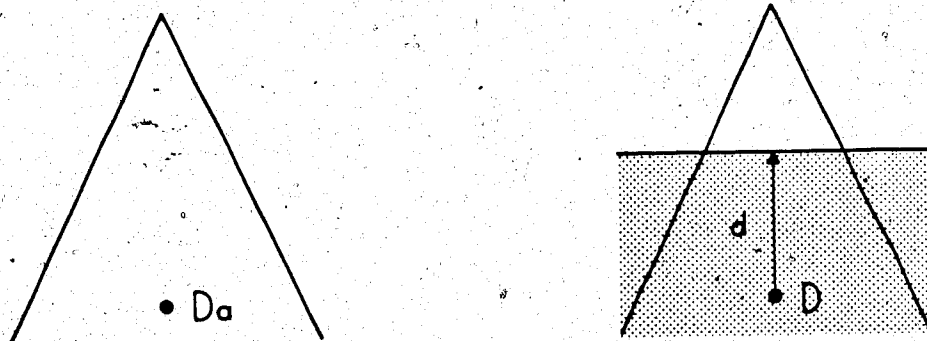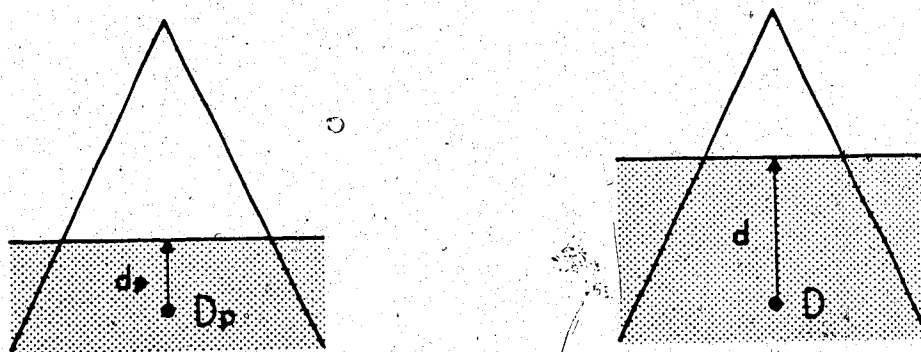
TMR

Fig. 3.5 Definitions of tissue-air and
tissue-phantom ratios.
TAR=D/D$_a$ TPR=D/D$_p$.

If the reference dose D_p is at the point of maximum dose in a phantom, the TPR is called a tissue-maximum-ratio (TMR). Historically TAR's are used for Cobalt-60 radiation and lower energy beams, but TAR's are less easily defined for higher X-ray energies and therefore TMR's are used for the higher energy beams (46). Once the TMR's or TAR's are known, the dose at any point along the central axis in the homogeneous phantom can be obtained by multiplying the TMR (or TAR) at that depth by the reference "calibration" dose, D_m, maximum dose in the phantom, (or D_a, the dose to a small mass of tissue in air).

It is also possible to separate the contribution of primary and scattered radiation by defining a scatter-air-ratio (SAR) or a scatter-phantom-ratio (SPR). These can be calculated from the tissue-air-ratios or tissue-phantom-ratios in the following manner:

$$SAR(d,W_d) = TAR(d,W_d) - TAR(d,0)$$

$$SPR(d,W_d) = TPR(d,W_d) - TPR(d,0)$$

where: $SAR(d,W_d)$, $SPR(d,W_d)$, $TAR(d,W_d)$, and $TPR(d,W_d)$ are the scatter-air-, scatter-phantom-, tissue-air-, tissue-phantom-ratios at depth, d, and for field size W_d. $TAR(d,0)$ and $TPR(d,0)$ are the tissue-air-, tissue-phantom-ratios at depth, d, and for a pencil beam of "zero" field size (54).

3.2 Summary of Calculation Methods

The human body is not homogeneous in external shape or in internal density. The external shape of the body can be altered effectively by using either "bolus" or external beam "compensators". However, internal differences in density affect the dose distribution in a complex way which cannot easily be modified by a simple external "compensator". In this thesis, we are concerned with the accurate calculation and measurement of dose within and beyond lung. We are specifically interested in dose calculations for a lower density object introduced into a water-equivalent medium. This low density inhomogeneity will affect the primary and scattered photon radiation, as well as the transport of electrons set in motion. With improved accuracy in dose calculations, the severity of perturbation of dose distribution by tissue inhomogeneities can be judged, and the possibility of constructing appropriate "compensators" becomes viable.

In order to calculate doses in inhomogeneous media, the usual procedure is to first calculate the dose in water, which is relatively easy to validate experimentally, and then multiply it by an inhomogeneity correction factor (ICF).

$$ICF = \frac{\text{Dose in heterogeneous phantom}}{\text{Dose in homogeneous (water) phantom}}$$

The available inhomogeneity correction methods are summarized in Table 3.4, in order of increasing complexity

(21).

The first two methods only correct for the effect of the inhomogeneity on primary photon fluence. They are based on calculation of a "water-equivalent" or radiological thickness. Suppose the primary beam passes along a path

Table 3.4: Inhomogeneity correction methods

Algorithm	Method can take account of:		
	Longitudinal position of structure	Lateral extent of structure	Electron transport
Ratio of TAR (or Effective SSD) (21)	NO	NO	NO
Batho (7,109)	YES	NO	NO
Lulu and Bjarngard (Batho) (69)	YES	YES	NO
Scaled TMR (this work)	YES	YES	NO
Differential SAR's (13,20)	YES	YES	NO
Equivalent TAR (107,110)	YES	YES	NO
delta-Volume (141)	YES	YES	(NO)*
Convolution (71)	YES	YES	YES
Monte Carlo (17,134)	YES	YES	YES

*under development.

of heterogeneous tissue with a spatially varying relative electron density, $\rho_e'(1)$. Then the water-equivalent depth,

$$d' = \int \rho_e'(1)d1.$$

The tissue-air ratio method gives the correction factor as:

$$ICF = \frac{TAR(d', W_d)}{TAR(d, W_d)} \tag{4}$$

where d' is the water-equivalent thickness, d is the geometric thickness of material and W_d is the beam size at depth d. This correction factor accounts for both beam size and depth of the calculation point, but not the proximity of the inhomogeneity to the calculation point or the lateral extent of the inhomogeneity. The effective SSD (source-skin distance) method is equivalent to the ratio of TAR's except that it uses percent depth doses and an inverse square correction instead of TAR's (21).

A refinement which accounts for the proximity of the inhomogeneity, was developed by Batho (7). It is a semi-empirical method, and its implicit assumptions and derivation are not well documented or understood. It uses TAR's and relative electron densities, and thereby indirectly accounts for the change in the "scattering power" of the inhomogeneity. Originally this method was developed for calculation points beyond an inhomogeneity. It has since been extended to consider points within an inhomogeneity (109). The general form of the Batho

correction factor is:

$$ICF = \frac{\left[TAR(d_2, W_d)\right]^{\rho_3 - \rho_2}}{\left[TAR(d_1, W_d)\right]^{1 - \rho_2}} \tag{5}$$

where ρ_2, ρ_3, d_1, d_2, and W_d are as given in Figure 3.6. This method will be discussed in detail in section 3.5.

A method which accounts for the shape of the inhomogeneity uses the volume integration of differential scatter-air ratios (dSAR) (13,20). The correction factor is given as:

$$ICF = \frac{TAR(d',0) + \sum \Delta s}{TAR(d, W_d)} \tag{6}$$

d' is the water equivalent depth. $TAR(d',0)$ is the zero-area tissue-air ratio, and the integral $\sum \Delta s$ sums scatter contributions from all volume elements in the irradiated volume. The contribution from each individual element is calculated as follows, Figure 3.7:

$$\Delta s = e^{-\mu_w(a'-a)} \left[dSAR\right] \rho_e' \left\{ e^{-\mu_w(\theta)(b'-b)} \right\} \tag{7}$$

where: dSAR is the differential scatter-air ratio for volume element, ΔV, assuming the surrounding medium is water. The remaining terms correct this value for the presence of surrounding structures of non-water density. a' and b' are the water-equivalent depth along the primary path and along the scattered photon path respectively,
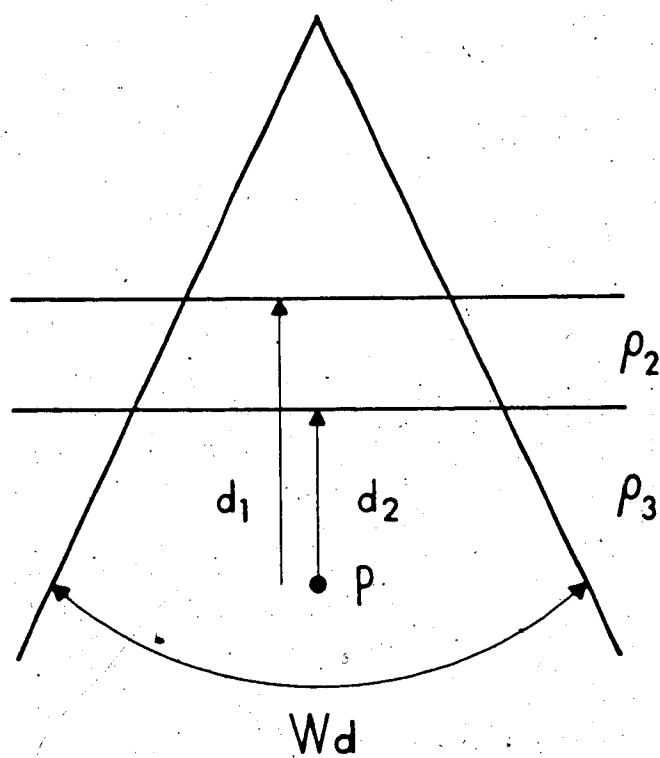
Fig. 3.6 Geometry used for the Batho correction.
ρ_2 and ρ_3 are the electron densities
relative to water.
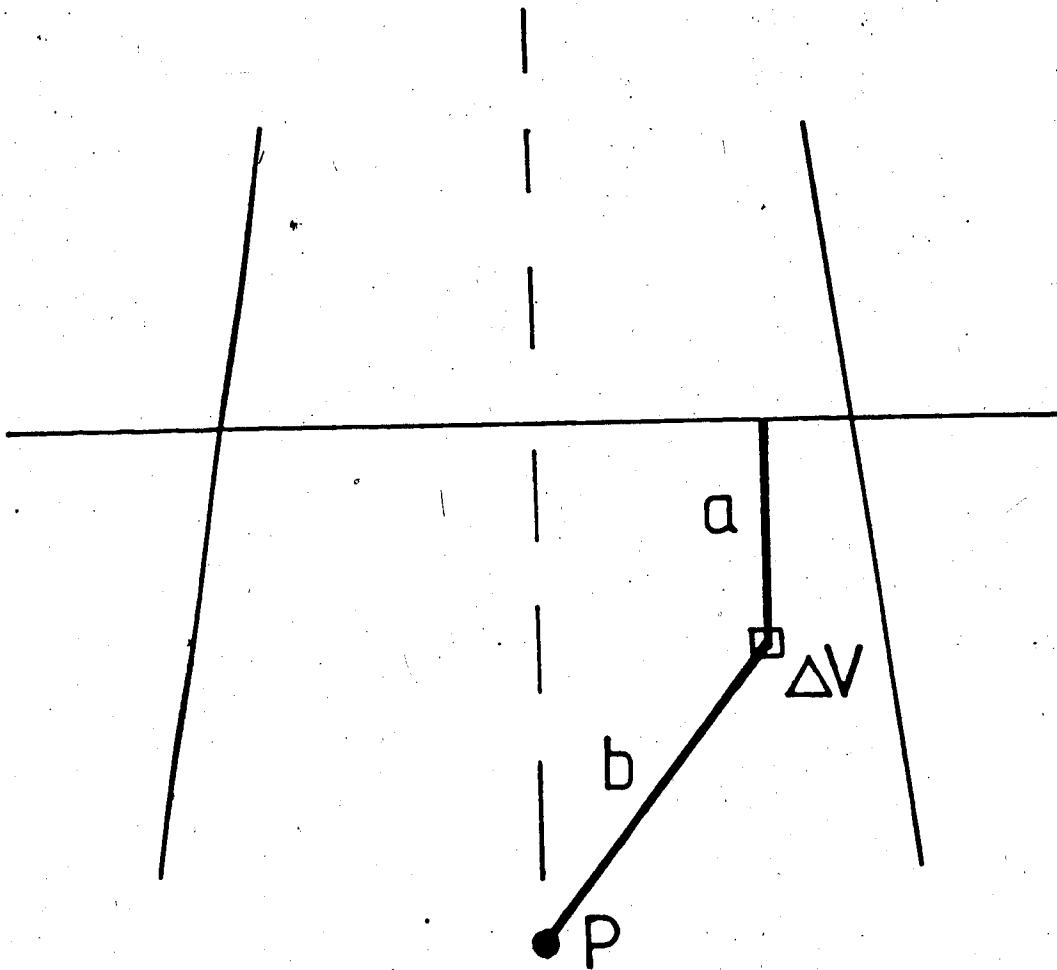
Fig. 3.7 Parameters used in the calculation

of scatter contribution in the dSAR.

assuming single scatter only. a and b are the real (or geometric) path lenghts. ρ_e' is the relative electron density in the scattering volume element, ΔV. μ_w and $\mu_w(\theta)$ are the linear attenuation coefficients in water of the primary and the scattered photon (13). This method lends itself to "pixel-by-pixel" corrections using complete electron density distributions obtained by CT scanning. This method was "ahead of its time" and was the first to separate the primary and scattered radiation components in a heterogeneous phantom. However, all of the multiply-scattered radiation is considered as if it behaves like single-scattered radiation; this may account for poor dose results obtained for large field irradiations of heterogeneous media (107).

The simple ratio of TAR's method (equation 4) has been modified by Sontag and Cunningham (110) in order to also account for the size, shape, and position of the inhomogeneity. This method is called the equivalent TAR method. An effective TAR(d',W_d') is determined where d' is the water-equivalent path discussed earlier, and W_d' is an "effective" field size. The correction factor is :

$$ICF = \frac{TAR(d',W_d')}{TAR(d,W_d)} \qquad (8)$$

d' is easy to obtain, but W_d' is more difficult to obtain since the entire environment of the calculation point must be considered. An equivalent field width is determined as

follows:

$$W'_d = W_d \cdot (\bar{\rho}'_e) \tag{9}$$

$\bar{\rho}'_e$ is the weighted average of all the relative electron densities in the irradiated three-dimensional volume.

$$\bar{\rho}'_e = \int \rho'_e (x,y,z) \; W (x,y,z) \; dV \tag{10}$$

The $W(x,y,z)$ is a set of weighting factors which depend on distance of each scattering volume element from the point of calculation. This method also lends itself to "pixel-by-pixel" corrections (21).

A method which relies on "ray tracing" between the calculation point and the scattering sites has been developed by Wong (141), and is referred to as the delta-volume method. This method calculates the primary dose, and adds first-scatter dose, corrected for heterogeneities. It further adds second-scatter dose, but this component is treated geometrically as first-scatter. Finally a residual term for multiple (>2) scatter dose is added. It is very similar to the volume integration of differential scatter-air ratios, but differs in that it only treats second-scatter as first-scatter, whereas the dSAR method treats all multiple scatter as first-scatter.

With present day computers, calculations with the delta-volume method are long (e.g. a 3D calculation on a VAX-11/780 computer for a 16x16x16 cm³ medium takes 1-2 hours per beam (141), but with development of very large

scale integration (VLSI) "chips" and/or array processors, routine clinical use may be possible in the near future. Furthermore this method has the potential to account for electron transport for high energy X-rays, and is still being actively improved. Another method with similar capabilities, but which uses a convolution principle, is being developed in this laboratory (71).

The latter three methods are complicated and must be performed on computers. The "input" information is the detailed anatomical information available from CT scans. Before the advent of CT scanning, this detailed anatomical information was not available; internal body contours were estimated and this gave rise to errors in dose calculation which were greater than errors due to the simplistic inhomogeneity corrections per se (108). At present, however, detailed anatomical information is available, and the accuracy of dose calculations is limited by the quality of the inhomogeneity correction. Therefore, the complex methods must be validated experimentally and it must be determined whether their use truly improves the accuracy of dose calculation.

The method which can, in principle, overcome all the deficiencies of the above methods uses Monte Carlo simulations (88). This method can "follow" individual photons as they are scattered throughout the patient, and can also consider the energy transport of charged particles from sites of interaction. In order to obtain

reasonable results, however, millions of photons must be considered in order to obtain accurate dose results (17,134). With present day computers, it still takes hours to days of computation to obtain a dose distribution in a simple inhomogeneous medium; this method is not yet practical for routine clinical use. For example, calculations for a 10x10 cm² field of 6 MV X-rays take 60 hours to obtain a dose accuracy of 0.5% on a VAX 11/780 computer (private communication T.R; Mackie). The implementation of the complex methods for HBI is still in the future. We are presently restricted to the simpler inhomogeneity correction methods, with possible modifications, and realize that one method may yield good results in a given situation, but poorer results in another. This is the rationale behind the experiments described in the following sections.

3.3 Homogeneous Phantoms

As noted earlier, the calculation of dose in a heterogeneous medium is preceded by a knowledge of dose in a homogeneous water medium. The dose, D_2, for the situation shown in Figure 3.8 is:

$$\text{Dose } (D_2) = \text{ICF} \times \text{Dose } (D_1)$$

(A) Equivalence of the homogeneous phantoms to water

In order to calculate and measure correction factors in a heterogeneous phantom, various size cork slabs are introduced into a homogeneous medium. For these experiments, homogeneous phantoms composed of slabs are most convenient. Thus, polystyrene and prestwood were used as the homogeneous material. Their equivalence to water and muscle has already been discussed in section 2.1.7 and 3.1.4). Nevertheless, tissue-maximum ratios (TMR's) were measured in polystyrene and prestwood for field sizes 4x4 cm² to 60x60 cm² and are given in Table 3.5. TMR's for the larger fields were not previously available for 6 MV X-rays. For field sizes larger than 35x35 cm², there is a minimal change in TMR with increasing field size, because scattering from "long range" is negligible.

The TMR values plotted at different depths in polystyrene and prestwood are within 1% of those in water up to depths of 20 cm. Beyond this depth, they are within 2 to 3%. These are shown in Figure 3.9 for a standard field size of 10x10 cm² at an SAD (Source to Axis

$\rho_2 \neq 1$

$\rho_1 = 1$

$\rho_1 = 1$

$\bullet D_2$

$\bullet D_1$
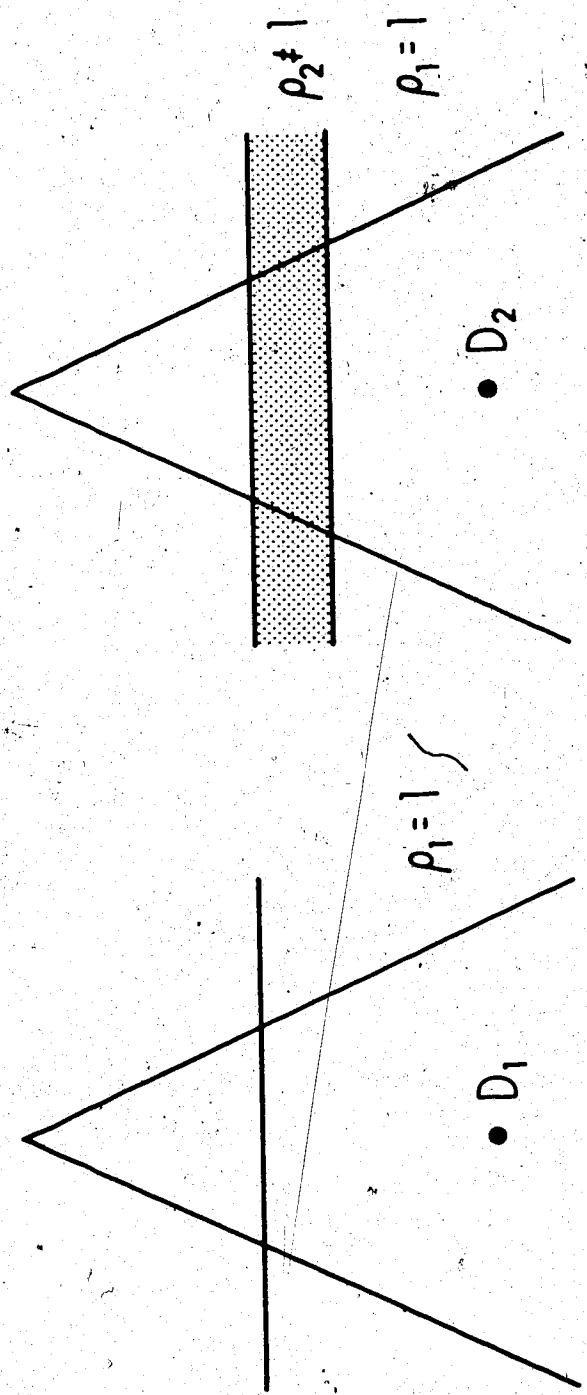
Fig. 3.8 Definition of the inhomogeneity correction factor $ICF = D_2 / D_1$.

Table 3.5: Tissue-maximum ratios for 6 MV X-rays

Depth(cm)	Field size							
	5x5cm²	10x10cm²	20x20cm²	30x30cm²	35x35cm²	40x40cm²	45x45cm²	50x50cm²
0.0	0.118	0.171	0.256	0.324	0.354	0.383	0.411	0.439
1.0	0.706	0.724	0.752	0.775	0.785	0.794	0.804	0.813
1.5	1.000	1.000	1.000	1.000	1.000	1.000	1.000	1.000
2.0	0.985	0.989	0.990	0.992	0.993	0.994	0.994	0.994
3.0	0.956	0.967	0.971	0.977	0.980	0.981	0.982	0.982
4.0	0.927	0.946	0.952	0.961	0.966	0.969	0.970	0.970
5.0	0.889	0.915	0.928	0.941	0.947	0.950	0.951	0.951
6.0	0.850	0.884	0.905	0.921	0.928	0.931	0.931	0.931
7.0	0.815	0.854	0.881	0.898	0.905	0.908	0.909	0.910
8.0	0.780	0.824	0.857	0.876	0.882	0.884	0.887	0.889
9.0	0.747	0.793	0.833	0.853	0.860	0.864	0.866	0.868
10.0	0.714	0.762	0.808	0.831	0.839	0.843	0.846	0.847
11.0	0.683	0.733	0.783	0.807	0.816	0.821	0.825	0.826
12.0	0.652	0.705	0.758	0.784	0.793	0.800	0.804	0.805
13.0	0.621	0.676	0.733	0.760	0.771	0.778	0.782	0.784
14.0	0.590	0.648	0.707	0.737	0.748	0.757	0.761	0.763
15.0	0.566	0.623	0.684	0.714	0.725	0.734	0.739	0.742
16.0	0.541	0.598	0.661	0.691	0.702	0.711	0.717	0.720
17.0	0.518	0.574	0.639	0.670	0.681	0.690	0.696	0.699
18.0	0.495	0.551	0.617	0.648	0.660	0.669	0.675	0.678
19.0	0.472	0.528	0.595	0.627	0.639	0.648	0.654	0.658
20.0	0.449	0.505	0.572	0.605	0.618	0.627	0.633	0.637
21.0	0.428	0.483	0.552	0.586	0.598	0.607	0.613	0.618
22.0	0.407	0.461	0.531	0.567	0.577	0.586	0.594	0.599
23.0	0.391	0.444	0.513	0.548	0.557	0.565	0.572	0.576
24.0	0.376	0.426	0.496	0.529	0.537	0.544	0.550	0.554
25.0	0.360	0.408	0.478	0.510	0.518	0.525	0.531	0.534
26.0	0.344	0.391	0.461	0.491	0.499	0.506	0.512	0.514
27.0	0.328	0.373	0.444	0.474	0.482	0.490	0.496	0.499
28.0	0.312	0.356	0.426	0.458	0.464	0.473	0.481	0.484
29.0	0.296	0.338	0.409	0.440	0.448	0.456	0.464	0.467
30.0	0.280	0.321	0.391	0.422	0.431	0.439	0.446	0.451

148
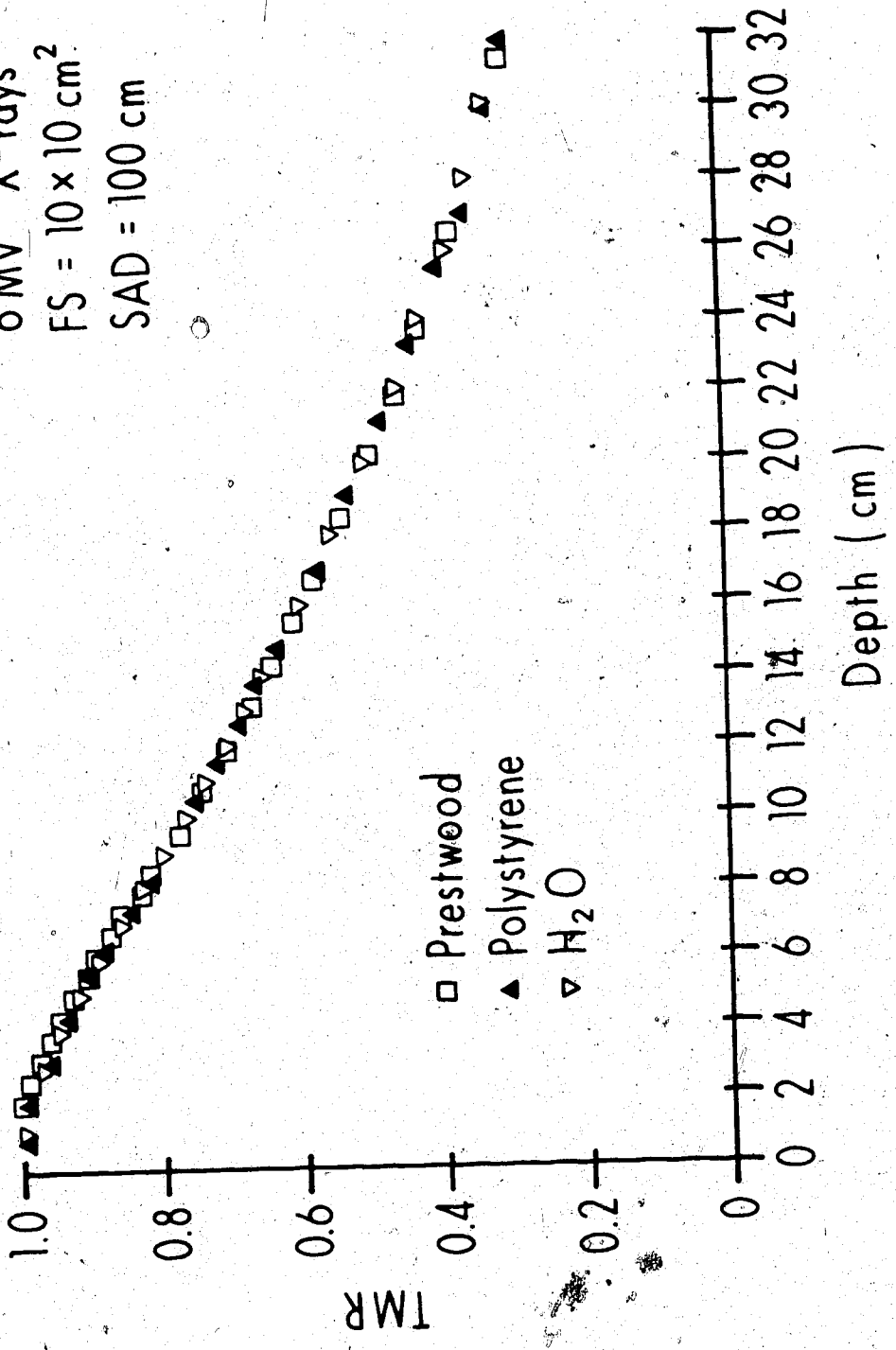
Fig. 3.9 Variation of tissue-maximum ratios with depth in a phantom.

The equivalence of these ratios for prestwood, polystyrene

and water is confirmed.

Distance) of 100 cm. Similar agreement is obtained for TMR's at the other field sizes.

(B) TMR's at extended distance

Several experiments were performed at larger distances from the source (SAD= 200 cm) to achieve the larger field size. The TMR's at this extended distance are within 1% of TMR's measured at the normal SAD of 100 cm (see Figure 3.10).

(C) Location of d_{max} at extended distance

For larger distances from the source, the position of the depth of maximum dose (d_{max}) in a phantom may be different than at an SAD of 100 cm (32). This is due to the different scattering conditions which contribute secondary electrons. Therefore the build-up to maximum dose was investigated for field sizes 10x10 cm^2 and 40x40 cm^2 in order to determine whether there is a shift in d_{max} at the larger SAD. The build-up curve was found to be reasonably uniform to within 0.5%, from a depth of 1.5 cm to 2.0 cm for both small and large fields. Therefore any value between 1.5 cm to 2.0 cm is acceptable as d_{max}, and shifts within this range are inconsequential.

Many of the dose calculation methods do not account for electronic disequilibrium in the medium. The range of electronic disequilibrium will be longer in a medium of lower density and the geometric location of d_{max} is expected to be deeper (143). In order to determine this
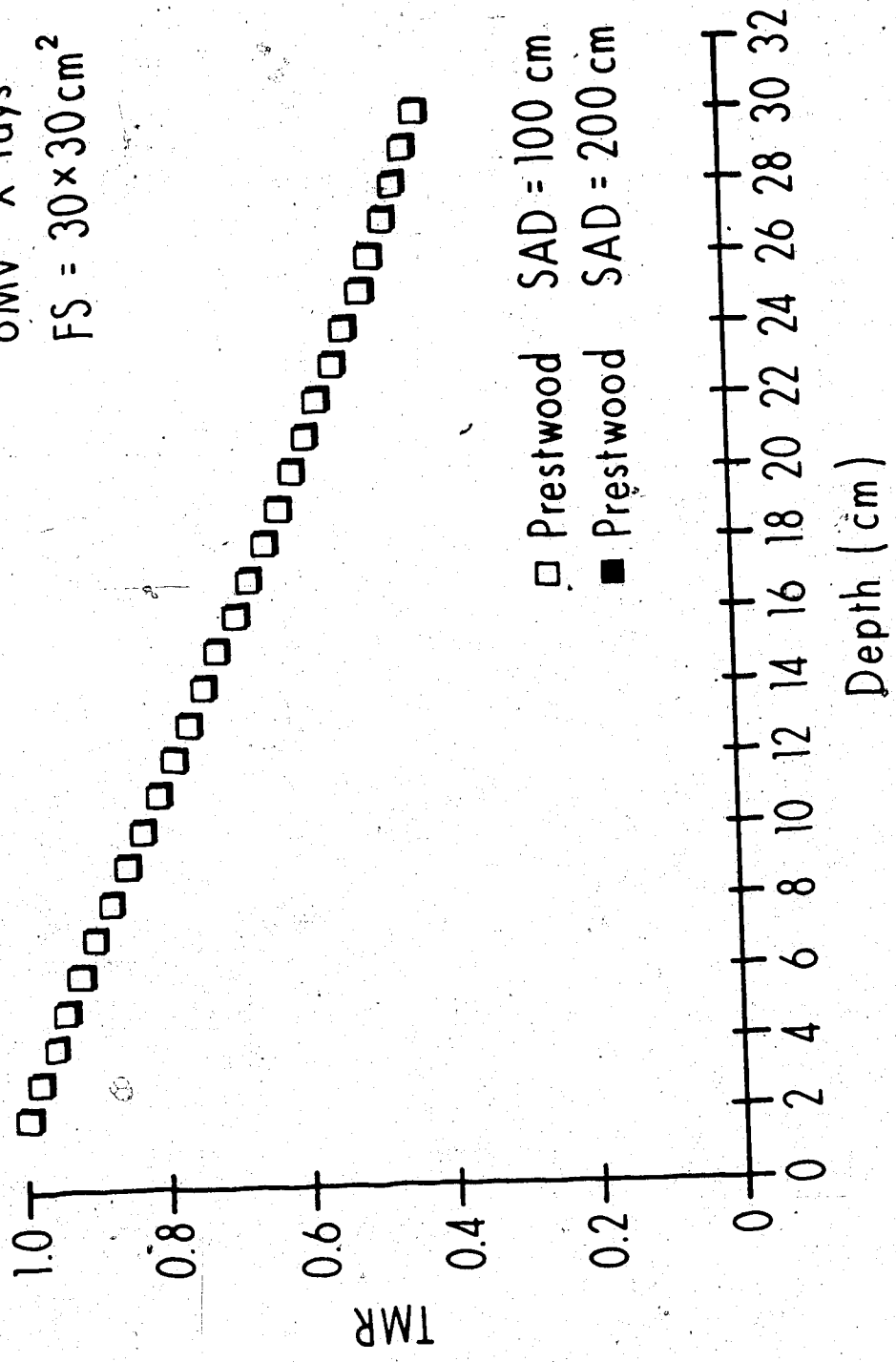
Fig. 3.10 Variation of tissue-maximum ratios with depth in a phantom.

The equivalence of these ratios at distances of 100 cm and

200 cm from the source is confirmed.

range for cork, the dose build-up was measured for field

sizes 10x10 cm² and 15x15 cm². For these measurements,

there was no build-up cap on the air ionization probe.

d_{max} for both fields was found to be 6.5 cm as shown in

Figure 3.11.

(D) Effect of backscattering material

The effect of material behind the measurement point

is often ignored in dose calculations, so that full

backscattering is implicitly assumed. The difference in

backscatter due to either cork or polystyrene behind the

probe was also investigated. Readings were obtained with

10.8 cm of either cork or polystyrene behind the probe for

several field sizes. The difference in backscatter was

found to be 1.3% for the 20x20 cm² field and less than 1%

for the smaller fields.
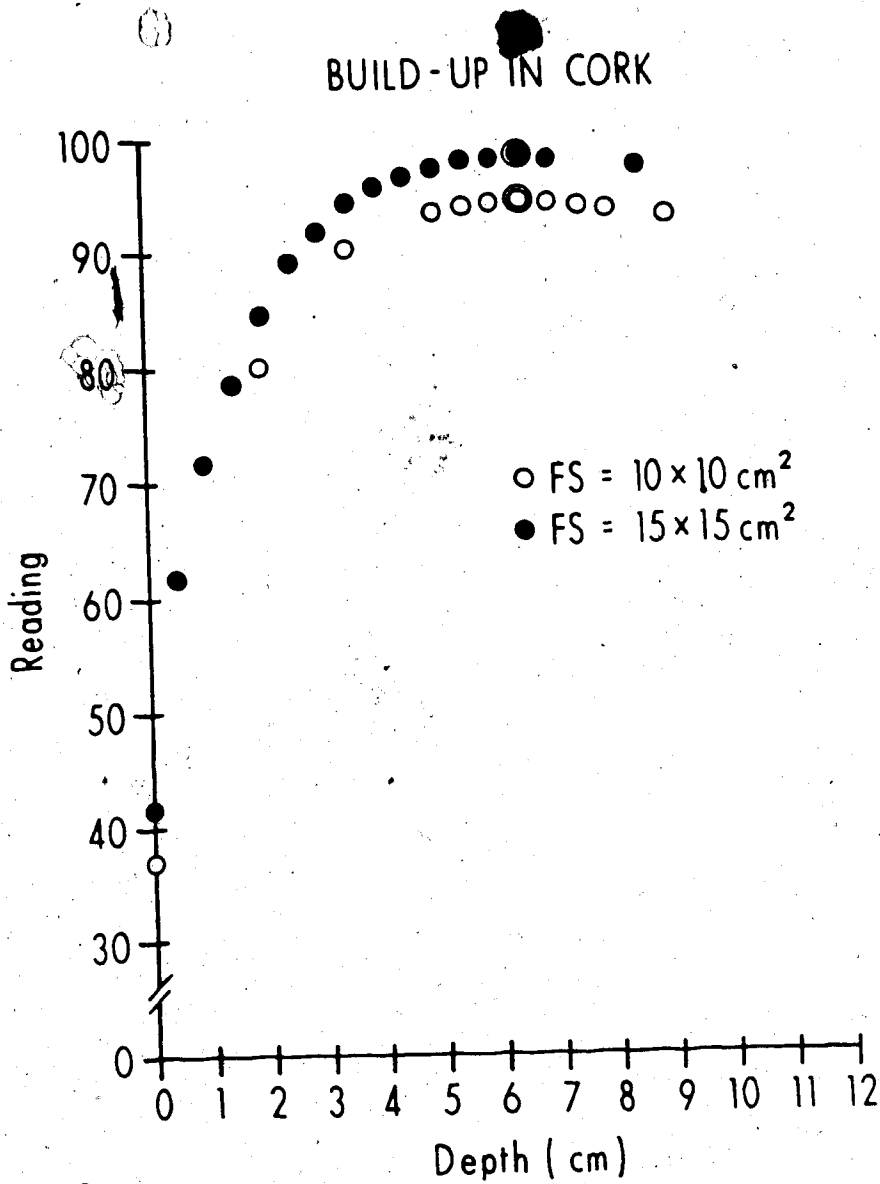
Fig. 3.11 The dose increase with depth in shallow layers
of cork. The depth of the maximum dose
(i.e. d_{max}) is at 6.5 cm for radiation field
sizes of 10x10 cm² and 15x15 cm².

3.4 Simple Heterogeneous Phantoms

Radiation doses were measured in simple heterogeneous phantoms irradiated with 6 MV X-rays and compared with those calculated using several algorithms implemented on radiotherapy planning computers. The Artronix PC-12 computer calculates inhomogeneity corrections using the effective SSD method. The AECL TP-11 computer uses the modified Batho method (109) to calculate tissue inhomogeneity corrections. Furthermore, dose calculations were also performed using the equivalent TAR method as implemented at the Ontario Cancer Institute. All these methods were described in section 3.2. Dose measurements were made with the Capintec PR-06C air ionization chamber described in section 3.1. The probe was used with build-up cap in polystyrene, while the build-up cap was removed for measurements in cork. The geometry of irradiation is shown in Figure 3.12. The probe is positioned at a fixed source-to-probe distance (SPD) along the central axis. The distance to the entrance side of the cork section, a, is increased, thus letting the entire cork section "rise through" the point of interest at P. Measurements were taken for different cork thicknesses, t, geometric depths, d, and field sizes, W_d, as listed in Table 3.6. These geometries were selected in order to sample the range of lung geometries encountered in clinical radiotherapy. For the larger field size an SAD of 200 cm was used. The inhomogeneity correction factor

is plotted versus parameter "a" as shown in Figure 3.12 both inside and beyond the cork inhomogeneity. Results are shown in this figure for field sizes 5x5 cm^2, 10x10 cm^2, and the large field of 35x35 cm^2 and cork thickness $t=7.8\pm0.2$ cm. Measured values are compared to ICF's calculated using the ratio of TAR's (effective SSD), generalized Batho, and equivalent TAR methods. From the experimental values one notes an initial sharp increase in the correction factor which then levels off. As the field size increases, the importance of scattered radiation

Table 3.6: Summary of experimental set-ups

Cork thickness	Geometric depth	Field size
3.2 cm	18.4 cm	5x5 cm^2
		10x10 cm^2
		20x20 cm^2
		35x35 cm^2
5.0 cm	15 cm	5x5 cm^2
		10x10 cm^2
		20x20 cm^2
		35x35 cm^2
7.8 cm	15.5 cm	5x5 cm^2
		10x10 cm^2
		20x20 cm^2
		35x35 cm^2

Experiment 'C'
6 MV X-rays
FS= 10×10 cm²

━━ measured
─·─ Ratio of TAR's
─── Eq TAR
━━ Batho

Inhomogeneity Correction
126
124
122
120
118
116
114
112
110
108
106
104
102
100
098
0 1 2 3 4 5 6 7 8 9 10 11 12 13 14 15 16
a(cm)

Experiment 'C'
6 MV X-rays
FS= 35×35 cm²

━━ measured
─·─ Ratio of TAR's
─── Eq TAR
━━ Batho

Inhomogeneity Correction
118
116
114
112
110
108
106
104
102
100
098
0 1 2 3 4 5 6 7 8 9 10 11 12 13 14 15 16
a(cm)

Experiment 'C'
6 MV X-rays
FS= 5×5 cm²

━━ measured
─·─ Ratio of TAR's
─── Eq TAR
━━ Batho

Inhomogeneity Correction
130
128
126
124
122
120
118
116
114
112
110
108
106
104
102
100
098
0 1 2 3 4 5 6 7 8 9 10 11 12 13 14 15 16
a(cm)

Polystyrene
Cork
Polystyrene

SPD
a
⊙P
w

Fig. 3.12 The inhomogeneity correction for 6 MV X-rays is plotted as a

function of parameter "a" for field size (A) 5x5 cm²,

(B) 10x10 cm², (C) 35x35 cm². The cork thickness, t, was 7.8±0.2 cm.

The experimental set-up is shown in the inset.

relative to the primary increases; but the inhomogeneity affects the primary radiation more than the scattered. For this reason, experimentally a greater ICF is observed for the smaller fields. For field sizes larger than 10x10 cm^2, the Batho correction factors agree more closely with the experimental values, presumably because the Batho correction indirectly (by use of TAR's which include the scatter) accounts in some way for the change in scattering conditions produced by the inhomogeneity. However, it underestimates the correction factor both inside and beyond cork by 2%. The ratio of TAR's overpredicts the correction factor in cork by as much as 8.2% near the cork polystyrene interface for the 10x10 cm^2 field. Beyond the cork polystyrene interface this method predicts a constant ICF which overpredicts the experimental values.

The equivalent TAR method performs better than the simple ratio of TAR's method, but is inferior to the Batho method in this geometry both within and beyond cork. It generally overpredicts the correction factor especially near the cork polystyrene interface where the overprediction is 2.6% for a 10x10 cm^2 field. This performance of the equivalent TAR method at 6 MV is not consistent with its reported superior performance at Cobalt-60. For Cobalt-60, agreement with the experimental data is within 2% both inside and beyond lung (107,110). The greater discrepancies for 6 MV X-rays are attributed to improper calculation of the contribution of scattered

radiation to dose. The weighting factors have little effect on the correction factors, but inaccuracies in scatter-air-ratios greatly affect the correction factors. The difficulty lies in obtaining "correct" zero-area tissue-air (or phantom) ratios. Practically these are found by extrapolation based on small field size data. This methodology (54) becomes difficult to apply for high energy X-rays because electron disequilibrium develops for smaller fields.

These experiments at 6 MV support the suggestion by Henkelman and Wong (43) that pixel-by-pixel methods which treat scatter contributions from scattering elements independently, may be inferior to simpler methods which use a bulk correction for tissue inhomogeneity.

For the smaller field size of 5x5 cm^2, the ratio of TAR's (effective SSD) method as well as the equivalent TAR method, overpredict correction factors both within and beyond cork. The Batho method again gives the best agreement, but exhibits some irregularities. The correction factor is now overpredicted in lung, and the curve of calculated correction factors crosses the experimental curve shortly behind the interface and underpredicts the correction factors thereafter. The correction factors in lung thus are overpredicted by all correction methods to a greater extent than expected. For the smaller fields incident on low density materials there is loss of lateral electron transport (i.e. more

electrons leave the central region tha enter from the sides) (143). Therefore a decrease in dose, and a decrease in the correction factor occurs. This effect becomes more pronounced with higher energy X-rays and is not handled by the correction methods discussed here. The above experiments were repeated for 15 MV X-rays and are included in a paper to be submitted for publication; the effects of electron disequilibrium are investigated in detail at this energy.

When the depth d is less than the depth of maximum build-up in tissue, the condition of electronic equilibrium of the Batho method is violated. If it is used with TMR's measured in the build-up region, the correction factors so calculated give very anomalous results. Therefore care must be taken when correction factors are calculated in the initial build-up region or at the interface of two media. For 6 MV X-rays this region extends over 1.5 cm near the interface. For higher energy beams, there is a greater distance in which the Batho correction should not be applied.

The 5 cm cork-10 cm polystyrene combination shows similar trends as shown in Figure 3.12, except that in this case, the equivalent TAR method slightly underpredicts correction factors beyond cork.

For the 3 cm cork-15 cm polystyrene combination the measured and calculated correction factors are shown in Figure 3.13. The Batho correction gives the best
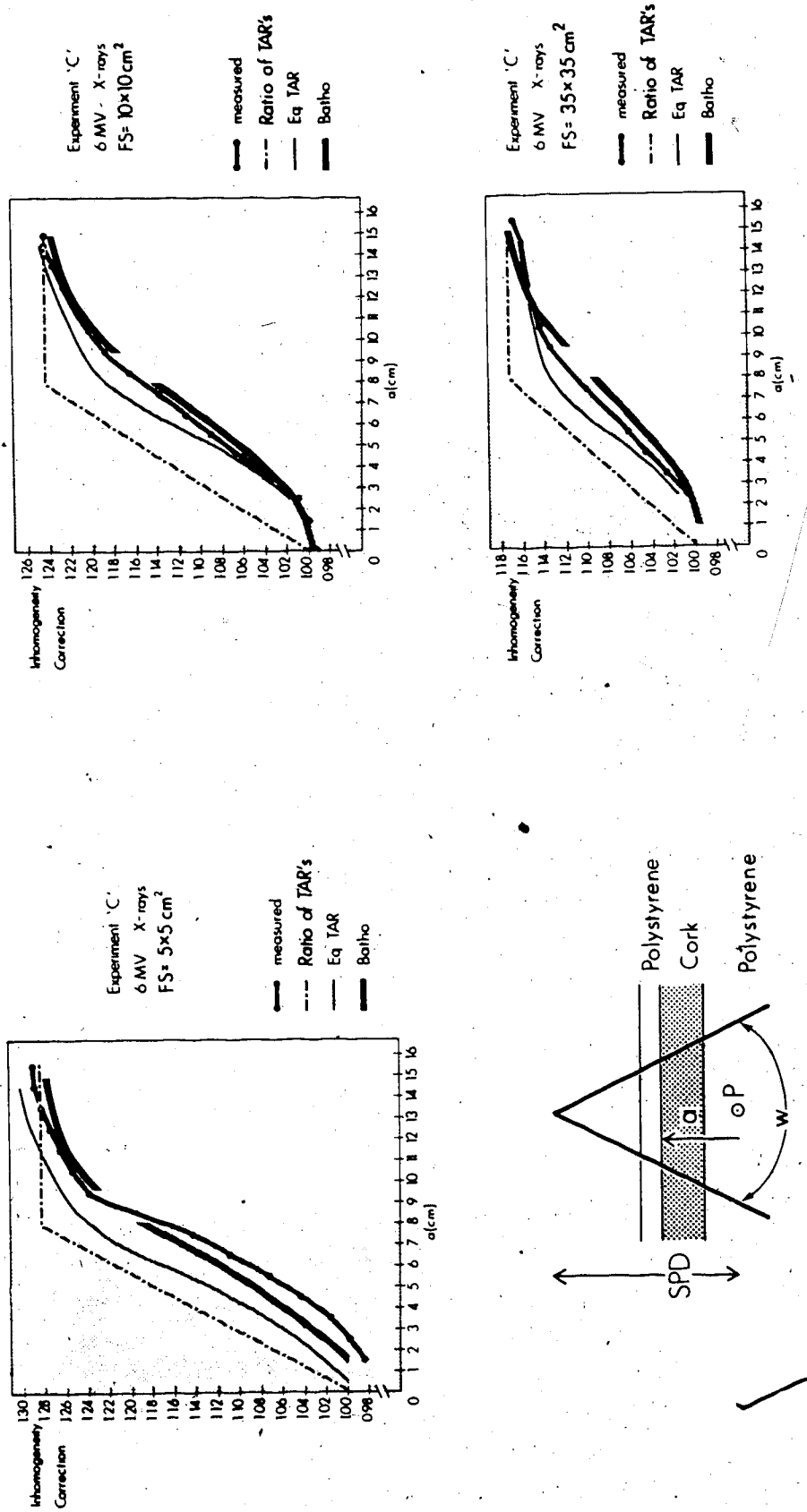
Fig. 3.13 The inhomogeneity correction for 6 MV X-rays is plotted as a function of parameter "a" for field size (A) 5x5 cm², (B) 10x10 cm², (C) 35x35 cm². The cork thickness, t, was 3.2 cm.

6MV X-rays
FS = 10×10 cm²

Inhomogeneity Correction

a(cm)

6MV X-rays
FS = 35×35 cm²

Inhomogeneity Correction

a(cm)

6MV X-rays
FS = 5×5 cm²

Inhomogeneity Correction

a(cm)

—— measured
––– Ratio of TAR's
—— Eq. TAR
▬▬ Batho

Polystyrene
Cork
Polystyrene

SPD

a

⊙P

w
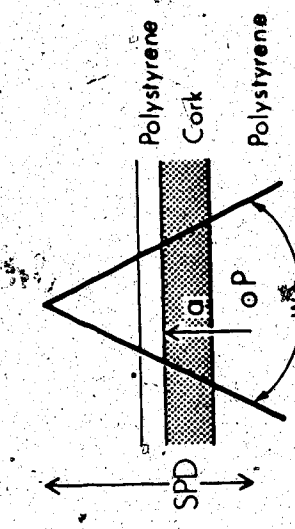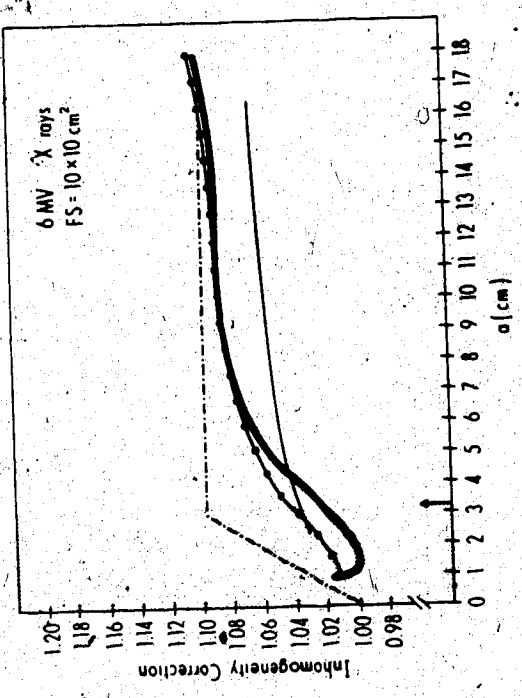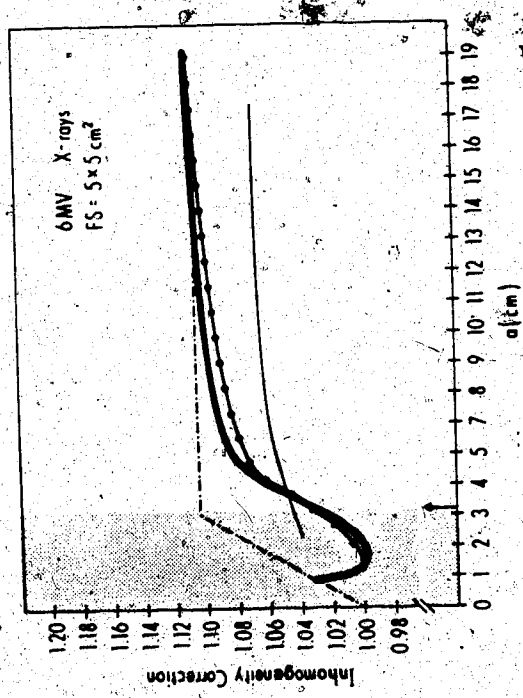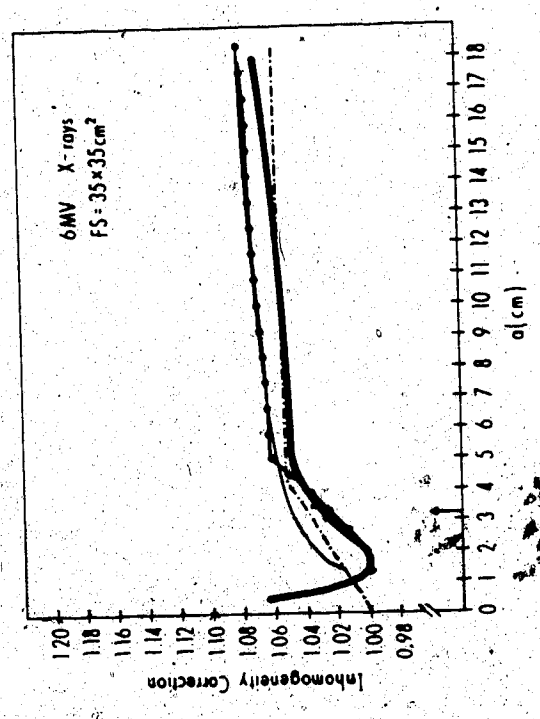
agreement both within and beyond cork. A slight underprediction occurs in cork for field sizes 10×10 cm² and beyond. A slight overprediction occurs for the 5×5 cm field size. The equivalent TAR method overpredicts doses in lung by roughly 2.5%, crosses over near the interface and underpredicts the doses beyond cork by 2.5% for the smaller field sizes. This handling of the correction factor beyond cork by the equivalent TAR method is not self-consistent with results obtained for other cork thicknesses. For example, it overpredicts the effect for a thicker cork section by overestimating correction factors beyond (Figure 3.12), but underpredicts the effect for a smaller thickness of cork by underestimating correction factors beyond (Figure 3.13). The agreement of the ratio of TAR's calculated correction factors with the measured values is not better than with the other combinations of cork-polystyrene.

Similar cork-polystyrene combinations were used to measure correction factors at an SAD of 200 cm and for field sizes up to 60×60 cm². There is not much change in the measured and calculated correction factors from field size 35×35 cm² to 60×60 cm². This is expected since the TMR curve versus field size changes little beyond a 35×35 cm² field. In addition a 10 cm cork-5 cm prestwood combination was also used. The correction factors for this combination and a large field size of 50×50 cm² are shown in Figure 3.16 of section 3.5.

The Batho correction performed very well giving values within 2% both within and beyond cork. This is contrary to what would be expected based on similar experiments performed at Cobalt-60 (125,139) where the Batho correction underpredicted dose in lung by as much as 10% in large fields. The effective energy of the 6 MV X-ray beam (2 MeV) is not greatly different from the monoenergetic photon emissions of 1.17 and 1.33 MeV of a Cobalt-60 beam. Therefore the improvement for in-lung dose calculations at large fields cannot be due to the difference in beam "quality". In order to explain this unexpected good performance of the Batho correction, experiments were performed with Cobalt-60 radiation. This is analysed in detail in section 3.5, which consists of a paper to be published in Medical Physics (May/June 1984).

3.5 Improved Lung Dose Calculations Using TMR'S

(vs. TAR'S) in the Batho Correction

INTRODUCTION

Dose calculations are usually performed by first considering the patient as being composed uniformly of water and then applying a correction to account for non unit-density structures, such as lung. With computed tomographic (CT) scanning, the _in-vivo_ geometry and density of the lung can be accurately determined, resulting in improved accuracy of calcul........(108). The availability of such anatomical ......ion ...s prompted a re-evaluation of the accuracy ... calculations within heterogeneous tis.....).

The power law ti...... ratio (TAR) method was developed initially fo... culating dose at points lying in the "shadow" of wide lung irradiated with Cobalt-60 photons (7,142). It has since been refined to consider dose points within lung (109), and ... account for lungs of finite width (69). Application of the method to higher photon energies has been attempted (113). A theoretical analysis of the Batho expression has recently been reported (70,139), but most validations have been experimental, as summarized in Table 3.7.

According to Sontag (109), the Batho correction for the simple geometry shown in Figure 3.14 is:

$$CF_B(TAR) = [\frac{TAR(d_2,r)}{TAR(d_1,r)}]^{1-\rho_2} \qquad -1A$$

Table 3.7: Experimental tests of the Batho correction
for Cobalt-60 irradiation

Reference	Field Size	Phantom	Agreement beyond lung	within lung
Sontag & Cunningham (109)	5x5 cm² to 15x15 cm²	wide slabs	+3%	-3%
Tatcher & Palti (113)	5x5 cm² to 15x15 cm²	slabs	+2%	-2%
Webb & Fox (133)	10x10 cm²	wide slabs	?+2%	-2%
Wong & Henkelman (139)	10x10 cm²	wide slabs	-	-2%
	20x20 cm²	wide slabs	-2%	-6%
Van Dyk et al. (125)	50x60 cm²	humanoid		-10%
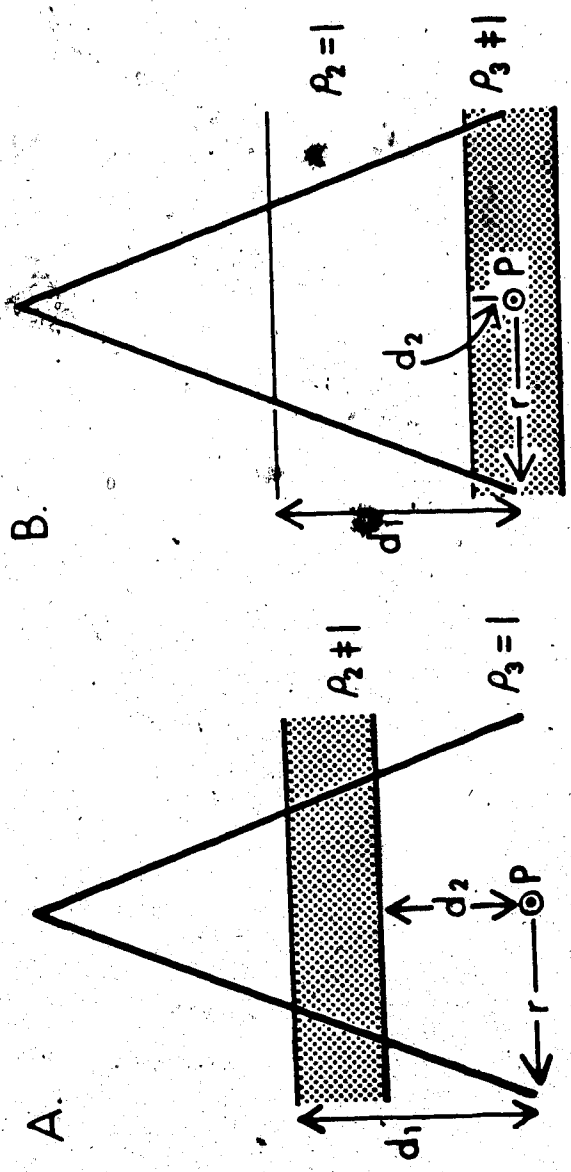
Fig. 3.14 Geometry for the Batho correction. Dose is calculated at point P,

(A) when P lies in tissue beyond lung, (B) when P lies within lung.

for points beyond lung, and

$$CF_B(TAR) = [\ TAR(d_2,r)\ ]^{\rho_3-1}$$ 1B

for points within lung.

where:

$TAR(d_i,r)$ is the tissue-air ratio at depth d_i and for field size r at depth d_i,

ρ_2, ρ_3 are the electron densities (e/cm^3) of the two media, relative to water.

These expressions assume that

(a) the lateral extent of the inhomogeneity is larger than the incident radiation beam,

(b) electronic equilibrium exists at the dose points of interest. The equation only corrects for changes in photon fluences and ignores the finite range of electrons set in motion. This creates difficulties in extending the Batho method to higher photon energies such as 10 MV X-rays (143).

(c) the tissue is water-like in its energy absorption and properties,

(d) changes in backscattering from materials beyond the point of interest are negligible.

Despite these shortcomings, the method continues to be used clinically with (or without !) adjustments for situations in which the above assumptions are untenable.

As seen in Table 3.7, the Batho correction factor is

accurate to within 3% inside and beyond lung for Cobalt-60 irradiation with field sizes up to 15x15 cm². However, as the field size is increased, the accuracy degrades and the Batho correction underpredicts the dose within lung by as much as 10% for fields used in half-body irradiation (25). The proposed explanation is that scattered radiation plays a greater role at large fields, and the Batho-TAR method fails to account correctly for this component of dose.

In our study with 6 MV X-rays, TMR (tissue-maximum ratios) were substituted in the Batho correction and we found agreement to within 2% both inside and beyond lung for field sizes up to 50x50 cm². In order to investigate whether the use of TMR's instead of TAR's accounted for the improvement in accuracy at the larger fields, we performed experiments with Cobalt-60 irradiation and used both TAR's and TMR's which are both easily measured at this energy. Experiments confirmed a significant improvement by 5% in accuracy when TMR's were used for in-lung corrections for all field sizes up to 50x50 cm². Tables of measured TMR data for Cobalt-60 are reported in section III.

The theoretical analysis of the improved performance of the TMR-Batho correction is presented in analytic calculations of primary and singly-scattered radiation in section IV.

II. EXPERIMENTAL METHODS

Doses were measured in heterogeneous phantoms consisting of slabs of cork to simulate lung and of polystyrene or prestwood to simulate unit density tissue. The electron densities of these materials was determined by computed tomography to be 0.28, 0.32, 1.01, and 1.02 respectively, relative to water. The phantoms were irradiated with 6 MV X-rays[a] and Cobalt-60 γ-rays[b]. Dose measurements were made with an air ionization chamber with an active volume of 0.65 ml, connected to a calibrated electrometer[c]. Measurements in polystyrene and prestwood were obtained with a standard "build-up cap" (0.5 cm of lucite), while in cork, the build-up cap was purposely removed in order to observe the effects of electronic disequilibrium. Under these circumstances the diameter of the air cavity was 6 mm, with a plastic wall thickness of only 0.5 mm.

The geometry of the irradiation is shown in Figure 3.15. The probe is positioned at a fixed source-to-probe (SPD) distance along the central axis. For small field sizes up to 20x20 cm² the SPD was 100 cm for 6 MV and 80 cm for Cobalt-60 radiations; the SPD was increased to 200 cm for 6 MV and 165.5 cm for Cobalt-60 radiations to achieve larger fields. The independence of TMR values on

a) Siemens Mevatron VI linear accelerator
b) Theratron 80 and Theratron 780 (Atomic Energy of Canada)
c) Capintec PR06C chamber and Model 192A electrometer
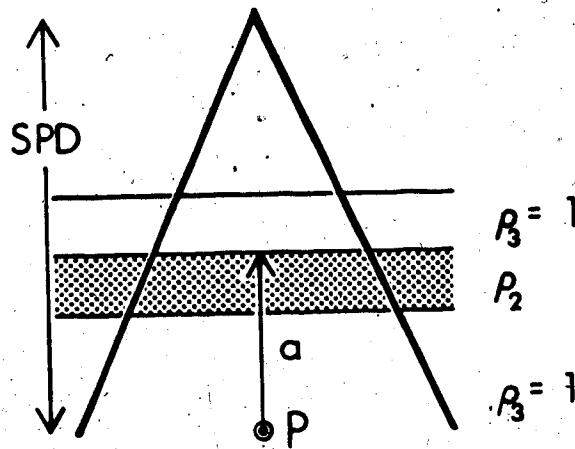
Fig. 3.15 Geometry used to obtain the experimental data. Dose at P is measured as parameter "a" is varied from 1 to 15 cm.

SPD was validated to within 1%. The major variable in our experiment is the distance to the entrance side of the cork slab, a. The results are most easily interpreted by considering that the cork slab effectively rises through the measurement point P, thus allowing validation of both equations 1A and 1B for isocentric irradiations.

For all field sizes, the phantom was larger than the field in order to satisfy assumption (a) of the Bath equation. Assumption (b) is generally valid, except for transition points near the tissue interfaces. Assumption (c) is valid to within 1% for soft tissues and lung at megavoltage energies (54). The energy absorption properties of polystyrene and prestwood, the materials used in the experiments, were found to be similar to those of water (54). Assumption (d) is approximately valid for our experiments since the reduction in backscatter produced when cork was substituted for polystyrene behind the probe was measured and found to be less than 2%.

III. EXPERIMENTAL RESULTS

Measurements were made at a constant depth of 15 cm along the central axis below the entrance surface of the phantom. A cork thickness of 10 cm was used to simulate lung of typical thickness. Results were obtained for a small (5x5 cm^2), medium (10x10 cm^2), and large field (50x50 cm^2). The data expressed as "inhomogeneity correction factors" (21) for 6 MV X-rays are shown in

Figure 3.16 A,B,C. The inhomogeneity correction factor is plotted as a function of a, the distance between the measurement point and the "top" cork-polystyrene interface (see Figure 3.15). The discrepancy between measured and calculated doses within and beyond lung is approximately 2% for small as well as large fields. This is contrary to expectations based on the results) of Van Dyk for irradiations with large Cobalt-60 fields (125).

Similar results for Cobalt-60 are shown in Figure 3.17 A,B,C. The calculated Batho correction factor using the usual TAR values and the proposed TMR values are also shown for comparison. For points beyond cork, there is no difference between the two correction factors calculated using either TAR's or TMR's, as expected from their invariant ratio in equation 1A. The maximum deviation of the calculated correction factor from measured values is 3%. However, for points inside cork there is a marked difference between the TMR-Batho correction and the TAR-Batho correction. The deviation from measured values is consistently worse for the TAR-Batho correction, and can be as high as 9% for large fields. This poor performance of the TAR-Batho correction at large fields has already been documented (125), but the simple remedy of using the TMR-Batho correction has not been reported previously. Nevertheless, it has been noted by K.Yuen (private communication) that for Cobalt-60 radiation, an in-lung correction factor of the form

A. 5×5 cm² 100 cm SPD

Inhomogeneity Correction Factor

1.38 1.34 1.30 1.26 1.22 1.18 1.14 1.10 1.06 1.02 0.98

Cork Polystyrene

Parameter a (cm)

1 2 3 4 5 6 7 8 9 10 11 12 13 14 15

B. 10×10 cm² 100 cm SPD

Inhomogeneity Correction Factor

1.30 1.26 1.22 1.18 1.14 1.10 1.06 1.02 0.98

Cork Polystyrene

Parameter a (cm)

1 2 3 4 5 6 7 8 9 10 11 12 13 14 15

C. 50×50 cm² 200 cm SPD

Inhomogeneity Correction Factor

1.22 1.18 1.14 1.10 1.06 1.02 0.98

Cork Prestwood

Parameter a (cm)

1 2 3 4 5 6 7 8 9 10 11 12 13 14 15

● ICF measured

▲ ICF (Batho·TMR)

Polystyrene
Cork
Polystyrene

SPD

a

oP

Fig. 3.16 For 6 MV X-rays, the inhomogeneity correction factor is plotted as a function of parameter "a" for field size (A) 5x5 cm², (B) 10x10 cm², (C) 50x50 cm².
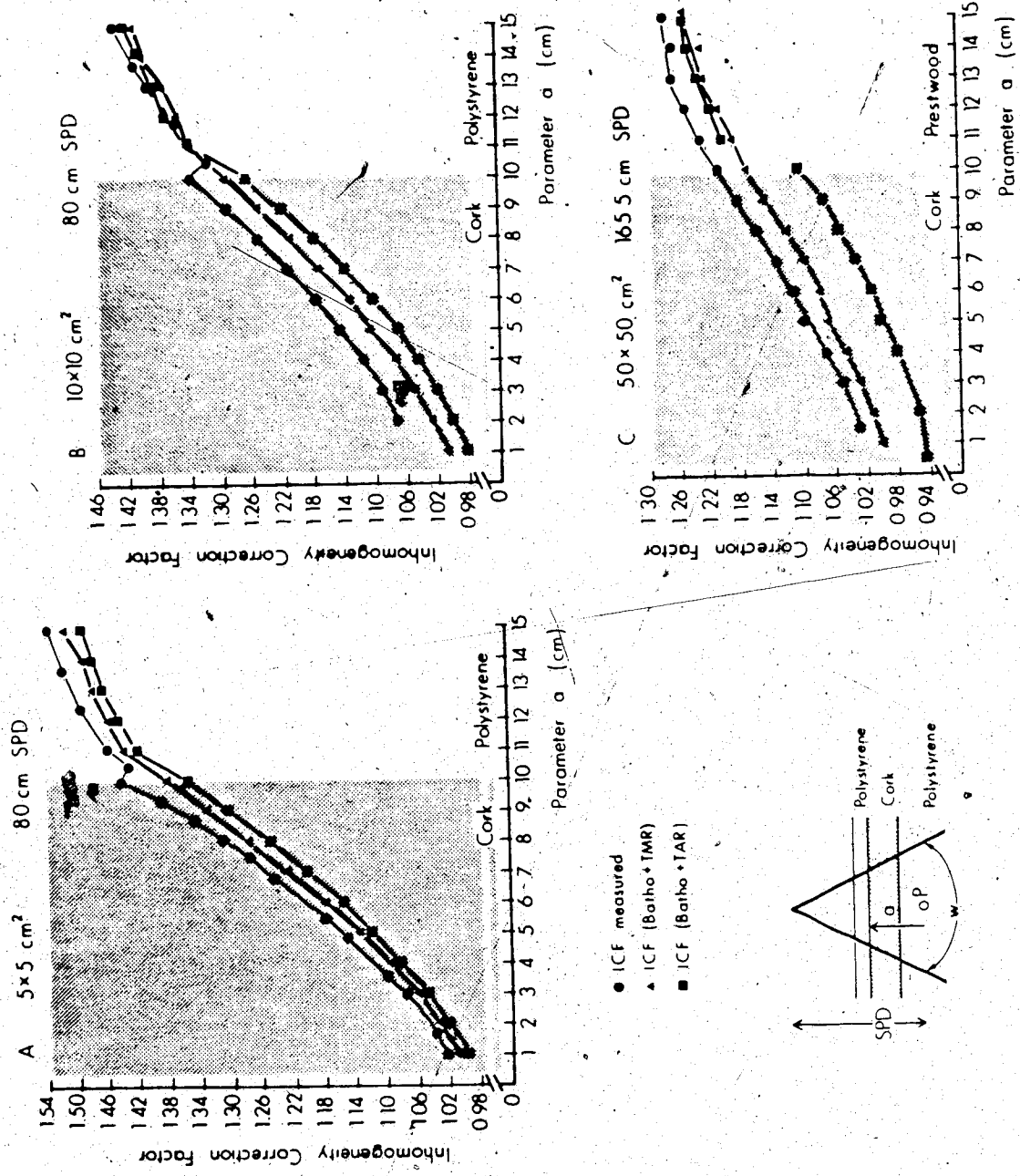
Fig. 3.17 For Cobalt-60 irradiation, the inhomogeneity correction factor is plotted as a function of parameter "a" for field size (A) 5x5 cm², (B) 10x10 cm², (C) 50x50 cm².

$$[\text{ TAR}(d) / \text{TAR}(0.5 \text{ cm})]^{\rho-1} \times \text{MSF}$$

would give better agreement with experimental values. The reason given was that TAR(0.5cm) and MSF (missing scatter factor) correct for changes in scatter behind the measurement point.

The reasons for the better results observed with the TMR-Batho method will now be examined. Note that the original Batho correction was NOT intended for use with TMR values which are suggested for higher energy X-rays (46,58). However, many clinics have (blindly) adopted the Batho correction using TMR values for both manual and computer-aided radiotherapy planning.

For the reader's convenience, tables of Cobalt-60 TMR values for field sizes 5x5 cm^2 to 50x50 cm^2, measured on a Theratron 80+ and Theratron 780+ are provided. TMR values as measured on both units for small and large field sizes were identical to within 1%. Comparing our measured TMR's with those calculated from published TAR's, we find similar agreement for the smaller field sizes (54) and the larger field size (130) for depths up to 20 cm. Differences are attributed to variations in the Cobalt source and collimator (131), and the experimental difficulties in measuring D_a for large fields (130),

+ Atomic Energy of Canada

Table 3.8: Tissue-maximum ratios for Cobalt-60

Depth(cm)	Field size						
	$5\times5\,cm^2$	$10\times10\,cm^2$	$15\times15\,cm^2$	$20\times20\,cm^2$	$30\times30\,cm^2$	$40\times40\,cm^2$	$50\times50\,cm^2$
0.5	1.0	1.0	1.0	1.0	1.0	1.0	1.0
1.0	0.990	0.990	0.992	0.990	0.994	0.995	0.995
2.0	0.953	0.960	0.970	0.970	0.978	0.980	0.980
3.0	0.915	0.930	0.942	0.945	0.956	0.960	0.960
4.0	0.872	0.900	0.912	0.917	0.935	0.940	0.941
5.0	0.831	0.864	0.882	0.890	0.912	0.915	0.925
6.0	0.785	0.830	0.847	0.860	0.888	0.895	0.900
7.0	0.741	0.790	0.813	0.825	0.861	0.870	0.875
8.0	0.699	0.755	0.780	0.795	0.835	0.841	0.855
9.0	0.657	0.720	0.750	0.760	0.810	0.815	0.825
10.0	0.622	0.685	0.717	0.733	0.780	0.790	0.800
11.0	0.581	0.645	0.684	0.710	0.753	0.760	0.780
12.0	0.548	0.615	0.650	0.681	0.725	0.731	0.750
13.0	0.516	0.585	0.618	0.650	0.695	0.708	0.720
14.0	0.486	0.550	0.588	0.620	0.662	0.680	0.700
15.0	0.455	0.520	0.560	0.595	0.635	0.655	0.674
16.0	0.427	0.491	0.530	0.562	0.607	0.630	0.649
17.0	0.400	0.468	0.501	0.535	0.582	0.617	0.623
18.0	0.373	0.441	0.475	0.510	0.557	0.585	0.599
19.0	0.349	0.414	0.451	0.483	0.532	0.560	0.579
20.0	0.329	0.390	0.429	0.455	0.508	0.538	0.552
21.0	0.310	0.365	0.405	0.431	0.486	0.515	0.530
22.0	0.291	0.340	0.382	0.410	0.461	0.495	0.510
23.0	0.275	0.322	0.360	0.389	0.443	0.471	0.490
24.0	0.253	0.305	0.340	0.369	0.422	0.450	0.468
25.0	0.240	0.285	0.320	0.349	0.404	0.430	0.450
26.0	0.224	0.265	0.302	0.331	0.385	0.412	0.435
27.0	0.210	0.241	0.285	0.314	0.364	0.395	0.418
28.0	0.199	0.220	0.270	0.299	0.348	0.380	0.399
29.0	0.189	0.210	0.257	0.281	0.330	0.360	0.380
30.0	0.175	0.205	0.241	0.265	0.316	0.341	0.367

where D_A is the dose to a small isolated mass of tissue in air. We are thus using a consistent set of TAR and TMR data in our calculation of Batho correction factors.

IV. THEORETICAL CALCULATIONS

In order to explain the unexpected performance of the TMR-Batho method, we analysed how the Batho method approximates the dose in an inhomogeneous medium. For comparison, we also calculated the dose due to primary and singly-scattered photons analytically (139). For Cobalt-60 radiation, the dose due to primary and singly-scattered radiation accounts for 93% of the total dose at a depth of 10 cm in water and a large field of 10 cm radius (140); consideration of only the primary and first-scatter components thus yields a reasonable estimate of the structure of the solution. Consideration of higher order scattering is possible to second order (140), but beyond this an analytic solution is intractable (for a finite heterogeneous medium). The application of Monte Carlo technique is possible, although time-consuming (133). However, this approach does not yield a structured solution which can be compared term-by-term with the Batho equation. The latter is important if the implicit limitations of the Batho approach are to be identified and understood more clearly.

A. Analytic Calculation

The total dose at P is decomposed into

$D_A = D_0 + D_1 + D_2 + \ldots\ldots + D_n$

where D_i = component of dose due to photons which have scattered "i" times prior to interacting at P. In the following derivation, we only solve for D_0 and D_1.

Assuming monoenergetic photons of energy E_0 incident on a homogeneous medium, and electronic equilibrium at point P (see Figure 3.18), the dose due to primary radiation is trivially:

$$D_0 = \Phi_0 \, e^{-\mu_0 d} \, \left(\frac{\mu_{en}}{\rho}\right) E_0 \qquad\qquad (1)$$

where d = depth in phantom (cm)

Φ_0 = incident photon number fluence (photons/cm^2)

(μ_{en}/ρ) = mass energy absorption coefficient (cm^2/g)

μ_0 = linear attenuation coefficient (cm^{-1}) for the medium at photon energy E_0 (MeV).

The dose at P, due to single scattering at elemental volume Q also assuming electronic equilibrium, is:

$$D_1 = \Phi_0 \, e^{-\mu_0(d - r\cos\theta)} \, \frac{d\sigma}{d\Omega} \, \frac{dA_p}{r^2} \, n_e \, dV \, e^{-\mu_1 r} \left(\frac{\mu_{en}}{\rho}\right)_1 \frac{E_1}{dA_p} \qquad (2)$$

where: $\dfrac{d\sigma}{d\Omega}$ = differential Compton cross section per unit solid angle (cm^2/e)

E_1 = once scattered photon energy (MeV)

n_e = electron density (e/cm^3) of medium

179
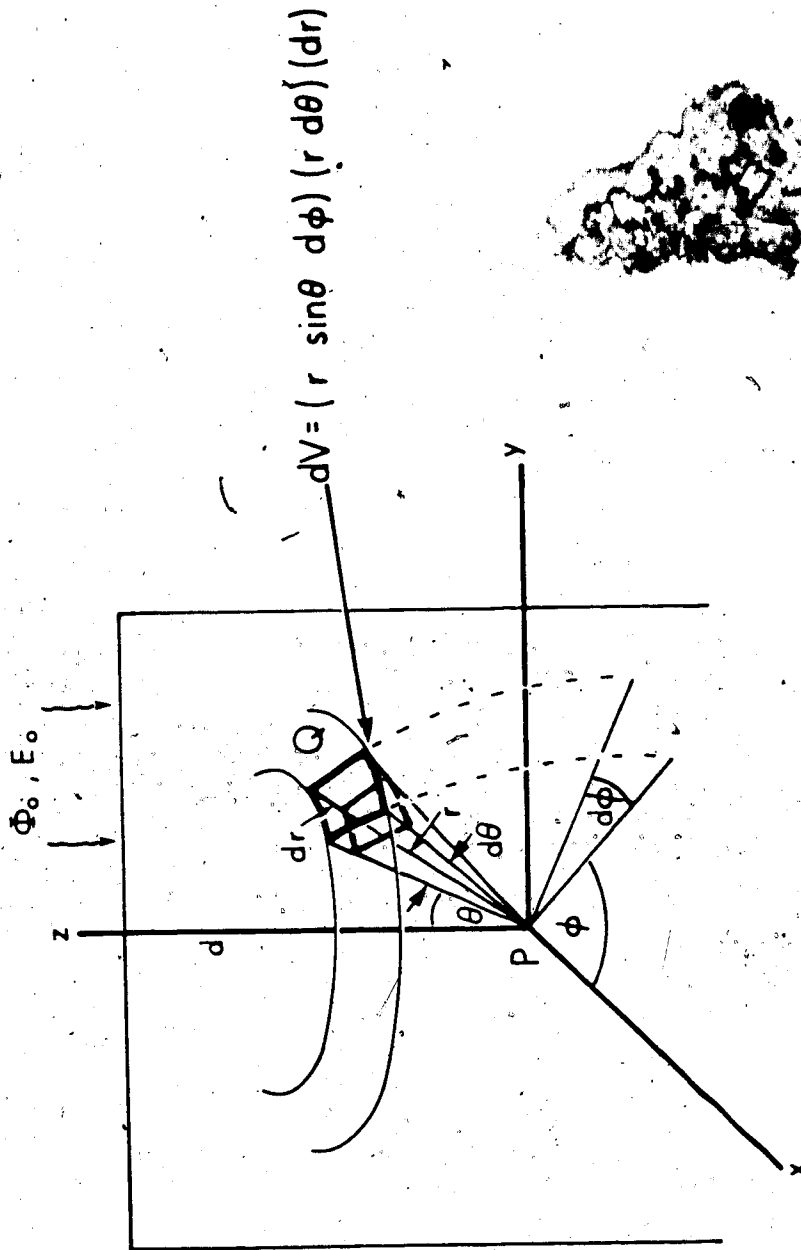
Fig. 3.18 Spherical coordinate system used for calculation of D_0 and D_A. Photons are scattered once at Q towards point P.

$$(\mu_{en}/\rho) = \text{mass energy absorption coefficient for}$$
$$\text{once-scattered photons (cm}^2/\text{g)}$$
$$\mu_1 = \text{linear attenuation coefficient (cm}^{-1})$$
$$\text{for first-scattered photons}$$
$$dA_p = \text{element of area at P.}$$

Assuming a parallel circular radiation field, and a spherical coordinate system, the total first scatter dose at P from all surrounding elements rearranges as:

$$D_1 = 2\pi n_e \, \Phi_0 e^{-\mu_0 d} \int_0^\pi \int_0^{r_m} E_1 \left(\frac{\mu_{en}}{\rho}\right)_1 \sin\theta \, \frac{d\sigma}{d\Omega} \, e^{r(\mu_0 \cos\theta - \mu_1)} \, dr \, d\theta$$

where: r_m = maximum radial distance from P to the geometric edge of beam, or, integrating over r,

$$D_1 = 2\pi n_e \, \Phi_0 e^{-\mu_0 d} \int_0^\pi E_1 \left(\frac{\mu_{en}}{\rho}\right)_1 \sin\theta \, \frac{d\sigma}{d\Omega} \, \frac{(e^{r_m(\mu_0 \cos\theta - \mu_1)} - 1)}{(\mu_0 \cos\theta - \mu_1)} \, d\theta \qquad (3)$$

Consider now the homogeneous phantom as two separate layers of water equivalent material as shown in Figure 3.19, in order to calculate separate scatter contributions. The first-scatter dose D_1 reaching point P can be divided into two parts; $D_{1w}^I(d_1)$ is the first-scatter dose at P originating in layer I, $D_{1w}^{II}(d_1)$ is the first-scatter dose at P originating in layer II. Then, restriction of the limits of integration to within layers I and II yields:
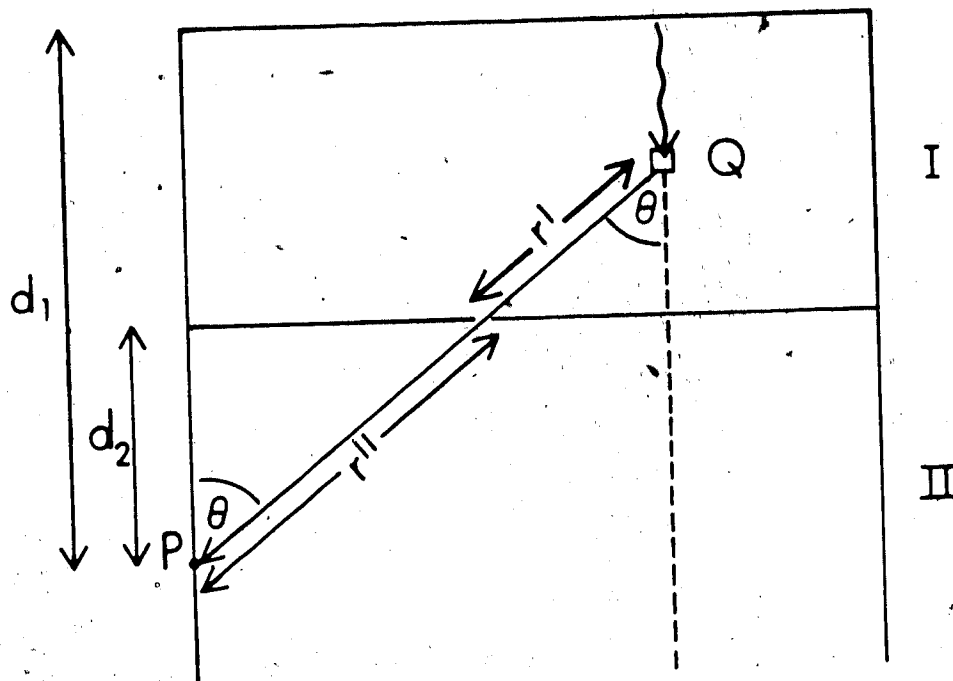
Fig. 3.19 Geometry used for calculation of first-scatter

dose to point P from two separate layers I and II.

$$D_{1w}^{I}(d_1) = 2\pi n_{ew}\, \phi_0\, e^{-\mu_0(d_1-d_2)} \int_0^{\theta_{max}} E_1\left(\frac{\mu_{en}}{\rho}\right)_1 \sin\theta\, \frac{d\sigma}{d\Omega}\, e^{-(\mu_1 d_2/\cos\theta)}$$

$$\cdots\cdots \frac{(e^{r_m^{I}(\mu_0\cos\theta - \mu_1)} - 1)}{(\mu_0\cos\theta - \mu_1)}\, d\theta \qquad (4)$$

where r_m^{I} = maximum distance to the edge of region I

$$D_{1w}^{II}(d_1) = 2\pi n_{ew}\phi_0\, e^{-\mu_0 d_1} \int_0^{\pi} E_1\left(\frac{\mu_{en}}{\rho}\right)_1 \sin\theta\, \frac{d\sigma}{d\Omega}\, \frac{(e^{r_m^{II}(\mu_0\cos\theta - \mu_1)} - 1)}{(\mu_0\cos\theta - \mu_1)}\, d\theta \qquad (5)$$

where r_m^{II} = maximum distance from P to the edge of region
II.

For comparison with the dose calculated by the Batho
method, we also require an expression for the scatter
contribution from the second layer when the first layer is
removed:

$$D_{1w}(d_2) = 2\pi n_{ew}\, \phi_0 e^{-\mu_0 d_2} \int_0^{\pi} E_1\left(\frac{\mu_{en}}{\rho}\right)_1 \sin\theta\, \frac{d\sigma}{d\Omega}\, \frac{(e^{r_m^{II}(\mu_0\cos\theta - \mu_1)} - 1)}{(\mu_0\cos\theta - \mu_1)} d\theta \qquad (6)$$

Suppose now the two layers are replaced by two
different layers of electron densities (ρ_2) and (ρ_3),
relative to water as in Figure 3.14. Then, in the
expressions (4) and (5) for first-scatter dose, all
distances in the layers must be scaled by the relative
electron density appropriate for each layer (80).
Therefore, the first-scatter dose at P originating in

layer I of density ρ_2 is:

$$D_1^I(d_1) = 2\pi n_{eI}\; \Phi_0 e^{-\mu_0\rho_2(d_1-d_2)} \int_0^{\theta_{max}} E_1(\frac{\mu_{en}}{\rho})_1 \sin\theta\; \frac{d\sigma}{d\Omega}\; e^{-(\mu_1\rho_3 d_2/\cos\theta)} \quad \cdots\cdots$$

$$\cdots\cdots \frac{(e^{\rho_2 r_m^I(\mu_0\cos\theta - \mu_1)} - 1)}{(\mu_0\cos\theta - \mu_1)} d\theta \qquad (7)$$

and first scatter dose at P originating in layer II of density ρ_3 is:

$$D_1^{II}(d_1) = 2\pi n_{eII}\; \Phi_0 e^{-\mu_0[\rho_2(d_1-d_2)+\rho_3 d_2]} \int_0^{\pi} E_1(\frac{\mu_{en}}{\rho})_1 \sin\theta \frac{d\sigma}{d\Omega}\quad \cdots\cdots$$

$$\cdots\cdots \frac{(e^{\rho_3 r_m^{II}(\mu_0\cos\theta - \mu_1)} - 1)}{(\mu_0\cos\theta - \mu_1)}\; d\theta \qquad (8)$$

In order to express $D_1^{II}(d_1)$ in terms of the dose in water, $D_{1w}^{II}(d_1)$, we use a Taylor expansion of the exponential term, i.e.,

$$[e^{\rho_3 r_m^{II}(\mu_0\cos\theta - \mu_1)} - 1] \cong \rho_3[e^{r_m^{II}(\mu_0\cos\theta - \mu_1)} - 1]$$

Then, comparing equation (5) and (8) we obtain:

$$D_1^{II}(d_1) = e^{(1-\rho_2)\mu_0(d_1-d_2)}\; e^{(1-\rho_3)\mu_0 d_2}\; \rho_3\; D_{1w}^{II}(d_1) \qquad (9)$$

In order to simplify the expression for the analytic dose,

we may express it as : $D_A = D_o (1 + D_1/D_o)$ where D_1/D_o is the ratio of single scatter to primary dose at P. Then, using equations (1), (7), and (9) we can write:

$$D_A = \phi_0 \left(\frac{\mu_{en}}{\rho}\right) E_0 \, e^{-\mu_0[\rho_2(d_1-d_2)+\rho_3 d_2]} \quad \ldots$$

$$\ldots \quad \left\{ 1 + \frac{e^{\mu_0[\rho_2(d_1-d_2)+\rho_3 d_2]} \, D_1^I(d_1)}{\phi_0 \left(\frac{\mu_{en}}{\rho}\right) E_0} + \frac{e^{\mu_0 d_1 \rho_3 D_{1w}^{II}(d_1)}}{\phi_0 \left(\frac{\mu_{en}}{\rho}\right) E_0} \right\} \quad (10)$$

B. The Batho Equation

For the situation depicted in Figure 3.14, the Batho correction factor using TAR's is given by:

$$CF_B(TAR) = \frac{[TAR(d_2,r)]^{\rho_3-\rho_2}}{[TAR(d_1,r)]^{1-\rho_2}} = \frac{[D_w(d_2)]^{\rho_3-\rho_2} \, [D_a]^{1-\rho_2}}{[D_w(d_1)]^{1-\rho_2} \, [D_a]^{\rho_3-\rho_2}}$$

$$= \frac{[D_w(d_2)]^{\rho_3-\rho_2}}{[D_w(d_1)]^{1-\rho_2}} \, [D_a]^{1-\rho_3} \quad (11)$$

where D_a = dose to a small mass of tissue in air,

$D_w(d_1)$ = dose in water at depth d_1,

$D_w(d_2)$ = dose in water at depth d_2.

The revised Batho correction factor, substituting TMR's instead, is:

$$CF_B(TMR) = \frac{[TMR(d_2,r)]^{\rho_3-\rho_2}}{[TMR(d_1,r)]^{1-\rho_2}} \cdot \frac{[D_w(d_2)]^{\rho_3-\rho_2}[D_m]^{1-\rho_2}}{[D_w(d_1)]^{1-\rho_2}[D_m]^{\rho_3-\rho_2}}$$

$$= \frac{[D_w(d_2)]^{\rho_3-\rho_2}}{[D_w(d_1)]^{1-\rho_2}}[D_m]^{1-\rho_3} \qquad (12)$$

where D_m is now the reference maximum dose, measured in phantom. The only difference between $CF_B(TAR)$ and $CF_B(TMR)$ is in the use of different calibrations which are based on D_a (no phantom scatter) or D_m (phantom scatter), respectively.

We can now proceed to calculate D_B. For simplification again, we divide the dose in water into its primary component, D_{0w}, and its first-scatter component, $D_{1w} = D_{1w}^I(d_1) + D_{1w}^{II}(d_1)$. Then,

$$D_w(d_2) = D_{0w}(d_2)\left[1 + \frac{e^{\mu_0 d_1}}{\phi_0(\frac{\mu_{en}}{\rho})E_0} D_{1w}^{II}(d_1)\right] \qquad (13)$$

and

$$D_w(d_1) = D_{0w}(d_1)\left[1 + \frac{e^{\mu_0 d_1}}{\phi_0(\frac{\mu_{en}}{\rho})E_0}(D_{1w}^I(d_1) + D_{1w}^{II}(d_1))\right] \qquad (14)$$

where $D_{1w}^I(d_1)$ and $D_{1w}^{II}(d_1)$ are given by analytic expressions (4) and (5). The dose calculated using the Batho correction factor, equation (12) is given by:

$$D_B(TMR) = CF_B(TMR) \ D_W(d_1)$$

$$= [D_{0W}(d_2)]^{\rho_3-\rho_2}[D_{0W}(d_1)]^{\rho_2}D_m^{1-\rho_3}[1 + \frac{e^{\mu_0 d_1}}{\Phi_0(\frac{\mu_{en}}{\rho})E_0}D_{1W}^{II}(d_1)]^{\rho_3-\rho_2}\ldots$$

$$\ldots \quad \{1 + \frac{e^{\mu_0 d_1}}{\Phi_0(\frac{\mu_{en}}{\rho})E_0}[D_{1W}^{I}(d_1) + D_{1W}^{II}(d_1)]\}^{\rho_2} \qquad (15)$$

If D_B is approximated by a first-order binomial expansion, then

$$D_B(TMR) = [\Phi_0(\frac{\mu_{en}}{\rho})E_0]^{\rho_3} \ e^{-\mu_0[\rho_2(d_1-d_2)+\rho_3 d_2]}D_m^{1-\rho_3} \quad \ldots$$

$$\ldots \quad [1 + \frac{e^{\mu_0 d_1}}{\Phi_0(\frac{\mu_{en}}{\rho})E_0}(\rho_2 D_{1W}^{I}(d_1) + \rho_3 D_{1W}^{II}(d_1))] \qquad (16)$$

But $D_m = P_m \ (1 + S_m/P_m)$

$$D_m^{1-\rho_3} = P_m^{1-\rho_3} [1 + S_m/P_m]^{1-\rho_3} \cong P_m^{1-\rho_3} [1 + (1 - \rho_3) S_m/P_m]$$

$P_m = \Phi_0(\frac{\mu_{en}}{\rho})E_0 \ e^{-\mu_0 d_{max}}$ is the primary dose and S_m is the scatter dose in phantom at the calibration reference depth. Then,

$$D_B = \Phi_0(\frac{\mu_{en}}{\rho})E_0 e^{-\mu_0 d_m+\rho_3\mu_0 d_m}\{e^{-\mu_0[\rho_2(d_1-d_2)+\rho_3 d_2]}\}(1+(1-\rho_3)S_m/P_m) \ \ldots$$

$$\ldots \quad \{1+\frac{e^{\mu_0 d_1}}{\Phi_0(\frac{\mu_{en}}{\rho})E_0}[\rho_2 D_{1W}^{I}(d_1)+\rho_3 D_{1W}^{II}(d_1)]\} \qquad (17)$$

For the Batho correction factor to yield a dose which is analytically correct for primary and first scatter, we require that equations (10) and (17) be equal:

$$1 + \frac{e^{\mu_0[\rho_2(d_1-d_2)+\rho_3 d_2]} D_1^I(d_1)}{\Phi_0 (\frac{\mu_{en}}{\rho}) E_0} + \frac{\rho_3 e^{\mu_0 d_1} D_{1w}^{II}(d_1)}{\Phi_0 (\frac{\mu_{en}}{\rho}) E_0} = e^{-\mu_0 d_m(1-\rho_3)} \quad \cdots\cdots$$

$$\cdots\cdots [1 + (1-\rho_3)S_m/P_m] \{1 + (e^{\mu_0 d_1}/\Phi_0 (\frac{\mu_{en}}{\rho}) E_0)[\rho_2 D_{1w}^I(d_1) + \rho_3 D_{1w}^{II}(d_1)]\} \quad (18)$$

For the case when the measuring point P lies in water-like tissue beyond lung (i.e. $\rho_3 = 1$, $\rho_2 \neq 1$)

$$D_1^I(d_1) = e^{(1-\rho_2)\mu_0(d_1-d_2)} \rho_2 D_{1w}^I(d_1)$$

and condition (18) is exactly satisfied as shown by Wong and Henkelman (139). Note that in this case, the reference dose, D_m or D_a cancels and does not appear in relation (18). This suggests that agreement beyond lung between measured and calculated values would not depend on the choice of TAR's or TMR's, as shown experimentally in Figure 3.17. However, for points P within lung (i.e. $\rho_2 = 1$ and $\rho_3 \neq 1$) relation (18) cannot be simplified. In order to verify the equality $D_1^I(d_1)$, $D_{1w}^I(d_1)$, $D_{1w}^{II}(d_1)$ and the dose at the reference point, S_m, P_m must be evaluated.

A computer program was written in FORTRAN 77 to

calculate $D_1^I(d_1)/\Phi_0$, $D_{1w}^I(d_1)/\Phi_0$, and $D_{1w}^{II}(d_1)/\Phi_0$

analytically for some of the experimental conditions used. Results are shown in Table 3.9. Equation (18) can be rearranged so that we can calculate S_m/P_m.

$$S_m/P_m = \frac{-1}{(1-\rho_3)} \quad \ldots\ldots$$

$$\ldots\ldots + \frac{(\frac{\mu en}{\rho}) E_0 + e^{\mu_0[\rho_2(d_1-d_2)+\rho_3 d_2]}(D_1^I(d_1)/\Phi_0) + \rho_3 e^{\mu_0 d_1}(D_{1w}^{II}(d_1)/\Phi_0)}{(1-\rho_3) e^{-\mu_0 d_m}(1-\rho_3)[(\frac{\mu en}{\rho}) E_0 + e^{\mu_0 d_1}\{\rho_2 D_{1w}^I(d_1)/\Phi_0 + \rho_3 D_{1w}^{II}(d_1)/\Phi_0\}]} \quad (19)$$

S_m/P_m can also be obtained from a Monte Carlo calculation. For a Cobalt-60 beam and a field size of 10x10 cm², S_m/P_m is 0.039 (T.R.Mackie, private communication), which is in very good agreement with the values as calculated by equation (19). Wong (140) gives S_m/P_m = 0.043 for an infinite field size. Therefore, using CF (TMR) we expect good agreement with measured values in lung. If CF_B(TAR) had been used, D_a would appear in equation (16) instead of D_m and S_a/P_a would be used instead of S_m/P_m in equations (17),(18), and (19). The right hand side of equation (19) would remain unaltered but would now equal S_a/P_a. This expression was calculated by computer and its numerical value is given in the last column of Table 3.9. Typically, the layer for electron equilibrium used at Cobalt-60 is only 0.5cm so that S_a/P_a is negligible and does not give the correct numerical result. The correct

Table 3.9: Analytically calculated doses at P
(Figure 3.19) for different thicknesses of the
layers I and II.

	$D_{1w}^{II}(d_1)/\Phi_0$ (keV cm²/g)	$D_{1w}^{I}(d_1)/\Phi_0$ (keV cm²/g)	$D_{1}^{I}(d_1)/\Phi_0$ (keV cm²/g)	calculated S_m/P_m or S_a/P_a
	Field diameter = 5.6 cm			
$d_1=15$cm $d_2=10$cm	2.7600	0.2709	0.4213	0.0322
$d_1=15$cm $d_2=7.5$cm	2.5180	0.5127	0.7167	0.0326
$d_1=15$cm $d_2=5$cm	2.1221	0.9088	1.1423	0.0331
$d_1=15$cm $d_2=3$cm	1.6015	1.4295	1.6495	0.0338
$d_1=15$cm $d_2=1$cm	0.7770	2.2539	2.3774	0.0340
	Field diameter = 11.2 cm			
$d_1=15$cm $d_2=10$cm	4.0045	0.7642	1.2235	0.0348
$d_1=15$cm $d_2=7.5$cm	3.4360	1.3327	1.9139	0.0367
$d_1=15$cm $d_2=5$cm	2.6817	2.0870	2.6834	0.0387
$d_1=15$cm $d_2=3$cm	1.9040	2.8648	3.3597	0.0394
$d_1=15$cm $d_2=1$cm	0.9089	3.8599	4.0967	0.0372

value to use in equation (19) is S_m/P_m, and therefore TMR's should be used in the Batho correction. D_B and CF_B(TAR) would consistently underpredict doses within lung. From Table 3.9 one can observe that as the field size is increased the right hand side of equation (19) increases in value. S_m/P_m also increases for larger fields, but S_a/P_a remains negligible. Therefore, the deviation of CF_B(TAR) from measured values should get larger as the field size is increased; this is also observed experimentally.

The fact that CF_B(TAR) is lower than CF_B(TMR) can also be deduced from equation 1B.

$$CF_B(TMR) = [TMR(d_2,r)]^{\rho_3-1}$$
$$= [TAR(d_2,r)/TAR(d_m,r)]^{\rho_3-1}$$
$$= [TAR(d_2,r)]^{\rho_3-1} \quad [TAR(d_m,r)]^{1-\rho_3}$$
$$= CF_B(TAR)[TAR(d_m,r)]^{1-\rho_3}$$

For lung, $1-\rho_3 > 1$ and $[TAR(d_m,r)] > 1$. Therefore CF_B(TMR) $> CF_B$(TAR) and since $TAR(d_m,r)$ increases with increasing field size, the inequality increases with increasing field size. A partial physical explanation why CF_B(TMR) should give better agreement is that;

(a) the TMR value includes no inherent backscatter

(b) the TAR value includes inherent backscatter.

In lung of density 0.3 g/cm^3, backscatter is reduced and (a) is more appropriate.

V. CONCLUSIONS

In this paper we have investigated the Batho power-law method for calculating dose within lung. Experiments indicate good agreement between measured and calculated dose for points in water-like tissue beyond lung. If the measurement point lies within lung however, there are large discrepancies between calculated and measured doses only if TAR's are used. When TMR's are substituted, the agreement improves considerably for Cobalt-60 irradiation. Agreement is also good for 6 MV X-rays where TMR's are normally used.

The reasons for these different results using TMR or TAR's were studied by comparison with analytic calculations of primary and first-scatter dose. If the reference dose calibration is performed in phantom, there is closer agreement between the Batho and analytic expression.

An improvement in accuracy for dose calculations for points within lung by as much as 5% can be achieved simply by substituting TMR's in the Batho correction factor instead of the customary TAR's. This is particularly important for large field irradiation, which is now used more routinely (32).

3.6 Complex Heterogeneous Phantoms

The human thorax is by no means similar to the simple geometries discussed in the previous sections. The lungs are finite in width, separated by a mediastinal section of water-like tissue and may be smaller than the radiation field. The simpler inhomogeneity correction methods tested and discussed in section 3.4 do not take into account the lateral extent of the inhomogeneity (except for the equivalent TAR method). The effect of changing the lateral size of the inhomogeneity is now investigated. Since we are primarily interested in large field dosimetry, a field size of 40x40 cm^2 was chosen for these experiments. The experimental set-up is shown in Figure 3.23. A cork thickness of 10 cm was used and this cork was "shrunken" laterally so that its cross section ranged from 30x30 cm^2 to 2x2 cm^2. For the simple slab geometries discussed in section 3.4, the Batho correction method performed very well for small as well as large fields and various thicknesses of inhomogeneities. Therefore measured inhomogeneity correction factors were compared with those calculated with the Batho method. For a point 5 cm below the cork section, the correction factors were plotted for decreasing lateral size of the cork (see Figure 3.20). For cork areas of less than 30x30 cm^2, the measured ICF increases gradually and deviates by 7% from the constant correction factor predicted by the Batho method for a 5x5 cm^2 area of the cork inhomogeneity. For
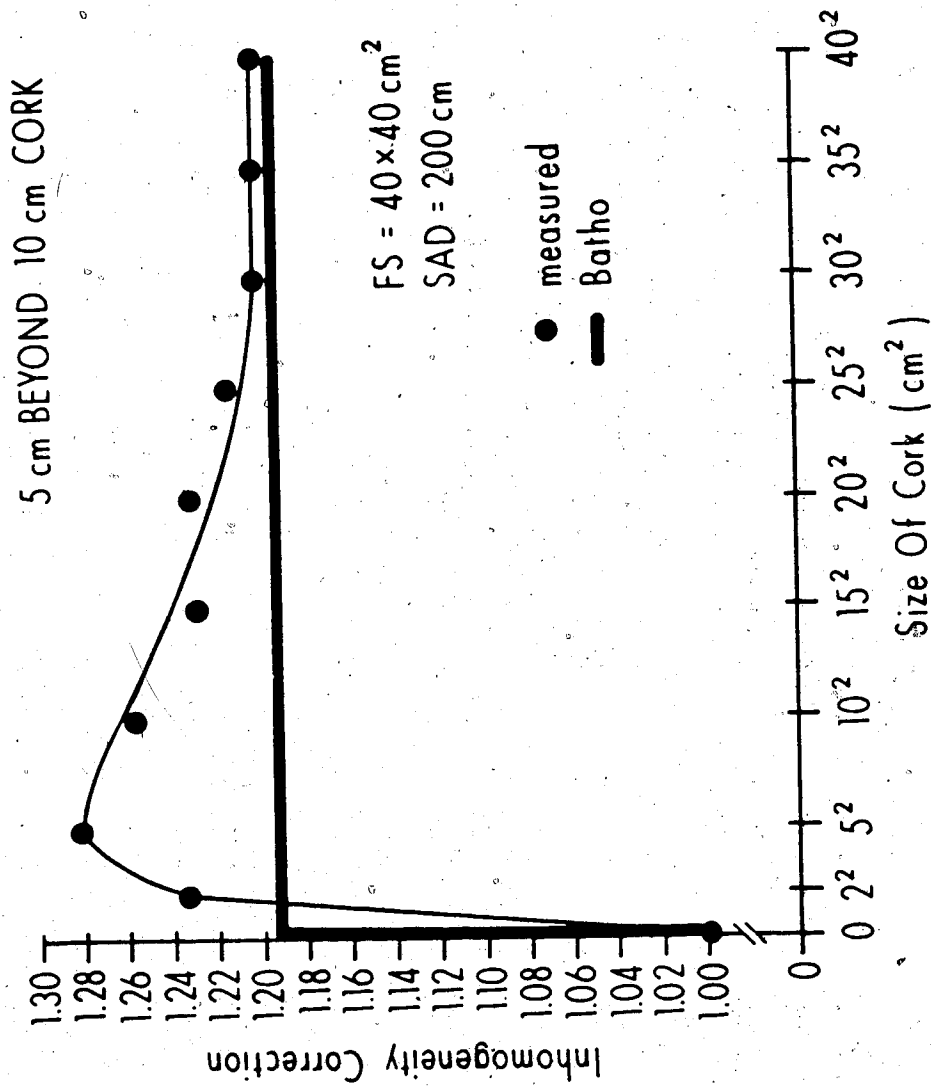
Fig. 3.20 The inhomogeneity correction for 6 MV X-rays at a point 5 cm below a 10 cm thick cork for varying lateral dimensions of the cork.

194

cork sizes smaller than 5x5 cm², the correction factor decreases, as is expected since it should return to 1.00 when the inhomogeneity width approaches zero.

Another type of phantom which was investigated consisted of two separated cork volumes on each side of a unit-density "mediastinum" along the central axis. The cork thickness was kept at 10 cm, while their cross-sectional areas were 20x20 cm². In this experiment, the cross-sectional area of mediastinum was varied from 5x20 cm² to 20x20 cm². This set-up is shown in Figure 3.21. Although this geometry is still rectilinear, it resembles more closely the configuration of the human thorax. In this case, the Batho method predicts a constant correction factor of 1.0 since the inhomogeneity does not lie directly above the point of calculation along the central axis. Experimentally, and for both sizes of mediastinum, the correction factor varies from 0.97 to 0.99 (Figure 3.21) for all positions of the cork volume. This lower factor is expected because there is a decrease in scattered radiation laterally in this geometry. If there is only one volume of cork on one side of the mediastinum, correction factors of 0.99 were measured for distances of the cork between 2 to 4 cm from the central axis.

In order to calculate doses correctly in the above two situations, only inhomogeneity correction methods which account for the lateral extent of the inhomogeneity

6MV X-rays
FS = 40×40 cm²

c = 10×20 cm²
● measured
○ Eq. TAR

c = 5×20 cm²
▲ measured
△ Eq. TAR

● Batho

40×40 cm²

Inhomogeneity Correction

1.06
1.04
1.02
1.00
0.98
0.96

a (cm)

0 1 2 3 4 5 6 7 8 9 10 11 12 13 14 15
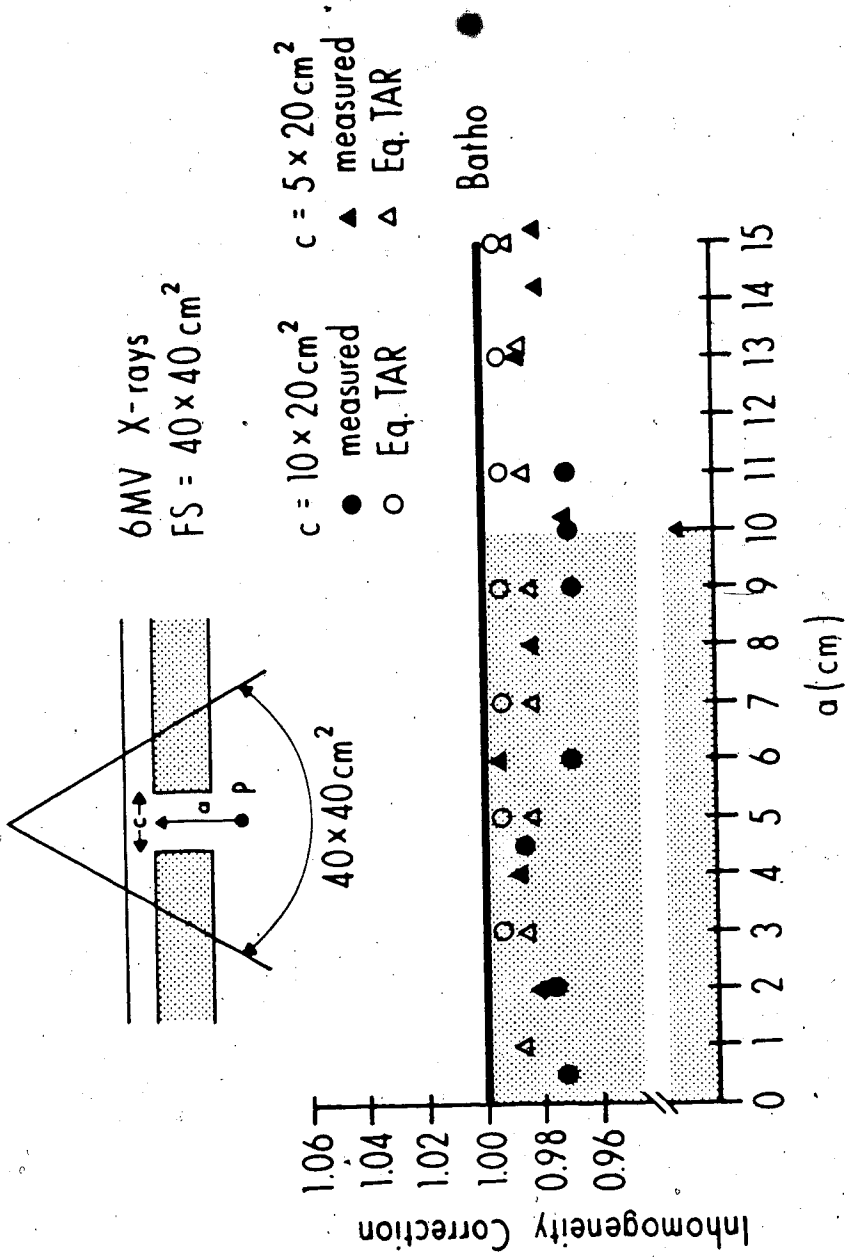
Fig. 3.21 The inhomogeneity correction for 6 MV X-rays as a function of parameter "a" for a "mediastinum" of lateral size, c=5x20 cm², and c=10x20 cm².

have the potential to be accurate. However, the simpler methods could and have been modified for this purpose. For the situation shown in Figure 3.23 a scaled TMR could be determined for an equivalent water depth and width. Then a correction factor can be calculated as follows:

$$ ICF = \frac{TMR(d',W_d')}{TMR(d,W_d)} $$

where d' and W_d' are the water-equivalent depth and field size, scaled according to density (80), and d, W_d are the geometric depth and field size. The field size is scaled according to density in both lateral directions. A similar approach was used initially in the formulation of the equivalent TAR method (108). This factor can be used inside cork. But for calculation points beyond cork this method would not account for the distance of the cork from the calculation point.

Another possibility has been suggested by Lulu and Bjarngard (69), and involves dividing the total phantom into constituent parts as shown in Figure 3.22. The inhomogeneity correction factor is calculated as usual for phantom 4 which now has an inhomogeneity of dimensions equal to the field. The dose at P_4 is:

$$ D_4 = D_3 \times ICF $$

The correction factor for situation 1 is then:
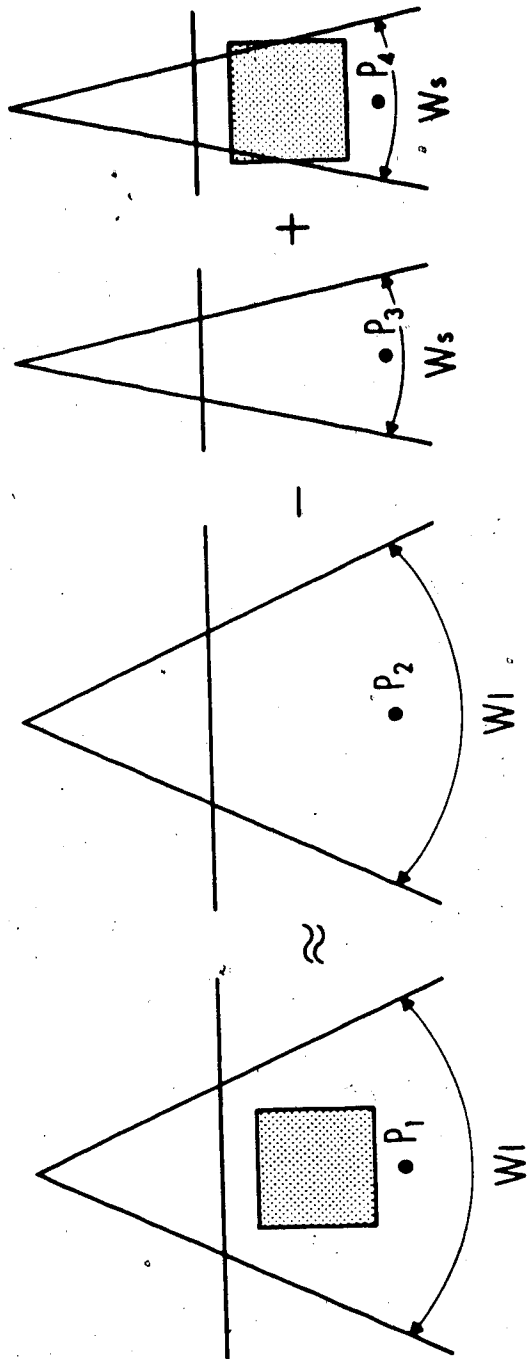
Fig. 3.22 The composite "phantom" used in the calculation of the inhomogeneity correction factor proposed by Lulu and Bjarngard (69).

$$ICF = D_1/D_2 = \frac{D_2 - D_3 + D_3(ICF)}{D_2} = 1 - (D_3/D_2)(1 - ICF)$$

$$= 1 - \left[\frac{TMR(d,W_s)D(d_m,W_s)}{TMR(d,W_l)D(d_m,W_l)}\right](1 - ICF)$$

ICF can also be replaced by any other correction factor which assumes the lateral extent of the inhomogeneity is greater than the beam size (56). In our case we use the Batho correction factor for ICF , as it had given the best results in similar situations.

The Lulu and Bjarngard correction factor ICF_{LB} as well as the scaled TMR factor ICF_{SC} were tested on the phantom shown in Figure 3.23. For cork sizes 10x10 cm^2 to 35x35 cm^2 in a 40x40 cm^2 field, the correction factor using ICF_{LB} was within 4% of measured values, underpredicting the correction factor within cork but overpredicting it beyond, as seen in Figure 3.23 A,B,C. The ICF is plotted as a function of parameter "a" as shown in Figure 3.23 for three sample cork sizes. The correction factor calculated using ICF_{SC} is within 3% of the measured values in cork. However, beyond cork it predicts a constant ICF as does the simple ratio of TAR's. This is expected since this correction method cannot sense the proximity of the cork to the point of calculation. Therefore this method is appropriate for calculation of doses within cork (or lung), but not beyond.

Since the detailed equivalent TAR method accounts for lateral dimensions of the inhomogeneity smaller than the field size, the above situation is one in which it should

Fig. 3.23 The inhomogeneity correction factor for 6 MV X-rays as a function of parameter "a". The lateral dimension of the cork, b, is varied

(A) 5x5 cm², (B) 10x10 cm², (C) 20x20 cm².

6MV X-rays
FS = 40 × 40 cm²
b = 10 × 10 cm²

Lulu + Bjarngard
measured
scaled TMR
Eq TAR
Batho

6MV X-rays
FS = 40 × 40 cm²
b = 20 × 20 cm²

Lulu + Bjarngard
measured
scaled TMR
Eq TAR
Batho

6MV X-rays
FS = 40 × 40 cm²
b = 5 × 5 cm²

Lulu + Bjarngard
measured
scaled TMR
Eq TAR
Batho
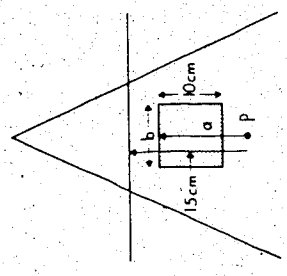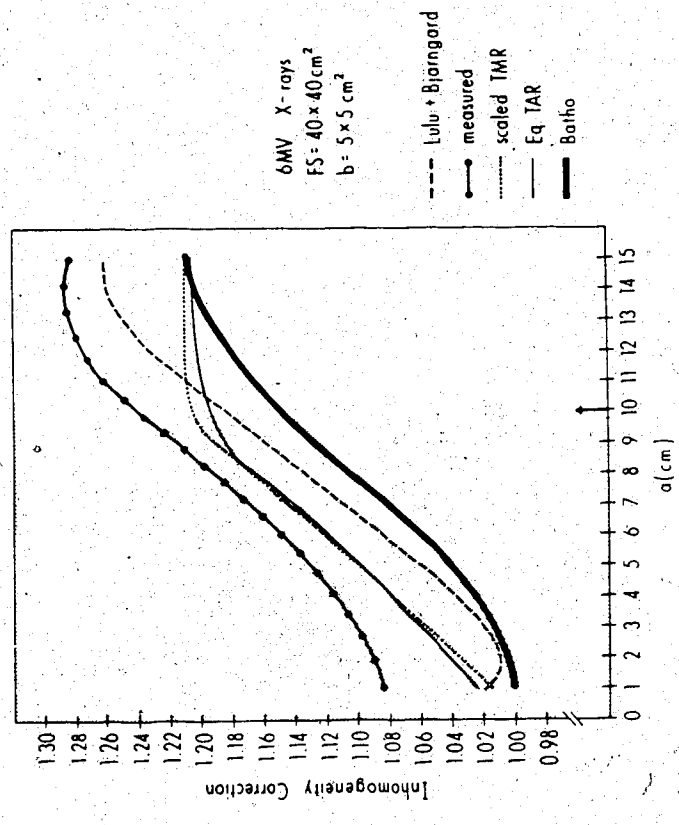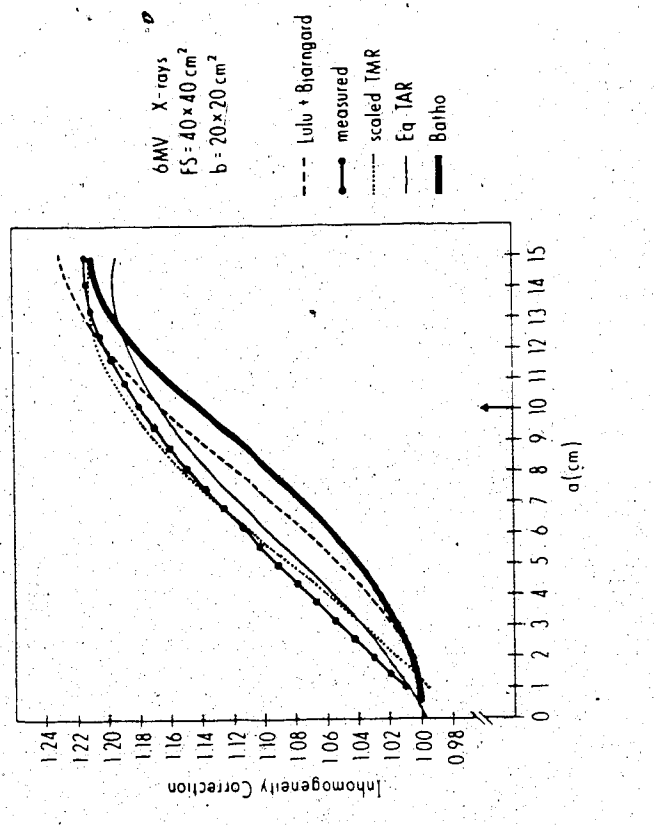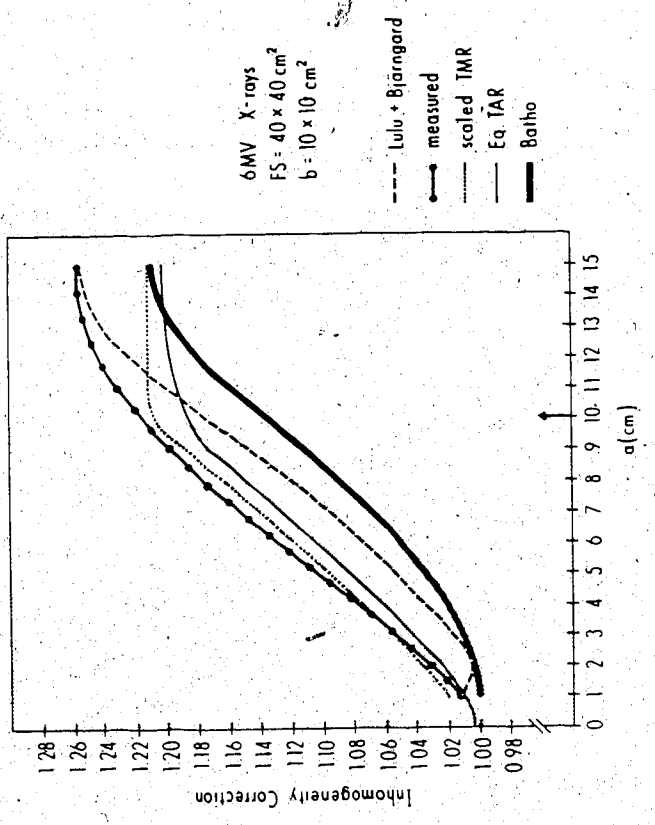
perform very well. Indeed, within lung, correction factors are within 2% of the measured values (Figure 3.23). Beyond lung, and for cork sizes of 10x10 cm^2 and smaller, discrepancies are larger. For comparison, correction factors calculated using the generalized Batho method are also shown in Figure 3.23.

When the cork is only 5x5 cm^2 along the central axis in a 40x40 cm^2 field, Figure 3.23 A, irregularities occur and both ICF_{LB} and ICF_{SC} underpredict the experimental ICF by as much as 8% in the first few centimeters of cork. In this case, most of the cork thickness lies behind the probe. Most of the material above the probe is of unit-density which scatters radiation and sets electrons in motion more than cork does. However, some cork lies directly above the probe and transmits more of these scattered photons and electrons set in motion than unit-density material. This cork volume is insufficient to achieve electronic equilibrium, but electrons set in motion in the surrounding unit-density material can reach the probe from three sides. Therefore the situation is such that an excess of electrons reaches the probe, thereby increasing the dose. The calculation methods which do not account for dose due to electron transport, do not give the correct ICF.

For the mediastinum phantom shown in Figure 3.21, the correction factor is plotted versus parameter "a". For the two mediastinum sizes, the correction factor is 0.97

to 0.99 for all positions of the 10 cm cork volumes. The equivalent TAR method "senses" this situation and predicts the correct correction factor. The Batho method as well as ICF_{LB} yield a factor of 1.0. It will be in error by less than 3% for mediastinum sizes $5x20$ cm^2 to $20x20$ cm^2. These are the typical mediastinum sizes encountered in human hemi-body irradiation. The ICF_{SC} deviates by as much as -6% from the measured values. The effect of the cork on the dose at the central axis is exaggerated and this factor is not useful for dose calculations in the mediastinum.

In conclusion then, for all these rectangular geometries, the simple correction factors can be used to calculate doses beyond, within, and lateral to lung inhomogeneities with an accuracy of 3% along the central axis. The only exception is for a small inhomogeneity along the central axis in a large field; near the first cork-prestwood interface, discrepancies of .8% were detected. This can be attributed to electronic disequilibrium above and to the sides of the probe which is not handled by any of these methods. Geometries such as inhomogeneities smaller than field size along the central axis and water-equivalent material along the central axis with inhomogeneities to the side will be less of a problem as the energy of the beam is increased (114). At higher energies the contribution to dose by scattered radiation is reduced, and is more forward peaked (i.e.

behaving more like the primary beam). Therefore, there will be less photon scatter from points distant from the central axis. However, for higher energy beams, the range of electrons set in motion is greater, and therefore electronic disequilibrium may develop, especially for small fields. Inhomogeneity correction methods which handle scattered photon radiation correctly will not be affected by a change in the direction of the scatter, but most of these methods do not handle electronic disequilibrium. Therefore there will be problems with higher energy beams at interfaces of two media where electron transport is disturbed.

SUMMARY

In the above experiments, various inhomogeneity correction methods were tested in a variety of situations similar to those encountered in radiotherapy of the thorax. None of the methods performed very well in all situations. It is therefore recommended that before any one method is chosen to correct doses for lung, its performance be verified in the situations likely to be encountered clinically. Moreover, if a method performs well at one energy of radiation, it is not to be assumed that it performs well at another. Finally, the accuracy of these calculation methods should be checked in a humanoid phantom. This will be the subject of the next section.

3.7 Humanoid Phantom

So far, only central-axis doses in simple rectilinear phantoms have been investigated. The accuracy of the calculation methods for "off-axis" points, which are relevant for hemi-body irradiations, was therefore investigated. The Alderson RANDO phantom (62) was used to simulate the human thorax. It is constructed of materials simulating the anatomical structures and densities as well as the typical external shape of the human.

If TMR's measured along the central axis are to be used for off-axis calculations, corrections must be applied for variations in photon fluence across the beam. For Cobalt-60, this does not create a serious problem because the primary photon fluence is very uniform (69,113,133). However, for X-ray beams from linear accelerators, the fluence "profile" depends on the X-ray target, the flattening filter, and collimation. For the 6 MV accelerator used in our experiments, the profile was measured at several depths in a water phantom irradiated with a 40x40 cm² field. Results are shown in Figure 3.24. The path lengths of primary rays will be different off-axis due to the divergence of the beam. However, for a 40x40 cm² field at an SSD of 200 cm, and a depth of 15 cm in a phantom, there will be a change in pathlength of only 0.07 cm up to the outer edge of the beam. Thus the divergence of the beam produces a negligible effect for the large fields at a distance of 200 cm. Thus, the major

MEASURED PROFILES

6MV X-rays
FS = 40×40cm^2
SSD = 200 cm

Depth 1.5 cm

Depth 5 cm

Depth 10 cm

Depth 25 cm

Reading
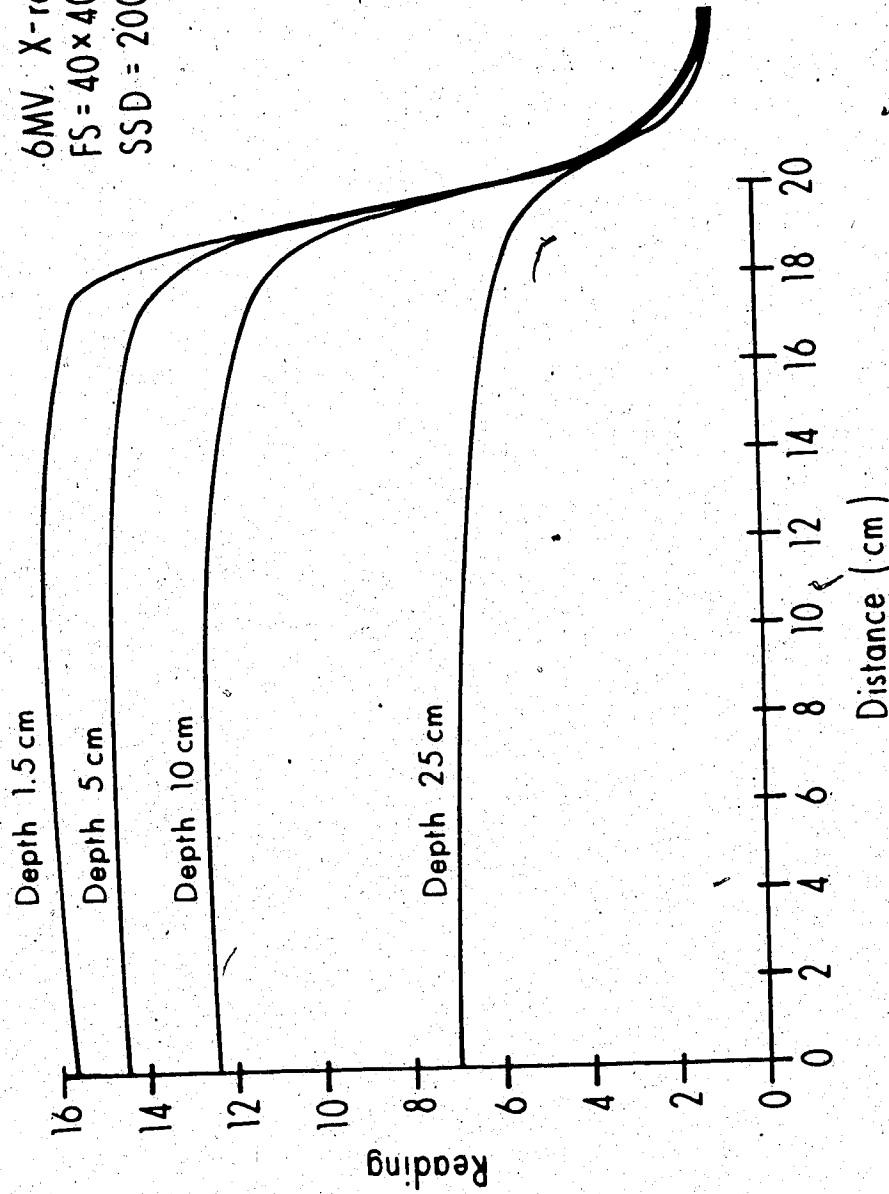
Distance (cm)

Fig. 3.24 Radiation profiles across the beam measured at several depths

in a water phantom for 6 MV X-rays at a source-to-surface

distance of 200 cm.

differences in fluence at a depth are due to the characteristics of the accelerator and beam-shaping devices.

In order to simulate the hemi-body treatment a field size of 40x40 cm² at an SSD of 200 cm incident on the posterior side of the phantom was used. (In practice, a pair of parallel opposed fields is used.) The posterior-anterior distance in the thorax region was between 21.5 to 23 cm. The lateral dimensions ranged from 39 cm at the shoulders to 32.5 cm at the waist. For calculation purposes, the field dimensions are determined by the size of the field or the size of the phantom whichever is smaller (26). However, since TMR's change little for field sizes ranging from 30x30 cm² to 40x40 cm², it is valid to use TMR's measured for a 40x40 cm² field to calculate doses in the RANDO thorax. The 40x40 cm² radiation field encompassed RANDO slices 12-26, with the central axis along slice 18. The inner dimensions, as well as the densities in the thorax were determined from a CT scan of the phantom. Slices 14 to 23 were scanned, with a CT slice thickness and indexing of 1 cm. The average relative lung density of 0.37 was determined by tracing the entire lung. The posterior-anterior diameter of lung in the mid-thorax slices was in the range of 13 to 16 cm, while the lateral size was typically 8 to 10 cm. Similar values were obtained from human thorax scans and are also published by Van Dyk et al. (126).

Several capsules filled with thermoluminescent (TLD) powder, were inserted in various places into the Rando slices number 15, 17 and 18. The precision and accuracy of this dosimeter is 3% and has been discussed in section 3.1.3.2 The phantom was irradiated and doses were determined. The positions of the TLD capsules are shown in the CT scans of Figure 3.25.

To verify the calibration of the TLD dosimeters the dose at d_{max} in the geometrical prestwood phantom was measured both with TLD and with the ionization probe. From this comparison, a table of TMR's for a 40x40 cm^2 field and the known profile across the beam, doses at all depths in a water phantom can be obtained (3). Doses were calculated for each of the positions of the TLD dosimeters. If the dosimeter was in lung, a correction factor was calculated using the modified Batho method (109), the Batho correction according to Lulu and Bjarngard, and the scaled TMR methods described in section 3.6. Two computer calculation methods were also used to obtain complete dose distributions in the entire RANDO slice. From these, correction factors were calculated at the positions of the TLD dosimeters. The calculated and measured correction factors for several positions in and out of lung are given in Table 3.10. One of the computer calculations was performed on the computer developed at the Cross Cancer Institute for radiotherapy planning (8). A CT image of the Rando slice was entered. The lungs were
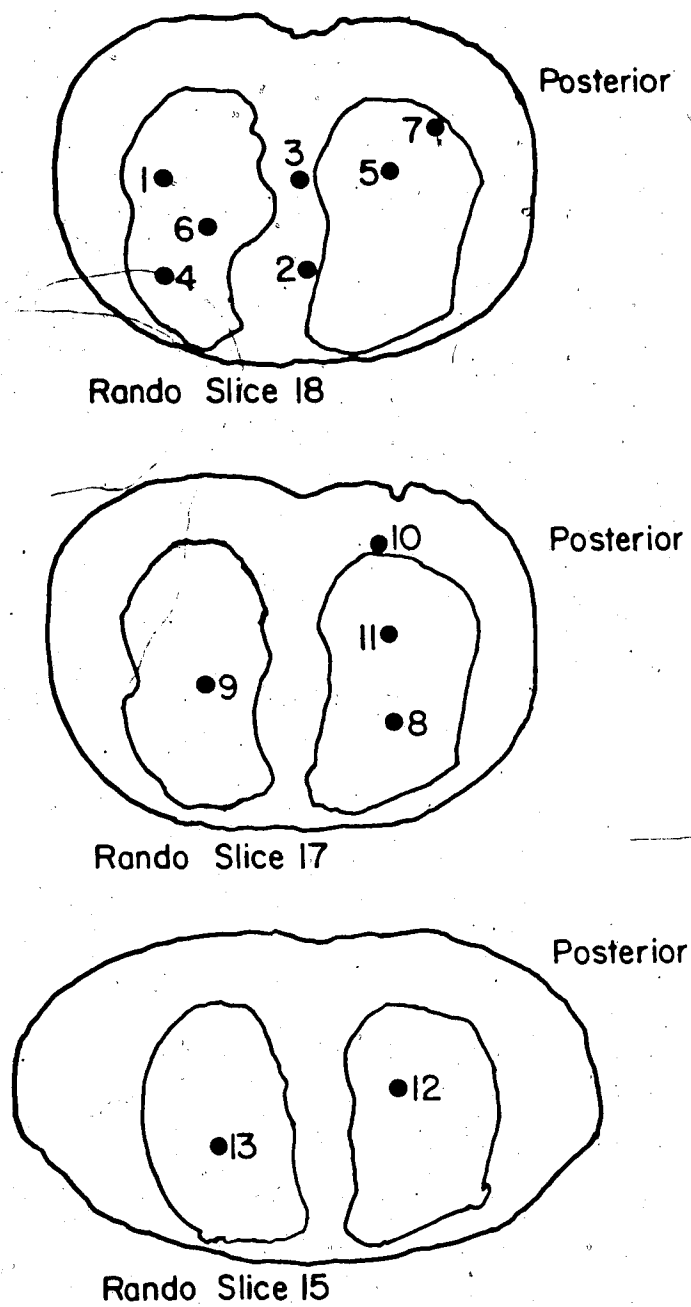
Fig. 3.25 Positions of the TLD dosimeters are indicated
in the CT scans of Rando slices (a) 18, (b) 17,
and (c) 15.

209

Table 3.10: Measured and calculated correction factors in Rando

TLD Number	Distance from surface (cm)	Distance in lung (cm)	measured ICF	Generalized Batho (CCI)	Lulu and Bjarngard	scaled TMR	eq. TAR
1	10.85	4.96	1.100	1.033	1.047	1.057	1.056
2	15.40	0	1.050	1.000	1.000		1.017
3	9.50	0	1.046	1.000	1.000		1.013
4	16.80	12.22	1.205	1.155	1.194	1.201	1.159
5	9.90	4.75	1.015	1.029	1.044	1.050	1.047
6	14.00	9.05	1.172	1.099	1.125	1.125	1.126
7	6.17	0.68	1.023	1.000	1.000		0.989
8	15.90	10.86	1.202	1.125	1.164	1.170	1.169
9	13.90	9.05	1.114	1.099	1.125	1.127	1.143
10	4.56	0	0.987	1.000	1.000		1.005
11	9.90	4.98	1.084	1.033	1.049	1.054	1.066
12	10.70	5.66	1.079	1.041	1.059	1.066	1.080
13	13.80	8.84	1.106	1.096	1.120	1.140	1.142

outlined by joystick on the video screen and assigned an average density of 0.37 g/cm³. The dose distribution in lung is calculated using the generalized Batho correction method. Such a distribution is shown in Figure 3.26 for Rando slice 18. The correction factors thus obtained are similar to those calculated manually using the Batho correction, as expected.

The second computer calculation was performed at the Ontario Cancer Institute, using the detailed equivalent TAR method based on pixel-by-pixel information available from a CT scan. All slices in the radiation field were scanned and used for a three-dimensional dose calculation. Such a dose distribution superimposed on the CT slice is shown in Figure 3.27 for Rando slice 18. For comparison a two-dimensional calculation, using only the central slice and assuming symmetry in the third dimension was also done (12). Correction factors calculated using the two-dimensional calculation are within 1% of those calculated using a three-dimensional calculation. Therefore in hemi-body irradiations a two-dimensional calculation would appear to be sufficient provided the calculation slice is not near the lung apex or the diaphragm.

The agreement between the detailed equivalent TAR values and those measured is better than ±4%. (The uncertainty of the TLD measurement, however, is itself of this order). The simple scaled TMR method also gives
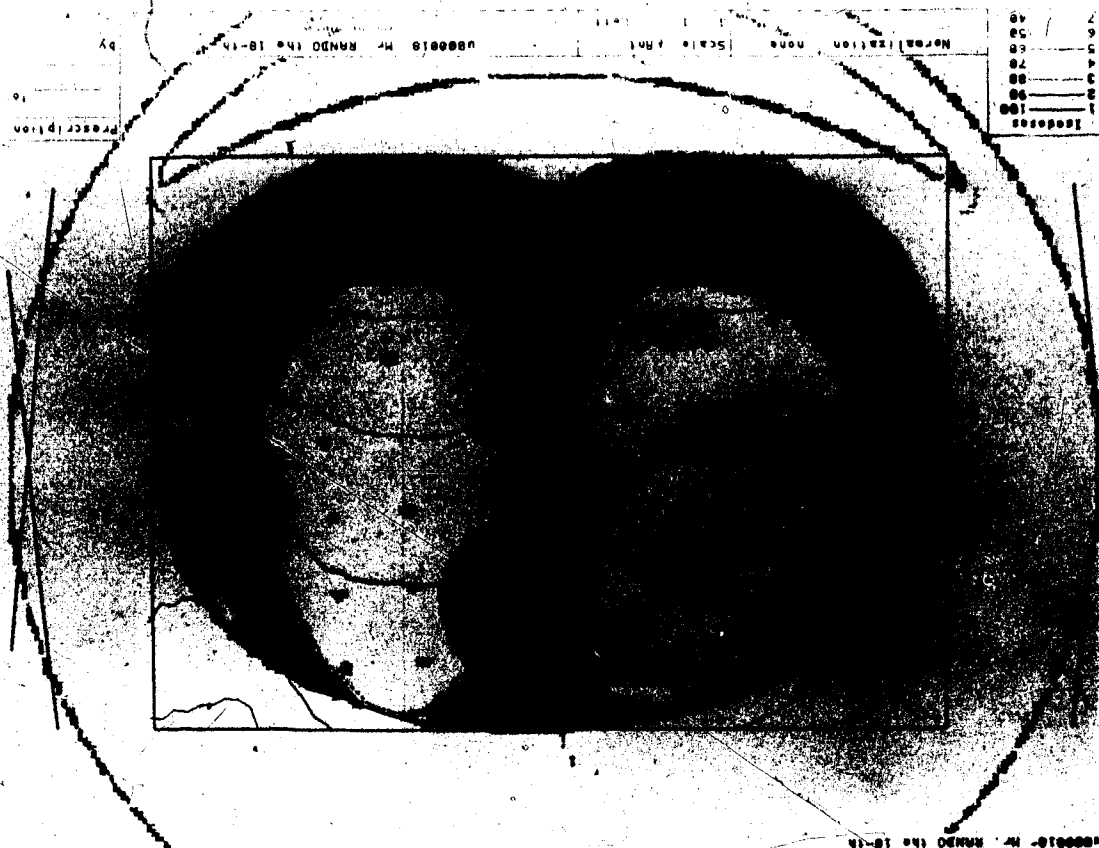
Fig. 3.26 The dose distribution in a CT scan of Rando
slice 18 is shown. The inhomogeneity correction
was performed using the generalized Batho
method (109).
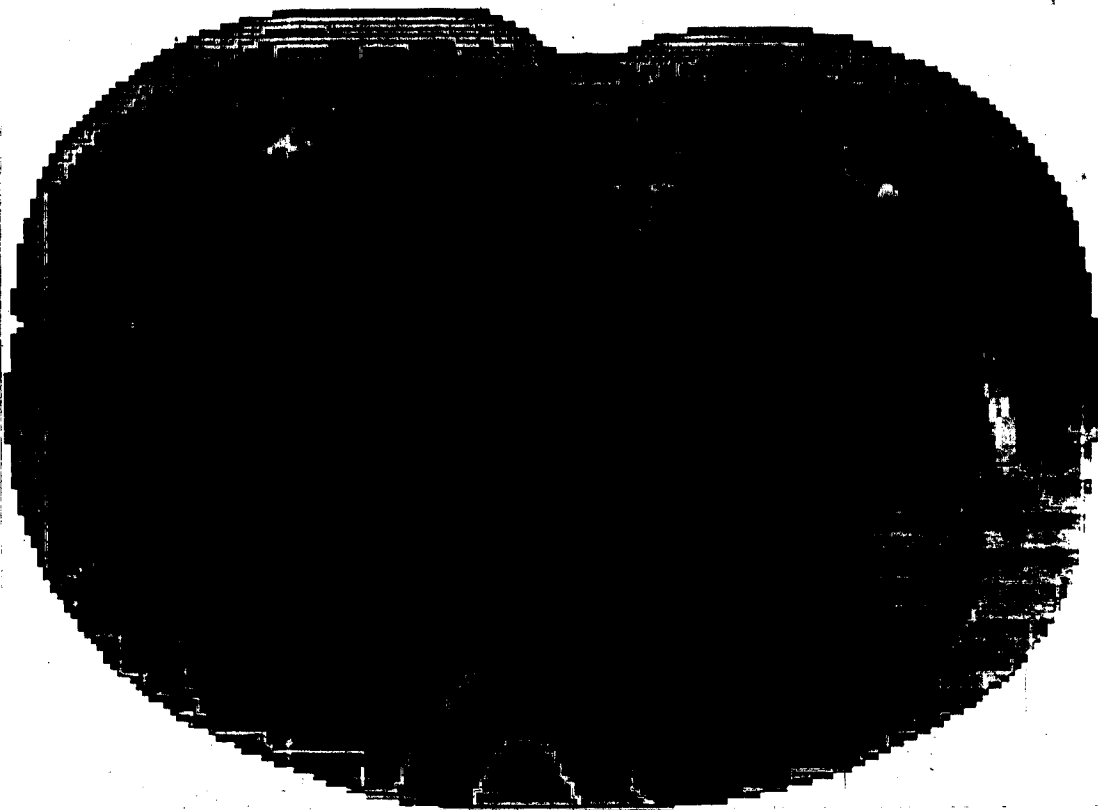
Fig. 3.27 The dose distribution in a CT scan of Rando
        slice 18 is shown. The inhomogeneity correction
        was performed using the equivalent TAR method (110)
        as implemented at the Ontario Cancer Institute.

values within 4% of the measured correction factors. This indicates that for the hemi-body treatment, doses within lung are obtained with reasonable accuracy using a simplified TMR method provided the correct internal dimensions and densities, as obtained on a CT scan, are entered. The detailed pixel-by-pixel correction method is therefore not essential for accurate dose calculation in hemi-body treatments. The Lulu and Bjarngard Batho correction performs as well as the simple scaled TMR. However, the generalized Batho method gives correction factors 2 to 3% lower than the other correction methods. This is expected since it does not account for the finite extent of the lungs. Therefore if the generalized Batho correction is used, one can expect doses in lung in the hemi-body irradiations to be underpredicted by roughly 6%. More accurate doses are obtained using any of the other methods. However, a pixel-by-pixel correction method is not essential. The simple scaled TMR yields doses with equal accuracy. This simple method could easily be implemented for dose calculations on a treatment planning computer. Then isodose distributions throughout the thorax can be obtained. The method can also be used manually to calculate doses at specified locations in the thorax. However, the accuracy of this method, as well as the other methods, depends on the accurate anatomical dimensions and densities obtained from CT scans. The influence of anatomical dimensions and densities on lung

dose calculations has been analysed in detail and discussed in several papers by Van Dyk ét al. (123,124,125) and has been found to be important. In summary, the use of a simple lung correction calculation in conjunction with correct specific anatomical dimensions and average density has been found to be sufficiently accurate for HBI protocols.

4. FUTURE WORK AND CONCLUSION

This thesis deals with radiation-induced damage to lung in large field irradiation. The incidence of radiation pneumonitis as a function of dose to lung in radiotherapy patients has been documented by Fryer (30) and Van Dyk (128). Recently, fractionated radiotherapy, which is more common in small field irradiations, is also being used for hemi-body irradiations (120). Chemotherapy may also be given to supplement the radiotherapy. Under these conditions, the response of lung as well as tumor will be different. Therefore dose response data for radiation pneumonitis need to be determined for these different conditions.

Corticosteroids and antibiotics have been found useful to treat certain aspects of the acute radiation pneumonitis syndrome, but its treatment remains an area of active research. When clinical symptoms of radiation pneumonitis develop, the patient experiences severe respiratory complications and the syndrome progresses rapidly and is potentially fatal. Intervention is then often "too little too late". One of the objectives of this thesis was to investigate a non-invasive test based on computed tomography (i.e. CT scans) which could be used as an early indicator of radiation damage to lung. In order for this test to be useful, it should indicate accurately the changes occuring in lung, preferably before

215

clinical symptoms occur. It should also be superior or at least as good as other non-invasive tests in terms of sensitivity and specificity. The mouse lung was first chosen to monitor radiation response using CT densitometry. The advantage of using mice is that a large number of animals can easily be studied. When animals of the same strain (which are often inbred) and age are used, differences in radiation response due to age or genetics are eliminated and good statistics are obtained. Moreover, the radiation changes in mouse lung are well documented in the literature. The severity of the changes as a function of dose as well as the development of these changes with time are known. Before embarking upon these experiments, however, the CT densitometry was tested with large and small objects and was found to be reliable for the study of mouse lungs (sections 2.1.5, 2.1.6, 2.1.7). Indeed, CT number changes observed in mouse lung corresponded to the time course of microscopic changes observed post-mortem. More severe changes were detected for those mice irradiated to the higher doses. Thus, dose response data can accurately be obtained using CT densitometry (section 2.2.2). This test could now be used to investigate other aspects of the radiation response of lung.

Most of the irradiated mice did not survive until the late phase of radiation damage. Data for this phase is therefore limited. Also it is not known whether mice with

less severe symptoms during the early phase are those
capable of recovering. CT densitometry experiments with
mice are now being carried out by Dr. G. Miller of the
Radiobiology Group to study the later phases of lung
damage. These mice are irradiated to lower doses and are
expected to survive the acute phase of damage. Dr.
Miller is also studying the effect of radiation protector
drugs. Rats with a lung volume approximately ten times
larger than that of mice might also be considered (section
2.2.3.3).

Once CT densitometry was established as an accurate
indicator of radiation response in lung, the second phase
of our experiments was to compare the usefulness of this
test to other in-vivo tests. For these experiments, dogs,
with a larger lung volume, were more useful (section 2.3).
CT densitometry was compared to conventional X-ray raphy
and two nuclear medicine tests (section 2.3.3 The
objective was to determine which of these tests was the
earliest indicator of radiation damage to lung. In this
respect, conventional X-radiography was inferior to all
tests closely followed by the macroaggregated albumin
perfusion test. CT changes were observed two weeks
earlier, and changes in radioaerosol clearance from lung
was the earliest indicator of radiation response.
However, the ultimate goal of these tests is to apply them
to radiotherapy patients. Often in these patients
radiation effects are superimposed on recurrent tumor

growth. This will be difficult to distinguish from radiation changes if a radioaerosol clearance test is being used. However, if a pre-irradiation CT scan is available, the location of the tumor can be noted. Then, on subsequent scans, a solid tumor can be distinguished from radiation changes and changes due to radiation alone can be quantified. However, for a diffuse tumor, differentiation of radiation change from tumor is more difficult. Nevertheless the merit of the CT scan as an accurate and early indicator of radiation change in lung is not to be underestimated. Another advantage of the CT scan is that it is a quicker procedure (15 min.) as compared to 40 minutes or longer for the radioaerosol scan. In the above experiments the dogs were sacrificed as soon as all tests showed abnormality. Thus, the correlation of the early effects with later effects during pneumonitis could not be determined. This could be the basis of a future study where there should be longer-term follow-up to the late phases. At present, however, the tests detecting radiation damage in the "prepneumonitis" phase are of limited value since no therapeutic agent exists that will modify the radiation reaction. On the other hand, there is no incentive to investigate such therapeutic agents as long as it is not known where and when to intervene. The pathogenesis of radiation pneumonitis as well as therapeutic agents to modify this syndrome are areas of active basic research. For these

studies, an early test for radiation response would be a valuable tool. This test should be non-invasive so that it can ultimately be employed in the follow-up of radiotherapy patients.

The CT densitometry test, as well as the nuclear medicine test still need to be investigated under a variety of conditions. Clinical trials are also necessary in patients with and without tumor in lung. The new imaging modality NMR (Nuclear Magnetic Resonance) may offer promise in the detection of edema in lung. Besides its imaging capability, NMR has the potential to detect in-vivo chemistry due to its ability to identify the structure and properties of complex molecules (138). NMR can thus not only aid in diagnosis, but may detect the molecular changes leading to radiation pneumonitis and may thus point to the underlying cause and process of the syndrome. This method applied to medicine is still in its infancy and its clinical value and potential remain to be explored.

Finally, in this work, the usefulness of the CT densitometry test was investigated in clinical situations. CT scans of radiotherapy patients irradiated with a high local dose to lung, or a lower dose to the entire lung (hemi-body irradiation) were analysed to obtain density information for diagnostic purposes (section 2.4). Average densities obtained for our patients' lungs excluding the diseased regions agree well with the

published values (129). In the patients receiving a high
local dose to lung CT number changes indicated radiation
changes and/or tumor volume changes. In the patients
receiving hemi-body irradiation no density increases were
observed, as expected for dose delivered (6 Gy in 8
fractions). This study is ongoing with a new group of
patients irradiated to higher dose levels.

Although radiation pneumonitis will not be fatal if
only a small part of the lung is irradiated, those
patients who have a smaller volume of lung irradiated
receive much higher localized doses. In these cases, the
area of irradiation is well defined; CT scan can be used
to obtain dose response data at such sites. In such
cases, an accurate dose distribution should be computed
using CT scans (11,125,130). This data can also be
obtained for fractionated radiation. If accurate dose
response data are available for all these clinical
situations, then dose to lung can be increased to achieve
a greater therapeutic gain. This presupposes of course
that dose can be accurately calculated and delivered to
lung. Chapter 3 of this thesis therefore deals with lung
dose calculations.

The existence of a low density material such as lung
in unit-density tissue alters the dose to points within
and beyond lung in a complicated way. The primary as well
as the scattered radiation is affected. Lung dose
calculation algorithms are often crude, accounting only

for primary changes in dose caused by the inhomogeneity. However, inaccuracies in delineation of inner anatomical contours and densities can introduce greater errors. With CT scanning the possibility exists to obtain the correct internal geometry and densities of tissue structures. The accuracy of lung dose calculations is now limited by the accuracy of the calculation algorithms and much research is being devoted to improve these (21,69,71,110,141).

In this thesis, application of the lung dose calculation methods to large field irradiations is discussed. The simple calculation algorithms as well as a more complex "pixel-by-pixel" dose correction method was tested. Depending upon the type of radiation and the complexity of the phantom, these methods may perform well in one situation but not in another. Electron transport becomes a problem with higher energy beams. None of the simple inhomogeneity correction methods account for changes in electron transport at the interface of two media. Monte Carlo and ray-tracing (or convolution) complex computer calculations can overcome this limitation.

Methods such as the simple ratio of TAR's (effective SSD) (21) which only account for changes in primary radiation are not sufficiently accurate even in simple situations (section 3.4). Methods which indirectly account for change in scatter such as the Batho method (109) perform very well, and (surprisingly) better than

pixel-by-pixel correction methods (equivalent TAR) in the simple geometries, giving agreement with measured values within and beyond lung to 2%. This method, however, does not account for a situation where the lateral extent of the inhomogeneity is smaller, than the radiation field size, and does not perform well in these more complex situations. For such cases the "pixel-by-pixel" equivalent TAR method (107,110) senses this situation and gives better agreement with measured values. If the Batho method is modified as proposed by Lulu and Bjarngard (69) to account for the lateral extent of the inhomogeneity, agreement is within 4% for complex situations (section 3.6). A simple scaled TMR method developed during this work, gives agreement to within 3%.

For the 6 MV X-rays used in our experiments the region of electron disequilibrium extends over 1.5 cm in unit-density material. Thus, there will be inaccuracies in dose calculation near the interface of two media. However, this region is not large enough to warrant use of Monte Carlo or ray tracing methods. At present, use of these methods cannot be contemplated in hemi-body irradiations due to the time involved (section 3.2).

Finally, dose calculations were performed for a humanoid phantom (RANDO). This phantom was irradiated using the same set-up as for the hemi-body patients (section 3.7). Calculated doses were compared to measured doses. In this complex configuration, dose computations

performed using the equivalent TAR method, the Lulu and Bjarngard version of the Batho method and the scaled TMR all gave good agreement with measured values within and out of lung (±4%). For all these calculations, anatomic information was obtained from CT scans. With this correct information even the simpler inhomogeneity correction methods yield dose calculations with 4% accuracy in hemi-body irradiations.

The work reported in this thesis, has validated computed tomography as a valuable tool for both radiotherapy planning and diagnostic follow-up. In the protocol for the hemi-body irradiations at the Cross Cancer Institute the total dose to lung was kept at 6 Gy. This dose was prescribed to mid-lung assuming unit-density for lung. Such a calculation, where the density of lung is not considered will underpredict the dose by more than 10% at some locations in lung. The correction factor at mid-lung in RANDO slice 18 is 1.073 calculated using the equivalent TAR method. The dose at this position would therefore be 6.44 Gy as compared to 6 Gy prescribed to this point by the CCI hemi-body irradiation protocol. Subsequent to the present work, dose at any point in lung can be calculated with 4% accuracy.

REFERENCES

1. Aget, H., Van Dyk, J., Leung, P.M.K.: Utilization of a high energy photon beam for whole body irradiation. Radiology 123: 747-751, 1977.

2. Ambrose, J.: Computerized transverse axial scanning (tomography). II. Clinical application. Br. J. Radiol. 46: 1023-1047, 1973.

3. Atomic Energy of Canada, Ottawa, Canada; Manual for TP-11 treatment planning system, 1980.

4. Attix, F.H., Roesch, W.C., Tochilin, E.: Radiation dosimetry Vol. II., Academic Press 1966.

5. Bagne, F.: A method for calculating megavoltage X-ray dose and dose parameters. Med. Phys. 7: 664-671, 1980.

6. Barrett, A.: Total body irradiation (TBI) before bone marrow transplantation in leukemia: a co-operative study from the European group for bone marrow transplantation. Br. J. Radiol. 55: 562-567, 1982.

7. Batho, H.F.: Lung corrections in cobalt-60 beam therapy. J. Can. Assoc. Radiol. 15: 79-83, 1964.

8. Battista, J.J.: Radiotherapy planning computers: To buy or not to buy? Course on "Computation in Radiation Therapy" Canadian College of Medical Physics, June 23, 1983. Quebec City, Que.

9. Battista, J.J., Bronskill, M.J.: Compton scatter imaging of transverse sections: an overall appraisal and evaluation for radiotherapy planning. Phys. Med. Biol. 26: 81-99, 1981.

10. Battista, J., Meeker, B., Chapman, D., Castor, W.: Animal tumor volume and density by CT. J. Comput. Assist. Tomogr. 4: 714, 1980.

11. Battista, J.J., Rider, W.D., Van Dyk, J.: Computed tomography for radiotherapy planning. Int. J. Radiation Oncology Biol. Phys. 6: 99-107, 1980.

12. Battista, J.J., Van Dyk, J.: CT-aided radiotherapy planning with emphasis on dose calculations in three dimensions. Chapter 39, Computerized Tomographic Scanners in Radiotherapy in Europe. Br. J. of Radiol. Supplement 15, 1981.

13. Beaudoin, L.: M.Sc. thesis, University of Toronto, 1968.

14. Bennet, D.E., Million, R.R., Ackerman, L.V.: Bilateral radiation pneumonitis, a complication of the radiotherapy of bronchogenic carcinoma. (Report and analysis of seven cases with autopsy). Cancer 2: 1001-1018, 1969.

15. Bracewell, R.N.: Strip integration in radioastronomy. Aust. J. Phys. 9: 198-217, 1956.

16. Brooks, R.A., DiChiro, G.: Principles of computer assisted tomography (CAT) in radiographic and radioisotopic imaging. Phys. Med. Biol. 21:689-732, 1976.

17. Bruce, W.R., Johns, H.E.: The use of the Monte Carlo method. Section II, Br. J. Radiol. Supplement 9, 1960.

18. Cormack, A.M.: Representation of a function by its line integrals, with some radiological applications. J. Appl. Phys. 34: 2722-2727, 1963.

19. Cormack, A.M.: Representation of a function by its line integrals with some radiological applications. II. J. Appl. Phys. 35: 2908-2913, 1964.

20. Cunningham, J.R.: Scatter-air ratios. Phys. Med. Biol. 17: 42-51, 1972.

21. Cunningham, J.R.: Current and future development of tissue inhomogeneity corrections for photon beam clinical dosimetry with the use of CT. Computed tomography in radiation therapy, edited by C.C. Ling, C.C. Rogers, and R.J. Morton, Raven Press, New York, 1983.

22. De Rosier, D.J., Klug, A.: Reconstruction of three-dimensional structures from electron micrographs. Nature 217: 130-134, 1968.

23. Dohring, W.: Quantitative analyses of regional pulmonary ventilation using Compton densitometry and computed tomography. Prog. Resp. Res. 11: 48-75 (Karger, Basel 1979).

24. Down, J.D., Steel, G.G.: The expression of early and late damage after thoracic irradiation: A comparison between CBA and C57Bl strains of mice. (in press).

25. El-Khatib, E., Sharplin, J., Battista, J.: Density of mouse lung in vivo following X-irradiation. Int. J. Radiation Oncology Biol. Phys. 9: 853-858, 1983.

26. Faw, F., Glenn, D.: Dose distribution if the field is larger than the patient. Presented at the third meeting of the International Organization of Medical

Physics, Gothenberg, Sweden, 1972.

27.   Fitzpatrick,   P.J.,   Rider,   W.D.:   Half-body
radiotherapy.   Int.   J.   Radiation Oncology Biol.   Phys.
1:   197-207, 1976.

28.   Fowler,   J.F.,   Travis,   E.L.:   The   radiation
pneumonitis syndrome in half- body radiation therapy.
Int. J. Radiation Oncology Biol. Phys. 4:   1111-1113,
1978.

29.   Freedman,   G.S.,   Lofgren,   S.B.,   Kligerman,   M.M.:
Radiation-induced   changes   in   pulmonary   perfusion.
Radiology 112:   435-437, 1974.

30.   Fryer, C.J.H., Fitzpatrick, P.J., Rider, W.D.,   Poon,
P.:   Radiation pneumonitis: Experience following a large
single dose of radiation.   Int.   J.   Radiation Oncology
Biol. Phys. 4:   931-936, 1978.

31.   General   Electric   publication.   Introduction   to
computed tomography.

32.   Glasgow, G.P.:   The dosimetry of fixed, single source
hemibody   and   total   body   irradiators.   Med.   Phys.   9:
311-323, 1982.

33.   Gordon, R., Bender, R., Hermann, G.T.:   Algebraic
reconstruction   techniques   (ART)   for   three-dimensional
electron microscopy and X-ray photography.   J.   Theor.
Biol. 29:   471-481, 1970.

34.   Gordon,   R.,   Herman,   G.T.,   Johnson,   S.A.:   Image
reconstruction   from projections.   Sci.   Am.:   56-58, Oct.
1975.

35.   Gross, N.J.:   Pulmonary effects of radiation therapy.
Annals of Internal Medicine 86:   81-92, 1977.

36.   Gross,   N.J.:   Experimental   radiation   pneumonitis:
Changes in physiology of the alveolar surface.   J.   Lab.
Clin. Med. 92: 991-1001, 1978.

37. Gross, N.J.:   Experimental radiation pneumonitis.
III.   Phospholipid studies on the lungs.   J.   Lab.   Clin.
Med. 93, 627-637, 1979.

38.   Gross, N.J.:   The pathogenesis of radiation-induced
lung damage.   Lung 159: 115-125, 1981.

39. Gur, D., Drayer, B.P., Borovetz, H.S., Griffith,
B.P., Hardesty, R.L., Wolfson, S.K.: Dynamic computed
tomography of the lung: Regional ventilation
measurements. J. Comput. Assist. Tomogr. 3:   749-753,

1979.

40. Hedlund, L.W., Effmann, E.L., Bates, W.M., Beck, J.W., Goulding, P.L., Putman, C.E.: Pulmonary edema: A CT study of regional changes in lung density following oleic acid injury. J. of Comput. Assist. Tomogr. 6: 939-946, 1982.

41. Hedlund, L.W., Jones, D.P., Effmann, E.L., Johnson, G.A., Bates, W.M., Beck, J.W., Wolfe, W., Putman, C.E.: A computed tomographic study of the dog lung during hemorrhagic shock and after rescuscitation. Investigative Radiology 16: 466-472, 1981.

42. Hedlund, L.W., Vock, P., Effmann, E.L.: Evaluating lung density by computed tomography. Seminars in Respiratory Medicine 5: 76-88, 1983.

43. Henkelman, R.M., Wong, J.W.: Physics of the inhomogeneity problem and the present status of clinical dosimetry. Computed tomography in radiation therapy edited by C.C. Ling, C.C. Rogers, and R.J. Morton, Raven Press, New York, 1983.

44. Herbert, D.L., Gur, D., Chabason, L., Good, W.F., Rinaldo, J.E., Snyder, J.V., Borovetz, H.S., Mancici, M.C.: Mapping of human lo   pulmonary ventilation by Xenon enhanced computed   raphy. J. of Comput. Assist. Tomogr. 6:1088-109   82.

45. Herman, H.J., Wetzel, E., Heller, M., Hofmann, W.: Vergleichende Untersuchungen (Computertomographie, Roentgendiagnostik, Szintigraphie) zum Nachweis strahlenbedingter Veranderungen der Lunge. Strahlentherapie 156: 248-252, 1980.

46. Holt, J.G., Laughlin, J.S., Moroney, J.P.: Extension of the concept of tissue-air ratios (TAR) to high energy X-ray beams. Radiology 96: 437- 446, 1970.

47. Hounsfield, G.N.: Computerized transverse axial scanning (tomography). I. Description of system. Br. J. Radiol. 46: 1016-1022, 1973.

48. Hubbell, J.H.: Photon cross sections, attenuation coefficients, and energy absorption coefficients from 10 keV to 100 GeV, NSRDS-NBS 29, U.S. GPO, Washington DC 1969.

49. ICRU Report 14, Radiation dosimetry: X-rays and gamma rays with maximum photon energies between 0.6 and 50 MeV, 1969.

50. ICRU Report 21, Radiation dosimetry: Electrons with

initial energies between 1 and 50 MeV, 1972.

51. ICRU Report 23, Measurement of absorbed dose in a phantom irradiated by a single beam of X or gamma rays, 1973.

52. Jennings, F.L., Arden, A.: Development of experimental radiation pneumonitis. Arch. Pathol. 71: 437-446, 1961.

53. Johns, H.E., Battista, J., Bronskill, M.J., Brooks, R., Fenster, A., Yaffe, M.: Physics of CT scanners: Principles and problems. Int. J. Radiation Oncology Biol. Phys. 3: 45-51, 1977.

54. Johns, H.E., Cunningham, J.R.: The Physics of Radiology, Fourth Edition, Thomas, Springfield, Illinois, 1983.

55. Judy, P.F., Balter, S., Bassano, D., McCullough, E.C., Payne, J.T., Rothenberg: AAPM Report No. 1: Phantoms for performance evaluation and quality assurance of CT scanners. 1977.

56. Kappas, K., Rosenwald, J.C.: Inhomogeneity corrections when lateral dimensions are smaller than field dimensions. Abstract in World Congress on Medical Physics and Biomedical Engineering 1982, Hamburg.

57. Karzmark, C.J., Morton, R.J.: A primer on theory and application of linear accelerators in radiation therapy. HHS Publication (FDA) 82-8181, Dec. 1981.

58. Khan, F.M., Sewchand, W., Lee, J., Williamson, J.F.: Revision of tissue-maximum ratio and scatter-maximum ratio concepts for Cobalt-60 and higher energy X-ray beams. Med. Phys. 7:230-237, 1980.

59. Kim, T.H., Khan, F.M., Galvin, J.M.: A report of the work party: Comparison of total body irradiation techniques for bone marrow transplantation. Int. J. Radiation Oncology Biol. Phys. 6: 779-784, 1980.

60. Koehler, P.R., Anderson, R.E., Baxter, B.: The effect of computed tomography viewer controls on anatomical measurements. Radiology 130: 189-194, 1979.

61. Kuhl, D.E., Edwards, R.Q.: Image separation radioisotope scanning. Radiology 80:653-661, 1963.

62. Lanzl, L.H.: The Rando phantom and its medical applications. 1973.

63. Law, M.P., Hornsey, S., Field, S.B.: Collagen

content of lungs of mice after X-ray irradiation. Radiat. Res. 65: 60-70, 1976.

64. Levi, C., Gray, J.E., McCullough, E.C., Hattery, R.R.: The unreliability of CT numbers as absolute values. AJR 139: 443-447, 1982.

65. Libshitz, H.I., North, L.B.: Diagnostic roentgenology of radiotherapy change. Lung, Chapter 3, pp.33-46. The Williams and Wilkins Company, 1979.

66. Lillicrap, S.C., Burns, J.E., Greene, D., Williams, P.C.: Revised code of practice for the dosimetry of 2 to 25 MV X-ray, and of Caesium-137 and Cobalt-60 gamma ray beams. Phys. Med. Biol. 28: 1097-1104, 1983.

67. Lillicrap, S.C., White, D.R., Bradshaw, A.I., Greatorex, C.A., Innes, G.S., Rees, D.J., Twiss, D.H., Williams, P.C.: Phantom materials for photons and electrons. The Hospital Physicists' Association Radiotherapy Topic Group. 1977.

68. Liu, J.W., Shen, Y.: Chinese herb medicine HH-6075, in radiation pneumonitis and pulmonary fibrosis. II. Electron microscopic studies. Proceedings of the seventh International Congress of Radiation Research, Amsterdam, July 3-8, 1983.

69. Lulu, B.A., Bjarngard, B.E.: Batho's correction factor combined with scatter summation. Med. Phys. 9: 372-377, 1982.

70. Lulu, B.A., Bjarngard, B.E.: A derivation of Batho's correction factor for heterogeneities. Med. Phys. 9: 907-909, 1982.

71. Mackie, T.R.: Photon dose calculation using a convolution method that includes non-local electron energy deposition. Med. Phys. 10: 536, 1983.

72. Mackie, T.R., Scrimger, J.W.: Contamination of a 15 MV photon beam by electrons and scattered photons. Radiology 144: 403-409, 1982.

73. Maisin, J.R.: The ultrastructure of the lung of mice exposed to a supra-lethal dose of ionizing radiation on the thorax. Radiat. Res. 44: 545-564, 1970.

74. Masterson, M.E., Thomason, C.L., McGary, R., Hunt, M.A., Simpson, L.D., Miller, D.W., Laughlin, J.S.: Dependence of the computerized tomography (CT) number-electron density relationship on patient size and X-ray beam filtration for fan beam CT scanners. SPIE 273: Application of optical instrumentation in medicine IX,

1981.

75. McCullough, E.C.: Photon attenuation in computed tomography. Med. Phys. 2: 307-320, 1975.

76. Miller, G., Scott, P., Sieman, D.: Immonuhistochemical assessment of the role of extracellular matrices in the expression of damage in irradiated mouse lung. Abstract in the proceedings of the 7th Int. Congress of Radiation Research, Amsterdam, July 3-8, 1983.

77. Moosavi, H., McDonald, S., Rubin, P., Cooper, R., Stuard, I.D., Penney, D.: Early radiation dose-response in lung: An ultrastructural study. Int. J. Radiation Oncology Biol. Phys. 2: 921-931, 1977.

78. Moss, W.T., Haddy, F.J., Sweany, S.K.: Some factors altering the severity of acute radiation pneumonitis: Variation with Cortisone, Heparin, and Antibiotics. Radiology 75: 50-54, 1960.

79. Nabawi, P., Mantravadi, R., Breyer, D., Capek, V.: Computed tomography of radiation-induced lung injuries. J. Comput. Assist. Tomogr. 5: 568-570, 1981.

80. O'Connor, J.E.: The variation of scattered X-rays with density in an irradiated body. Phys. Med. Biol. 1: 352-369, 1957.

81. Oldendorf, W.H.: Isolated flying spot detection of radiodensity discontinuities displaying the internal structural pattern of a complex object. IRE Trans. Biomed. Elect. BME 8: 68-72, 1961.

82. Parker, R.P., Hobday, P.A., Cassel, K.J.: The direct use of CT numbers in radiotherapy dosage calculations for inhomogeneous media. Phys. Med. Biol. 24: 802-809, 1979.

83. Peters, L.: Discussion: The radiobiological bases of TBI. Int. J. Radiat. Oncology Biol. Phys. 6: 785-787, 1980.

84. Peters, L.J., Withers, H.R., Jackson, H.C., Dicke, K.A.: Radiobiological considerations in the use of total-body irradiation for bone marrow transplantation. Radiology 131: 243-247, 1979.

85. Phelps, M.D., Gado, M.H., Hoffman, E.J.: Correlation of effective atomic number and electron density with attenuation coefficients measured with polychromatic X-rays. Radiology 117: 585-588, 1975.

86. Prato, F.: The development of pulmonary radiation fibrosis in man. Ph.D. thesis, University of Toronto, 1976.

87. Radon, J.: On the determination of functions from their integrals along certain manifolds. Ber. Saech. Akad. Wiss. Leipzig Math. Phys. Kl. 60:262-277, 1917.

88. Raeside, D.E.: Monte Carlo principles and applications. Phys. Med. Biol. 21: 181-197, 1976.

89. Rider, W.D.: C.T. X-ray measurement of lung density. Int. J. Radiation Oncology Biol. Phys. 6: 956, 1980.

90. Rinderknecht J., Shapiro, L., Krauthammer, M., Taplin, G., Wasserman, K., Uszler, J.M., Effros, R.M.: Accelerated clearance of small solutes from the lungs in interstitial lung disease. Am. Rev. of Respiratory Disease 121: 105- 117, 1980.

91. Robinson, P.J., Kreel, L.: Pulmonary tissue attenuation with computed tomography: Comparison of inspiration and expiration scans. J. of Comput. Assist. Tomogr. 3: 740-748, 1979.

92. Rosenblum, L.J., Mauceri, R.A., Wellenstein, D.E., Bassano, D.A., Cohen, W.N., Heitzman, E.R.: Computed tomography of the lung. Radiology 125:521-524, 1978.

93. Rosenblum, L.J., Mauceri, R.A., Wellenstein, D.E., Thomas, F.D., Bassano, D.A., Raasch, B.N., Chamberlain, C.C., Heitzman, E.R.: Density patterns in the normal lung as determined by computed tomography. Radiology 137: 409-416, 1980.

94. Rothschild, A.M., Castania, A.: Contribution of vasopressor and plasma kininogen changes towards acute adrenaline pulmonary edema in the rat. Naunyn-Schmiedeberg's Arch. of Pharmacology 295: 177-181, 1976.

95. Rubin, P., Casarett, G.W.: Clinical Radiation Pathology. Saunders, Philadelphia, 1968.

96. Rubin, P., Shapiro, D.L., Finkelstein, J.N., Penney, D.P.: The early release of surfactant following lung irradiation of alveolar type II cells. Int. J. Radiation Oncology Biol. Phys. 6: 75-77, 1980.

97. Rubin, P., Sieman, W., Shapiro, D.L., Finkelstein, J.N., Penney, D.P.: Surfactant release as an early measure of radiation pneumonitis. Int. J. Radiat. Oncology Biol. Phys. 9: 1669-1673, 1983.

98.   Rubin, P., Sieman, D., Shapiro, D., Finkelstein, J., Penney, D., Gregory, P.:   Dose-effect relationship for surfactant alveolar levels after pulmonary irradiation. Int.   J. Radiation Oncology Biol. Phys. 6: 1359-1360, 1980.

99.   Sahebjami, H., Vassalo, C.L.: Effects of starvation and refeeding on lung mechanics and morphometry. Am. Rev. of Respiratory Disease 119: 443- 451, 1979

100. Salazar, O.M., Rubin, P., Keller, B., Scarantino, C.: Systemic (Half-body) radiation therapy: Response and toxicity. Int. J. Radiation Oncology Biol. Phys. 4: 937-950, 1978.

101. Scrimger, J., Kolitsi, Z.: Scattered radiation from beam modifiers used with megavoltage therapy units. Radiology 130: 233-236, 1979.

102. Sharplin, J., Franko, A.J.: Irradiation of mouse lungs causes a dose-dependent increase in lung weight. Int. J. Radiation Oncology Biol. Phys. 8: 1065-1069, 1982.

103. Shen, Y., Liu, J.W., Li, T.H.: Chinese herb medicine HH-6075, in radiation pneumonitis and pulmonary fibrosis. I. Preliminary report on animal experiment. Abstract in Proceedings of the seventh International Congress of Radiation Research. Amsterdam. July 3-8, 1983.

104. Shrivastava, P.N., Hans, L., Concannon, J.: Changes in pulmonary compliance and production of fibrosis in X-irradiated lungs of rats. Radiology 112: 439-440, 1974.

105. Sieman, D.W., Hill, R.P., Bush, R.S.: Analysis of blood gas values in mice following pulmonary irradiation. Radiat. Res. 81: 303-310, 1980.

106. Sieman, D.W., Hill, R.P., Penney, D.P.: Early and late pulmonary toxicity in mice evaluated 180 and 420 days following localized lung irradiation. Radiat. Res. 89: 396-407, 1982.

107. Sontag, M.R.: Ph.D. thesis, University of Toronto, 1979.

108. Sontag, M.R., Battista, J.J., Bronskill, M.J., Cunningham, J.R.: Implications of computed tomography for inhomogeneity corrections in photon beam dose calculations. Radiology 124: 143-149, 1977.

109. Sontag, M.R., Cunningham, J.R.: Corrections to

absorbed dose calculations for tissue inhomogeneities.
Med. Phys. 4: 431-436, 1977.

110. Sontag, M.R., Cunningham, J.R.: The equivalent
tissue-air ratio method for making absorbed dose
calculations in a heterogeneous medium. Radiology. 129:
787-794, 1978

111. Sutharalingam, J.R., Kenney, G.N.:
Thermoluminescent dosimetry TLD, U. of Wisconsin Press,
1968.

112. Suzuki, A., Suzuki, M.N.: Use of a pencil-shaped
ionization chamber for measurement of exposure resulting
from a computed tomography scan. Med. Phys. 5:
536-539, 1978.

113. Tatcher, M., Palti, S.: Evaluation of density
correction algorithms for photon beam dose calculations.
Radiology 141: 201-205, 1981.

114. Tatcher, M., Palti, S.: A simple equivalent
tissue-air ratio method for calculating absorbed dose in a
heterogeneous medium. Radiology 146: 527-529, 1983.

115. Teates, D., Cooper, G.: Some consequences of
pulmonary irradiation. A second long term report. Am.
J. Roentgenol. 96: 612-619, 1966.

116. Travis, E.: The sequence of histological changes in
mouse lungs after single doses of X-rays. Int. J.
Radiation Oncology Biol. Phys. 6: 345-347, 1980.

117. Travis, E.L.: Early indicators of radiation injury
in the lung: Are they useful predictors for late changes?
Int. J. Radiation Oncology Biol. Phys. 6: 1267-1269,
1980.

118. Travis, E.L., Down, J.D., Holmes, S.J., Hobson, B.:
Radiation pneumonitis and fibrosis in mouse lung assayed
by respiratory frequency and histology. Radiat. Res.
84: 133-143, 1980.

119. Travis, E.L., Vojnovic, B., Davies, E.E., Hirst,
D.G.: A plethysmographic method for measuring function in
locally irradiated mouse lung. Br. J. Radiol. 52:
67-74, 1979.

120. Urtasun, R.C.: Hemibody irradiation technique: A
wider use in oncology. Int. J. Radiation Oncology Biol.
Phys. 9: 1585-1586, 1983.

121. Urtasun, R.C., Belch, A., Bodnar, D.: Hemibody
Radiation, an active therapeutic modality for the

management of patients with small cell lung cancer. Int. J. Radiation Oncology Biol. Phys. 9: 1575-1578, 1983.

122. Urtasun, R.C., Belch, A.R., McKinnon, S., Higgins, E., Saunders, W., Feldstein, M.: Small-cell lung cancer initial treatment with sequential hemi-body irradiation vs 3-drug systemic chemotherapy. Br. J. Cancer 46: 228-235, 1982.

123. Van Dyk, J.: Lung dose calculations using computerized tomography: Is there a need for pixel based procedures? Int. J. Radiation Oncology Biol. Phys. 9: 1035-1041, 1983.

124. Van Dyk, J.: Magna-field irradiation: Physical considerations. Int. J. Radiation Oncology Biol. Phys. 9: 1913-1918, 1983.

125. Van Dyk, J., Battista, J.J., Rider, W.D.: Half-body radiotherapy: The use of computed tomography to determine the dose to lung. Int. J. Radiation Oncology Biol. Phys. 6: 463-470, 1980.

126. Van Dyk, J., Battista, J.J., Rider, W.D.: The Use of computed tomography in lung dose calculations for upper half-body irradiations. Chapter 25, Computerized Tomographic Scanners in Radiotherapy in Europe. Br. J. Radiol. Supplement 15, 1981.

127. Van Dyk, J., Hill, R.P.: Post-irradiation lung density changes measured by computerized tomography. Int. J. Radiation Oncology Biol. Phys. 9: 847- 852, 1983.

128. Van Dyk, J., Keane, T.J., Kan, S., Rider, W.D., Fryer, C.J.H.: Radiation pneumonitis following large single dose irradiation: A re-evaluation based on absolute dose to lung. Int. J. Radiation Oncology Biol. Phys. 7: 461-467, 1981.

129. Van Dyk, J., Keane, T.J., Rider, W.D.: Lung density as measured by computerized tomography: Implications for radiotherapy. Int. J. Radiation Oncology Biol. Phys. 8: 1363-1372, 1982.

130. Van Dyk, J., Leung, M.K., Cunningham, J.R.: Dosimetric considerations of very large Cobalt-60 fields. Int. J. Radiation Oncology Biol. Phys. 6: 753-759, 1980.

131. Vatnitskij, S.M., Aalto, P.K., Rannikko, S.J.: Tissue-air ratios for cobalt 60 therapy units. Br. J. of Radiol. 56: 315-319, 1983.

132. Wara, W.M., Phillips, T.L., Margolis, L.W., Smith,

V.: Radiation pneumonitis: A new approach to the derivation of time-dose factors. Cancer 32: 547-552, 1973.

133. Webb, S., Fox, R.A.: Verification by Monte Carlo methods of a power law tissue-air ratio algorithm for inhomogeneity corrections in photon beam dose calculations. Phys. Med. Biol. 25:225-240, 1980.

134. Webb, S., Parker, R.P.: A Monte Carlo study of the interaction of external beam X-radiation with inhomogeneous media. Phys. Med. Biol. 23: 1043-1059, 1978.

135. Webber, C.E., Coates, G.: A clinical system for the in-vivo measurement of lung density. Med. Phys. 9: 473-477, 1982.

136. Wegener, O.H., Koeppe, P., Oeser, H.: Measurement of lung density by computed tomography. J. of Comput. Assist. Tomogr. 2: 263-273, 1978.

137. White, D.R.: The photon attenuation and absorption properties of clear and white polystyrene. Br. J. of Radiol. 51: 397-398, 1978.

138. Witcofski, R.L., Karstaedt, N., Partain, C.L., Editors: NMR Imaging. Proceedings of an International Symposium on Nuclear Magnetic Resonance Imaging. The Bowman Gray School of Medicine of Wake Forest University, Winston-Salem, NC. Oct. 1-3, 1981.

139. Wong, J.W., Henkelman, R.M.: Reconsideration of the power-law (Batho) equation for inhomogeneity corrections. Med. Phys. 9: 521-530, 1982.

140. Wong, J.W., Henkelman, R.M., Fenster, A., Johns, H.E.: Second scatter contribution to dose in a Cobalt-60 beam. Med. Phys. 8: 775-782, 1981.

141. Wong, J.W., Rosenberger, F.U.: Photon dose calculations in radiotherapy treatment planning. Canadian College of Physicists in Medicine, Proceedings of Symposium "Computation in Radiation Therapy", Quebec City, June 23, 1983.

142. Young, M.E.J., Gaylord, J.D.: Experimental tests of corrections for tissue inhomogeneities in radiotherapy. Br. J. Radiology 43: 349-355, 1970.

143. Young, M.E.J., Kornelson, R.O.: Dose corrections for low-density tissue inhomogeneities and air channels for 10 MV X-rays. Med. Phys. 10: 450-455, 1983.

APPENDIX

PROGRAM SINGLEFOR

Ellen El-Khatib

June 17/83

This program calculates the dose due to first scatter
from two separate slabs of a phantom.

```
real*4        pi,rsq,elecm3,hn,lm,x1,x2,field,TAND,COSD,SIND
Parameter(PI=3.1416)
Parameter(elecm3=3.343E23)
Parameter(rsq=7.941E-26)
type*,'Please enter primary linear attenuation coefficient
1    (cm-1):'
accept*,xmuo
sum1=0.0
sum2=0.0
type*,'Please enter primary energy (Mev):'
accept*,hno
alo=hno/0.511
type *,' Please enter the field diameter (cm):'
accept *, field
type*,'Please enter distance from surface to probe x1 (cm):'
accept*,x1
type*,'Please enter thickness of lower layer x2 (cm):'
accept*,x2
type*,'Please enter electron density relative to
1    water of second layer'
```

```
accept*,ro3

do   a=0.0,179.0,0.01

    ct=COSD(a)

    al=alo/(1+alo*(1-ct))

    hn=al*0.511

hn is the energy of the once scattered photon/


Differential Probability

    cm=1-ct

    cp=1+ct*ct

    tem=cp*1.0/((1+alo*cm)*(1+alo*cm))

    tem=tem*(1+alo*alo*cm*cm/((1+alo*cm)*cp))

    dsig=(rsq/2.0)*tem



Integral Probability
    temp=(2*(1+al)/(1+2*al)-ALOG(1+2*al)/al)*

1   (1+al)/(al*al)

    temp=temp+ALOG(1+2*al)/(2*al)-

1   (1+3*al)/(1+2*al)/(1+2*al)

linear attenuation coefficient of the once scattered photon

    xmul=temp*rsq*2.0*PI*elecm3



integral energy transfer coefficient
    temtr=2*(1+al)*(1+al)/(al*al*(1+2*al))-(1+3*al)/

1   (1+2*al)/(1+2*al)

    temtr=temtr+(1+al)*(1+2*al-2*al*al)/

1   (al*al*(1+2*al)*(1+2*al))

    temtr=temtr-4*al*al/(3*(1+2*al)*(1+2*al)*(1+2*al))
```

```
      temtr=temtr-((1+al)/(al*al*al)-1/(2*al)+1/
1     (2*al*al*al))*ALOG(1+2*al)
```

mass energy absorption coefficient for scattered photon

```
      xmulabs=temtr*rsq*2.0*PI*elecm3
```

evaluation of integral

```
      y=xmuo*COSD(a)-xmul
      if(ATAND(field/(2.0*x2)).GE.a) then
```

maximum angle for first slab is smaller than 180 degrees

determine whether this angle has been reached

```
            if(ATAND(field/(2.0*x1)).GE.a)then
            lm=(x1-x2)/COSD(a)
      else
            lm=((field/2.0)-x2*TAND(a))/SIND(A)
      end if
      x=xmul*ro3*x2/COSD(a)
      if(y.eq.0.0)then
            r=0.0
      else
            r=(EXP(lm*y)-1)/y
      end if
```

```
   Evaluation of swl
      Su=hn*xmulabs*SIND(a)*dsig*EXP(-x)*r*0.01*(PI/180)
      suml=suml+Su
      end if
            if(ATAND(field/(2.0*x2)).GE.a)then
```

```
                    rm=x2/COSD(a)

         else

                    rm=field/2.0/SIND(a)

      end if

      if(y.eq.0.0)then

            st=0.0

      else

            st=(EXP(rm*y)-1)/y

      end if


Evaluation of Sw2

      ad=hn*xmulabs*SIND(a)*dsig*st*0.01*(PI/180)

      if (abs(a-10.0) .lt. 0.01) then

         type*,'hn=',hn

         type*,'dsig=',dsig

         type*,'xmul=',xmul

         type*,'xmulabs=',xmulabs

         type*,'lm=',lm

         type*,'rm=',rm

         type*,'Su=',Su

         type*,'ad=',ad

      endif

      sum2=sum2+ad

   end do


   swlflu=sum1*2*PI*elecm3*EXP(-xmuo*(x1-x2))

   type*,'This is first scatter dose per

1     unit flux from first layer'

   type*,'swlflu=',swlflu
```

```
sw2flu=sum2*2.0*PI*elecm3*EXP(-xmuo*x1)

type*,'This is the first scatter dose
1    per unit flux from 2nd layer'

type*,'sw2flu=',sw2flu

type*,'Please enter primary energy absorption coefficient;'

accept*, xmuoabs

sp=sw2flu/(xmuoabs*hno*EXP(-xmuo*x2))

type*,'This is the first scatter to primary ratio of the
1    second layer'

type*,'sp=', sp

stop

end
```